Numerical Simulation of Tropical Cyclones using Goal-Oriented Adaptivity

Zur Erlangung des akademischen Grades eines

DOKTORS DER NATURWISSENSCHAFTEN

von der Fakultät für Mathematik des

Karlsruher Instituts für Technologie (KIT)

genehmigte

DISSERTATION

von

Dipl.-Math. techn. Martin Baumann

aus

Oberhausen-Rheinhausen

Tag der mündlichen Prüfung: 21. Dezember 2011

Referent: Prof. Dr. Vincent Heuveline
Korreferent 1: Prof. Dr. Dominik Schötzau
Korreferent 2: Prof. Dr. Sarah Jones

Abstract

In this work, an extension of existing goal-oriented a posteriori error estimators for Petrov-Galerkin methods is developed. For conforming space-time finite element discretizations of parabolic problems, this extension allows the construction of economical meshes on which user-defined physical quantities of interest can be determined efficiently. These techniques are applied to scenarios of tropical cyclone dynamics to improve the precision of storm forecasts. By means of optimized space-time meshes, the position error of predicted storm tracks can be reduced significantly. Furthermore, aspects of the approximation of unknown quantities needed for the error estimation are discussed. In this context, a block strategy based on the solution of local Dirichlet problems and global defect correction is proposed. Several variants of the error estimator and resulting adaptive methods are systematically compared based on scenarios with exact analytical solutions.

Zusammenfassung

In dieser Arbeit wird eine Erweiterung existierender Ziel-orientierter Fehlerschätzer für Petrov-Galerkin Methoden entwickelt. Diese ermöglicht es für parabolische Probleme Diskretisierungen mit Raum-Zeit Finite-Elementen so auszulegen, dass beliebige physikalische Größen, die von Interesse sind, effizient bestimmt werden können. Diese Techniken werden auf Szenarien der Dynamik tropischer Wirbelstürme zur Verbesserung der Genauigkeit von Sturmvorhersagen angewendet. Durch Gitteroptimierung in Raum und Zeit kann der Positionsfehler wesentlich verringert werden. Außerdem werden Aspekte zur Approximation gewisser unbekannter Größen, die für die Fehlerschätzung erforderlich sind, diskutiert. In diesem Zusammenhang wird eine Blockstrategie vorgestellt, die auf lokalen Dirichlet-Problemen und globaler Defekt-Korrektur basiert. Mehrere Varianten des Fehlerschätzers und zugehörige adaptive Verfahren werden anhand von Szenarien mit exakten analytischen Lösungen systematisch verglichen.

Acknowledgments

A special thank is devoted to Prof. Dr. Vincent Heuveline who offered me the opportunity to work in the field of goal-oriented adaptive methods. I thank him for many fruitful discussions and support during the last years. Furthermore, I want to thank Prof. Dr. Sarah Jones and Dr. Leonhard Scheck for numerous discussions and advice not only for questions concerning meteorological topics. I enjoyed working in this interdisciplinary project very much. This research was supported by the German Research Foundation (DFG) priority programme (SPP) 1276.

Contents

1 Introduction

For many numerical simulations, the first intention is the precise approximation of an application dependent physical quantity of the solution such as a point value or an integral over a certain region, for example. Methods for efficient determination of this quantity are needed instead of good approximations with respect to global error norms, in this case. The Dual Weighted Residual (DWR) method represents a generic framework for goal-oriented error control and mesh adaptation and goes back to [2, 20]. For a *goal functional* that represents the quantity of interest, the sensitivity with respect to perturbations is given by the solution of a *dual problem*. Based on this information, the error of an approximate solution measured in the goal functional can be determined by means of an a posteriori error estimator. Local mesh adaptation towards an equal distribution of each cell's error contribution leads to economical meshes for the determination of the quantity of interest. Meanwhile, such techniques are widely established in many fields of application, such as fluid flow with chemical reactions [8, 12], solid mechanics [44], hydrodynamic stability [26], and aerodynamic flow simulation [24]. In this work, such adaptive techniques are further developed and applied to atmospheric fluid flow scenarios.

Tropical cyclones (TCs) are intense atmospheric vortices that form over tropical oceans. Their power source is the latent heat contained in the warm, water vapor saturated air above the ocean surface. This energy is released as the air ascends and expands in the storm, and the water vapor condenses. Powered by this energy source, tropical cyclones can reach wind speeds of more than 250 km/h. In case the storm reaches the coast and begins to travel over land, heavy damages can be caused by severe winds, torrential rainfall and flooding. Predicting the motion and intensity evolution of tropical cyclones is a difficult task, since atmospheric processes on a wide range of scales must be considered. In order to improve the precision of forecasts and resulting early warnings, the understanding and modeling of the highly complex multi-scale problem must be further enhanced.

The motion of TCs is mainly determined by the flow on large scales (several thousand kilometers) while the storm's intensity is regulated primarily by processes on the scale of one kilometer and below. However, the influence a storm has on the large scale flow is also determined by its intensity. The latter affects the environment of the storm and thus also the small-scale processes which are important for the evolution of the intensity. Models that describe the dynamics of the atmosphere must account for interacting processes on all these scales. By means of numerical simulations based on finite dimensional approximations, forecasts of storm tracks and intensity can be made. Not all of the relevant scales can be resolved due to restrictions of available computer resources. Some effects are located on the sub-grid scales and require adequate parametrization. Despite the use of massively parallel computing capabilities of today's supercomputers, high-resolution numerical simulations of a storm including the near environment are restricted to a horizontal resolution of a few hundred meters and a vertical resolution of about 50 meters at best [15]. On such meshes, motion in a horizontal scale of about 1 km at minimum can be resolved, which is insufficient to resolve small cloud dynamics. In order to give precise early warnings, the necessary forecasts must be calculated on time and are therefore typically based on coarser mesh resolutions. Since not all existing scales can be well-resolved for such problems, the use of adaptive methods based on meshes with varying resolution is promising. Whenever the smallest scale that locally must be resolved varies strongly over the domain, adaptive meshes can lead to a substantial decrease of unknowns in discrete numerical models. For TC forecasting, mesh nesting techniques are often employed to enhance the resolution locally. Based on more flexible unstructured meshes, the regionally varying demand with respect to the mesh's resolution can be exploited even better. However, one of the most important questions is which parts of the mesh should be refined to improve the precision of the resulting forecasts.

The influence that perturbations of the atmospheric state can have on the dynamics of a TC depends strongly on their spatial distribution. This is suggested by sensitivity studies based on ensemble simulations with perturbed initial data, linearized models, and adjoint models, cf. [16]. Therefore, goal-oriented adaptive methods that make use of such sensitivity information are very promising. Although the application of the generic approach described by the DWR method is straightforward, the task is demanding due to the complexity of atmospheric models (time-dependent, three-dimensional, including chemical reactions, and moist effects). These models can include model-switches (e.g. different sub-grid models for different regimes) that can be problematic for the calculation of the adjoint sensitivity. Additionally, the adequate definition of goal functionals that lead to improvements of TC forecasting is not obvious. In this work, meteorological scenarios based on a simplified model for atmospheric large-scale dynamics are considered.

The a posteriori estimators for the error in user-defined functionals, described in [2], require Galerkin approximations of the considered problems. To apply goal-oriented methods to time-dependent problems, variational formulations in terms of integrals over space and time and corresponding space-time finite element discretizations are adequate. The corresponding dual problem is also time-dependent and posed backward in time. In [23], goal-oriented error estimators for instationary problems were proposed in the context of the heat equation. Error estimators for general parabolic problems were investigated in [40] in the context of discontinuous Galerkin methods (non-conforming) as well as Petrov-Galerkin methods. In the latter case, only the primal problem was discretized conformingly, i.e. using continuous trial functions, while the dual problem was discretized in terms of discontinuous trial functions. To the knowledge of the author, the case of conforming discretizations in terms of continuous trial functions for both the primal and dual problems has not been addressed so far. In this work, a generalization of the goal-oriented error characterization to this context is proposed and corresponding a posteriori error estimators are derived. An additional term that originates from the different structures of the discrete trial and test spaces must be considered. Furthermore, error indicators are derived which quantify the error contribution related to the space and time discretization separately. In terms of these indicators, the mesh adaptation procedure can be controlled.

This thesis is organized as follows. In Chapter 2, the Navier-Stokes equations (NSE) and corresponding variational formulations are shortly outlined. This set of equations describes the flow dynamics for a wide class of fluids and represents an essential part of many atmospheric models. The widely-used two-dimensional barotropic model can be derived from the NSE and has proven to provide a useful approximate description of the processes that determine the motion of a tropical cyclone. The model and the related assumptions are shortly depicted. Furthermore, a conforming discretization based on space-time finite elements is given which leads to a Petrov-Galerkin method. In Chapter 3, an extension of the goal-oriented error characterization for Petrov-Galerkin approximations is given, and resulting a posteriori error estimators are derived in the context of parabolic problems. The evaluation of the error estimators requires the approximation of unknown quantities. In that context several strategies are discussed. Furthermore, a block method based on local Dirichlet problems and global defect-correction is proposed. Finally, the error estimator for the Navier-Stokes equations is described in detail. This includes the precise definition of cellwise error indicators that allow to distinguish between contributions related to the temporal and the spatial discretization, respectively. In Chapter 4, adaptive numerical simulations based on different variants of the goal-oriented error estimators are applied to stationary scenarios with known analytical solution. This allows a systematic comparison of the different approximation strategies of the unknown quantities with respect to the reliability of the estimators and the efficiency of adaptive methods. A scenario of interacting tropical cyclones is investigated in Chapter 5. Mesh adaptation strategies for the construction of optimal space-time discretizations are presented. Based on adaptive numerical simulations, both the error in the output functionals as well as the error in the predicted storm position could be reduced significantly. In the final chapter, the presented results are shortly summarized and aspects of further developments are discussed.

2 Fluid Flow Model

Atmospheric fluid flow can be described by models that are based on the Navier-Stokes equations. These can be derived from physical conservation properties of mass, momentum, and energy and can be extended to include effects such as chemical reactions and humidity, for example. The resulting set of equations is quite complex, i.e. instationary, three-dimensional, highly nonlinear, and often strongly coupled. Assuming typical atmospheric conditions, the relative importance of the different terms in these equations can be assessed by means of a scale analysis. Neglecting the less important terms leads to more idealized, mathematically simpler models that are still able to describe important atmospheric processes. The barotropic model investigated in this work is strongly idealized, but provides still a useful approximate description of the large-scale flow in the atmosphere.

After a short overview of related mathematical definitions and notations, the Navier-Stokes equations for incompressible Newtonian fluids and corresponding weak formulations are given. Based on these problem formulations, statements on existence and uniqueness of solutions are summarized. The two-dimensional barotropic model equations and assumptions involved in their derivation are outlined. Finally, a discretization in terms of a space-time finite element method is presented that is used for goal-oriented adaptive numerical simulations in later sections.

2.1 Functional Analytical Background

In this section, some function spaces and notations are shortly introduced. Let $\Omega \subseteq \mathbb{R}^d$, with $d \in \{2,3\}$, denote an open bounded domain with boundary $\partial\Omega$. For $1 \leq p < \infty$, the space $L^p(\Omega)$ consists of real functions for which the pth power is measurable with respect to the Lebesque measure $dx = dx_1 \cdots dx_d$. Equipped with the norm

$$\|f\|_{L^p(\Omega)} := \left(\int_\Omega |f(x)|^p dx \right)^{1/p},$$

the space $L^p(\Omega)$ is a Banach space. In the case $p = 2$, the space $L^2(\Omega)$ is a Hilbert space with the inner product

$$(f,g) := (f,g)_\Omega := (f,g)_{L^2(\Omega)} := \int_\Omega f(x)g(x)\,dx.$$

The corresponding norm is denoted by $\|\cdot\|$ or $\|\cdot\|_\Omega$. The space $H^m(\Omega)$ denotes the space of $L^2(\Omega)$ functions with distributional derivatives that are $L^2(\Omega)$ up to order m. $H^m(\Omega)$ equipped with the scalar product and norm

$$(f,g)_{H^m(\Omega)} := \sum_{|\alpha| \leq m} (D^\alpha f, D^\alpha g)_{L^2(\Omega)}, \quad \|f\|_{H^m(\Omega)} := \left(\sum_{|\alpha| \leq m} \|D^\alpha f\|^2_{L^2(\Omega)} \right)^{1/2},$$

forms a Hilbert space. Here, the multi-index is defined as $\alpha := (\alpha_1, \ldots, \alpha_d) \in \mathbb{N}^d$ and

$$D^\alpha := D_1^{\alpha_1} \cdots D_d^{\alpha_1} := \frac{\partial^{\alpha_1 + \cdots + \alpha_d}}{\partial x_1^{\alpha_1} \cdots \partial x_d^{\alpha_d}}.$$

The Hilbert space $H_0^1(\Omega) \subseteq H^1(\Omega)$ is spanned of functions that vanish on the boundary $\partial\Omega$. Its dual space is denoted by $H^{-1}(\Omega)$, which is a Banach space equipped with the norm

$$\|f\|_{H^{-1}(\Omega)} := \sup_{\varphi \in H_0^1(\Omega)} \frac{\langle f, \varphi \rangle_{H^{-1}(\Omega), H_0^1(\Omega)}}{|\varphi|_{H^1(\Omega)}}, \quad |\varphi|_{H^1(\Omega)} := \left(\sum_{|\alpha|=m} \|D^\alpha \varphi\|_{L^2(\Omega)}^2 \right)^{1/2},$$

whereas $\langle f, \varphi \rangle_{H^{-1}(\Omega), H_0^1(\Omega)} := f(\varphi)$. Let V denote a real, separable and reflexive Banach space with dual space V^*. Let H denote a real and separable Hilbert space and let $V \hookrightarrow^d H$ (continuous embedding and dense). Then the spaces (V, H, V^*) form a Gelfand triple. In this context, the duality pairing on $V^* \times V$ is a continuous extension of the scalar product on H, i.e.

$$(u, v)_H = \langle u, v \rangle_{V^*, V} \quad \forall u \in H \, \forall v \in V.$$

It is well-known, that $(H_0^1(\Omega), L^2(\Omega), H^{-1})$ forms a Gelfand triple. For more details on Sobolev spaces and related concepts, the reader is referred to [1].

For the investigation of the incompressible Navier-Stokes equations with homogeneous Dirichlet boundary conditions, the following spaces are introduced. Let $\mathcal{D}(\Omega)$ denote the space of C^∞ functions with compact support contained in Ω and $\mathcal{V} := \{u \in \mathcal{D}(\Omega)^d \,|\, \nabla \cdot u = 0\}$. The closure of $\mathcal{V}$ in $L^2(\Omega)^d$ is denoted by H_{div} and the closure of $\mathcal{V}$ in $H_0^1(\Omega)^d$ is denoted by V_{div} . These spaces can be characterized by

$$\begin{aligned} H_{div} &= \{u \in L^2(\Omega)^d \,|\, \nabla \cdot u = 0 \text{ in } \Omega, \, n \cdot u = 0 \text{ on } \partial\Omega\}, \\ V_{div} &= \{u \in H_0^1(\Omega)^d \,|\, \nabla \cdot u = 0 \text{ in } \Omega\}, \end{aligned}$$

where n denotes the outward unit normal vector of the boundary $\partial\Omega$. The spaces $(V_{div}, H_{div}, V_{div}^*)$ form a Gelfand triple [47]. In case of periodic boundary conditions, the corresponding spaces can be characterized by

$$\begin{aligned} H_{div} &= \{u \in H_p^0(\Omega)^d \,|\, \nabla \cdot u = 0 \text{ in } \mathbb{R}^d\}, \\ V_{div} &= \{u \in H_p^1(\Omega)^d \,|\, \nabla \cdot u = 0 \text{ in } \mathbb{R}^d\}, \end{aligned}$$

where a domain of the form $\Omega := [0, L_1] \times \cdots \times [0, L_p]$ is assumed. The space $H_p^m(\Omega)$ denotes the space of functions which are in $H_{loc}^m(\mathbb{R}^d)$ and fulfill the periodicity condition

$$u(x + L_i e_i) = u(x), \quad i = 1, \ldots, d, \forall x \in \mathbb{R}^d.$$

Here, e_i denotes the ith directional unit vector. $H_p^m(\Omega)$ is a Hilbert space with scalar product $(\cdot, \cdot)_{H_p^m(\Omega)} := (\cdot, \cdot)_{H^m(\Omega)}$ and further $H_p^0(\Omega) \equiv L^2(\Omega)$. It is well-known that the periodic function spaces $(V_{div}, H_{div}, V_{div}^*)$ also form a Gelfand triple [46].

For time-dependent problems, the considered functions are functions in time. Let B denote a separable Banach space. For $m \in \mathbb{N}$, let $C^m([0, T]; B)$ denote the space of continuous functions defined on $[0,T]$ that have mth continuous derivative. Further, let $C([0,T];B) := C^0([0,T];B)$. The space $C^m([0,T];B)$ is a Banach space equipped with the norm

$$\|f\|_{C^m([0,T];B)} := \max_{t\in[0,T]} \sum_{j=0}^{m} \left\| f^{(j)}(t) \right\|_B .$$

$L^p(0,T;B)$ denotes the space of equivalence classes of Bochner integrable functions $f : [0,T] \to B$, i.e.

$$\begin{aligned} L^p(0,T;B) \quad &:= \quad \left\{ f \mid f : [0,T] \to B,\, \|f\|_{L^p(0,T;B)} < \infty \right\} \quad (1 \le p \le \infty), \\ \|f\|_{L^p(0,T;B)} \quad &:= \quad \begin{cases} \left(\int_0^T \|f(t)\|_B^p \, dt \right)^{1/p}, & \text{for } 1 \le p < \infty, \\ \operatorname{ess\,sup}_{t\in(0,T)} \|f(t)\|_B, & \text{for } p = \infty. \end{cases} \end{aligned}$$

$L^p(0,T;B)$ is also a Banach space. For $1/p + 1/q = 1$, the dual space $(L^p(0,T;B))^*$ can be identified with $L^q(0,T;B^*)$. A corresponding dual pairing is given by

$$\langle f, u \rangle_{L^q(0,T;B^*),L^p(0,T;B)} = \int_0^T \langle f(t), u(t) \rangle_{B^*,B} \, dt.$$

Furthermore, it holds that $L^p(0,T;B) \hookrightarrow L^q(0,T;B)$ for arbitrary $1 \le q \le p \le \infty$. The derivative $\partial_t u$ of an abstract function $u \in L^2(0,T;B)$ is defined in the sense of distributions: If $w : [0,T] \to B$ exists such that $-\int_0^T u(t)\varphi'(t)dt = \int_0^T w(t)\varphi(t)dt$ for all $\varphi \in C_0^\infty(0,T)$, then the (distributional) derivative is defined by $\partial_t u := w$. For a Gelfand triple (V,H,V^*), the space of V-valued functions with distributional derivative in the dual space V^* is denoted by

$$W := W(0,T) := \left\{ f \mid f \in L^2(0,T;V),\, \partial_t f \in L^2(0,T;V^*) \right\}.$$

It is well-known that equipped with the scalar product

$$(f,g)_W := \int_0^T (f(t),g(t))_V \, dt + \int_0^T (f'(t),g'(t))_{V^*} dt,$$

the space W is a Hilbert space [51]. Functions in W are almost everywhere equal to a continuous function and the embedding $W \hookrightarrow C([0,T],H)$ is continuous, hence initial conditions of parabolic problems posed as function in H make sense. By the Lions-Aubin lemma, the embedding $W \hookrightarrow^c L^2(0,T;H)$ is compact [19]. Furthermore, for arbitrary functions $f, g \in W$, the integration by parts rule holds, i.e.

$$\int_0^T \Big(\langle \partial_t f(t), g(t) \rangle_{V^*,V} + \langle f(t), \partial_t g(t) \rangle_{V,V^*} \Big) dt = (f_{|t=T}, g_{|t=T})_H - (f_{|t=0}, g_{|t=0})_H. \tag{2.1}$$

Lemma 1. *The space* $W(0,T) \cap L^p(0,T;V)$ *is dense in* $L^2(0,T;V)$ *for* $1 \le p \le \infty$.

Proof. The space $C^\infty([0,T];V)$ is dense in $W(0,T)$ (for a proof see [19], p. 206, for example). Furthermore, the space $C^\infty([0,T];V)$ is also dense in $L^2(0,T;V)$ (this can be proved by mollification, analogously to the previous dense inclusion). For any $f \in C^\infty([0,T];V) \subseteq C([0,T];V)$ it holds that

$$\|f\|_{L^\infty(0,T;V)} = \operatorname{ess}\sup_{t\in(0,T)} \|f(t)\|_V \leq \max_{t\in[0,T]} \|f(t)\|_V = \|f\|_{C([0,T];V)},$$

hence $f \in L^\infty(0,T;V)$. Therefore, it holds that

$$C^\infty([0,T];V) \subseteq L^p(0,T;V), \quad 1 \leq p \leq \infty. \tag{2.2}$$

For arbitrary $x \in L^2(0,T;V)$ there exists a sequence $(x_i)_{i\in\mathbb{N}} \subseteq C^\infty([0,T];V)$ with $\|x_i - x\|_{L^2(0,T;V)} \to 0$ for $i \to \infty$. The inclusions $C^\infty([0,T],V) \subseteq W(0,T)$ and (2.2) imply $C^\infty([0,T],V) \subseteq W(0,T) \cap L^p(0,T;V)$. Hence for the sequence it holds that $(x_i)_{i\in\mathbb{N}} \subseteq W(0,T) \cap L^p(0,T;V)$. □

For more details on abstract functions and distributional derivatives, the reader is referred to e.g. [19, 29, 51].

2.2 The Incompressible Navier-Stokes Equations

The motion of Newtonian fluids is governed by the Navier-Stokes equations. A detailed derivation of the set of equations can be found e.g. in [43]. Central arguments that are taken into account are several physical properties of such fluids. For example, the conservation of mass and momentum (Newton's second law) yields the continuity equation and the momentum equation. Assuming a linear relationship between stress and strain rate (which defines Newtonian fluids), the stress tensor – which is included in the momentum equation – can be modeled by a constitutive relation in terms of only one parameter, i.e. the kinematic viscosity parameter. This leads to the following form of the Navier-Stokes equations for incompressible fluids (i.e. constant density). The initial boundary value problem for a time interval $I := [0,T]$ and the bounded domain $\Omega \subseteq \mathbb{R}^d$ $(d = 2,3)$ with Lipschitz boundary $\partial\Omega$ is given by: Find a velocity field $\upsilon : [0,T] \times \Omega \to \mathbb{R}^d$ and pressure $p : [0,T] \times \Omega \to \mathbb{R}$ such that

$$\begin{aligned}
\partial_t \upsilon - \nu\Delta\upsilon + (\upsilon\cdot\nabla)\upsilon + \nabla p &= f \quad \text{in } I\times\Omega, && (2.3)\\
\nabla\cdot\upsilon &= 0 \quad \text{in } I\times\Omega, && (2.4)\\
\upsilon_{|t=0} &= \upsilon_0 \quad \text{in } \Omega, && (2.5)\\
\upsilon &= 0 \quad \text{in } I\times\partial\Omega, && (2.6)
\end{aligned}$$

holds. The volume force f and the velocity's initial state υ_0 are given. The kinematic viscosity $\nu > 0$ is a material parameter. A pressure that is solution of Equation (2.3) is only unique up to an additive constant. Therefore, a further condition needs to be added, e.g. $\int_\Omega p\,dx = 0$. For many applications, other types of boundary conditions than the no-slip condition (2.6) are needed. Some features that naturally are contained within very large domains and don't have boundary layers (e.g. homogeneous turbulence), can be investigated in space-periodic domains. The periodicity condition has the following form

$$\upsilon(t, x + L_i e_i) = \upsilon(t,x) \quad \text{and} \quad p(t, x + L_i e_i) = p(t,x), \tag{2.7}$$

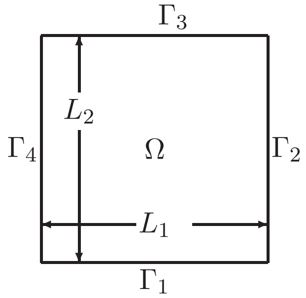

Figure 2.1: Periodic boundary conditions for the domain $\Omega = [0, L_1] \times [0, L_2] \subseteq \mathbb{R}^2$ with boundary $\partial\Omega = \Gamma_1 \cup \cdots \cup \Gamma_4$ lead to corresponding boundary tuples (Γ_1, Γ_3) and (Γ_2, Γ_4) on which condition (2.7) must hold.

for any $x \in \mathbb{R}^d$, any $t \in [0, T]$ and $i \in \{1, \dots, d\}$. Here, $L_i > 0$ denotes the period in the ith direction in space and e_i the ith directional unit vector, cf. Figure 2.1. Although often not physically feasible, models based on boundary condition (2.7) permit the analysis of important questions of practical relevance. Furthermore, the class of natural boundary conditions exists which often is used to model outflow boundaries, e.g.

$$\nu \partial_n v = pn, \tag{2.8}$$

where n denotes the outward unit normal vector of the boundary $\partial\Omega$.

Questions concerning existence and uniqueness of solutions of the initial boundary value problem (2.3)-(2.5) equipped with suitable boundary condition are not fully answered yet. The following weak formulation posed in divergence-free function spaces (see Section 2.1) is investigated in [46, 47], for example. Let the volume force $f \in L^2(0, T; V_{div}^*)$ and the initial velocity field $v_0 \in H_{div}$ be given. $v \in L^2(0, T; V_{div}) \cap L^\infty(0, T; H_{div})$ is a *weak solution* of the NSE, if

$$\begin{aligned} \frac{d}{dt}(v, \varphi) + \nu(\nabla v, \nabla \varphi) + ((v \cdot \nabla)v, \varphi) &= \langle f, \varphi \rangle_{V^*, V}\,, \\ v_{|t=0} &= v_0. \end{aligned} \tag{2.9}$$

for all $\varphi \in V_{div}$. It is well-known, that weak solutions of problem (2.9) exist. In 2D, the solution v can be proved to be unique and it holds that $v \in C([0, T]; H_{div})$ and $\partial_t v \in L^2(0, T; V_{div}^*)$. In 3D, solutions are weakly continuous from $[0, T]$ into H_{div} and $\partial_t v \in L^{4/3}(0, T; V_{div}^*)$.

While uniqueness of weak solutions in 3D has not been proven yet, the following results concerning uniqueness of strong solutions are known. Let $f \in L^\infty(0, T; H_{div})$ and $v_0 \in V_{div}$. A function $v \in L^2(0, T; S)$ with $\partial_t v \in L^2(0, T; H_{div})$ and $v \in \mathcal{C}([0, T]; V_{div})$, is a *strong solution* of the NSE, if (2.9) holds. The space S is defined by $S := \{u \,|\, u \in H_{div}, \, \Delta u \in H_{div}\}$ for the space-periodic case, and by $S := V_{div} \cap H_{div}^2(\Omega)^d$ for the no-slip case. In 2D, such strong solutions exist and are unique. In 3D, there exists a unique solution on the interval $[0, \min\{T, T^*\}]$, where T^* depends on the data and might be smaller than T.

A connection between weak and strong solutions for given $f \in L^\infty(0, T; H_{div})$ and $v_0 \in V_{div}$ can be stated as follows: In 2D, a weak solution is also a strong solution. In 3D, a weak solution is also a strong solution on $[0, \min\{T, T^*\}]$. If the solution v has further regularity, e.g. $v \in L^4(0, T; V)$, then v is a strong solution on $[0, T]$.

Details on these statements as well as related proofs can be found in [46, 47], for example. In the following, the two-dimensional case with no-slip or periodic boundary conditions is considered.

The calculation of approximate solutions for the NSE based on conforming discretization methods requires the definition of finite dimensional subspaces of the function spaces related to the corresponding continuous variational problem. To avoid the implementation of solenoidal function spaces (divergence-free functions), a variational formulation in so-called mixed form is considered (see [22, 36], for example). Let $\Omega \subseteq \mathbb{R}^d$ be a bounded domain with Lipschitz continuous boundary. For the case of no-slip boundaries the space of the velocity component is defined as $V := H_0^1(\Omega)^2$ and the pressure space is defined as $Q := L_0^2(\Omega) := \left\{p \in L^2(\Omega) \mid \int_\Omega p\, dx = 0\right\}$. For given initial velocity $\upsilon_0 \in H_{div}$ and force $f \in L^2(0,T;V_{div})$, where the spaces H_{div} and V_{div} are defined in Section 2.1, the following variational problem can be stated: Find $\upsilon(t) \in V$ and $p(t) \in Q$ such that for almost every $t \in (0,T)$

$$\begin{aligned} d_t(\upsilon(t),\varphi) + (\upsilon(t)\cdot\nabla)\upsilon(t) - (f(t),\varphi) + \nu(\nabla\upsilon(t),\nabla\varphi) - (p(t),\nabla\cdot\varphi) &= 0, \\ (\nabla\cdot\upsilon(t),\psi) &= 0, \\ \upsilon_{|t=0} &= \upsilon_0, \end{aligned} \tag{2.10}$$

holds for any $\varphi \in V$ and any $\psi \in Q$. For the space-periodic case, a square domain $\Omega = [0,L_1]\times[0,L_2]$ is assumed. In this case, the space of the velocity field is defined as $V := H_p^1(\Omega)^2$ (see Section 2.1 for details). For a solution (υ,p) of problem (2.10) the regularity property $\partial_t\upsilon \in L^2(0,T;V^*)$ holds, cf. [47]. Solutions of problem (2.10) are also solutions of problem (2.9). Conversely, solutions of (2.9) must possess further regularity properties to guarantee the existence of a pressure function [36].

Since later approximate solutions of the NSE should be calculated in terms of space-time finite element methods, variational formulations based on integrals over space and time are natural. In [31], Layton states a variational formulation for strong solutions based on the following function spaces:

$$\begin{aligned} X &:= W(0,T)\cap L^4(0,T;V)\cap L^\infty(0,T;H), \\ Y &:= L^2(0,T;V)\cap L^\infty(0,T;H), \\ M &:= L^2(0,T;Q). \end{aligned}$$

$(\upsilon,p) \in X\times M$ is a *strong solution* of the NSE, if

$$\int_0^T \Big((\partial_t\upsilon + (\upsilon\cdot\nabla)\upsilon - f,\varphi) + \nu(\nabla\upsilon,\nabla\varphi) - (p,\nabla\cdot\varphi) + (\nabla\cdot\upsilon,\psi)\Big)\, dt + (\upsilon_{|t=0} - \upsilon_0, \varphi_{|t=0}) = 0, \tag{2.11}$$

for all $(\varphi,\psi) \in Y\times M$. A solution of (2.11) is also solution of problem (2.10). This formulation will later be used to define conforming discretizations in terms of adequate finite dimensional subspaces of X, Y and M.

2.3 The Barotropic Model

The Earth's rotation has strong influence on the dynamics of the atmosphere. This can be accounted for by an extension of the momentum equation of the NSE by a Coriolis term. Its influence depends on the latitude Φ (describing the position on Earth, whereas the origin is the equator) and is given in terms of the Earth's rotation vector $(0, 0, \omega^{(\text{Earth})})^T$, where $\omega^{(\text{Earth})} \approx 7.27 \cdot 10^{-5}\, 1/\text{s}$. The resulting Coriolis acceleration has the form

$$f_{cor} e_3 \times \upsilon, \quad e_3 := (0, 0, 1)^T.$$

The Coriolis parameter is defined as $f_{cor} := 2\omega^{(\text{Earth})} \sin \Phi$ and depends only on the y-coordinate, in case of a Cartesian coordinate system (x-coordinate in eastern direction, y-coordinate in northern direction). For investigations of large-scale phenomena at the mid-latitudes, the following linear approximation of the Coriolis parameter based on a Taylor series about a reference latitude Φ_0 is often used:

$$f_{cor} \approx f_{cor}(y_0) + \beta y, \quad \beta := d_y f_{cor}(\Phi_0).$$

This approximation is usually denoted by *mid-latitude beta-plane*. For the synaptic scale (horizontal length scale: about 1000 km), a scale analysis of the horizontal momentum equations indicates that the Coriolis force and the pressure gradient force are the dominating terms. The wind is approximately a result from the balance between these two effects (geostrophic balance). For the vertical component of the momentum equation, a scale analysis justifies the hydrostatic assumption, i.e. $\partial_z p \equiv -\rho g$, where g denotes the gravity force and ρ the density of air. For a barotropic atmosphere, surfaces of constant pressure, constant density and constant temperature (ideal gas assumed) are parallel. In this case, the horizontal wind is independent of height [30]. Furthermore, the assumption that the velocity is purely horizontal, i.e. $\upsilon_3 \equiv 0$, leads to the two-dimensional *barotropic model*:

$$\begin{aligned} \partial_t \upsilon + (\upsilon \cdot \nabla)\upsilon + \frac{1}{\rho}\nabla p + f_{cor} e_3 \times \upsilon &= 0 \quad \text{in } [0, T] \times \Omega, & (2.12) \\ \nabla \cdot \upsilon &= 0 \quad \text{in } [0, T] \times \Omega. & (2.13) \end{aligned}$$

Although the molecular viscosity of air is neglected due to the scale analysis, it is common to add effects of diffusion to (2.12). These can represent effects of turbulent mixing and diffusion due to convection of the three-dimensional atmosphere. The resulting equations have the form

$$\begin{aligned} \partial_t \upsilon + (\upsilon \cdot \nabla)\upsilon - \nu \Delta \upsilon + \frac{1}{\rho}\nabla p + f_{cor} e_3 \times \upsilon &= 0 \quad \text{in } [0, T] \times \Omega, & (2.14) \\ \nabla \cdot \upsilon &= 0 \quad \text{in } [0, T] \times \Omega, & (2.15) \end{aligned}$$

where $\nu \geq 0$ denotes the viscosity parameter. The system (2.14)-(2.15) can be reformulated in terms of the vorticity $\xi := \nabla \times \upsilon$. To this end, the rotation operator is applied to the momentum equation (2.14) and exploiting (2.15) yields the vorticity equation

$$\partial_t \xi + (\upsilon \cdot \nabla)\xi - \nu \Delta \xi + (\partial_y f_{cor})\upsilon_2 = 0. \tag{2.16}$$

Since $\partial_t f_{cor} \equiv \partial_x f_{cor} \equiv 0$ holds, problem (2.16) can be written in terms of the absolute vorticity $\eta := \xi + f_{cor}$:

$$d_t\eta = \partial_t\eta + (\upsilon \cdot \nabla)\eta = \nu\Delta\xi. \tag{2.17}$$

Therefore, the absolute vorticity is conserved in case of vanishing viscosity. This model is often used to predict flow patterns in the tropics and equatorial regions. It represents the synaptic-scale flow field at a constant pressure surface of 500 mb. The equivalence of the problem (2.14)-(2.15) and problem (2.16) in case of neglected Coriolis force is proved in [32].

2.4 The Discretization

Many finite element methods for the NSE are based on finite dimensional subspaces of the spatial function space, e.g. $Q_h \subset Q$ and $V_h \subset V$, and a finite difference approximation of the temporal differential operators. In contrast, space-time finite element methods can be defined in terms of discrete function spaces both in space and time. The calculation of approximate solutions for problem (2.11), necessitates the replacement of the spaces X, Y and M by finite dimensional spaces $X_{h\tau} \subseteq X$, $Y_{h\tau} \subseteq Y$ and $M_{h\tau} \subseteq M$. The subscript 'τ' indicates a temporal discrete and the subscript 'h' indicates a spatial discrete nature of the underlying objects. This approach results in conforming discretization methods as the discrete spaces are subspaces of the corresponding continuous spaces. Since the trial and test spaces are not identical, the discretization leads to a Petrov-Galerkin approximation. In the following, details on the discretization in time and space are described.

2.4.1 Time Discretization: Continuous Galerkin-Petrov Method

In this section a conforming semi-discretization in time for an abstract parabolic problem is described. Let the spaces (V, H, V^*) form a Gelfand triple. For given force-term $f \in L^2(0, T; V^*)$ and initial condition $u_0 \in H$, find $u \in W := W(0, T)$ such that

$$\int_0^T \Big(\langle \partial_t u - f, \varphi \rangle_{V^*,V} + a(u, \varphi) \Big)\, dt + (u_{|t=0} - u_0, \varphi_{|t=0})_H = 0, \tag{2.18}$$

holds for all $\varphi \in L := L^2(0, T; V)$. Here, $a : V \times V \to \mathbb{R}$ denotes a continuous and elliptic bilinear form, i.e. there exist constants $\alpha > 0$ and $C > 0$ such that

$$\begin{aligned} a(u, u) &\geq \alpha \|u\|_V^2 , \\ |a(u, v)| &\leq C \|u\|_V \|v\|_V , \end{aligned}$$

holds for all $u, v \in V$. As the test functions are elements of space L, discontinuities in time are allowed. Thereby the global problem can be decoupled into a sequence of smaller problems. Let the following $N + 1$ points define the temporal mesh:

$$0 = t_0 < t_1 < \cdots < t_N = T. \tag{2.19}$$

On each sub-interval $I_i := (t_{i-1}, t_i)$ the trial and test functions are defined as V-valued polynomials. The trial space $W_\tau \subseteq W$ is defined such that functions are

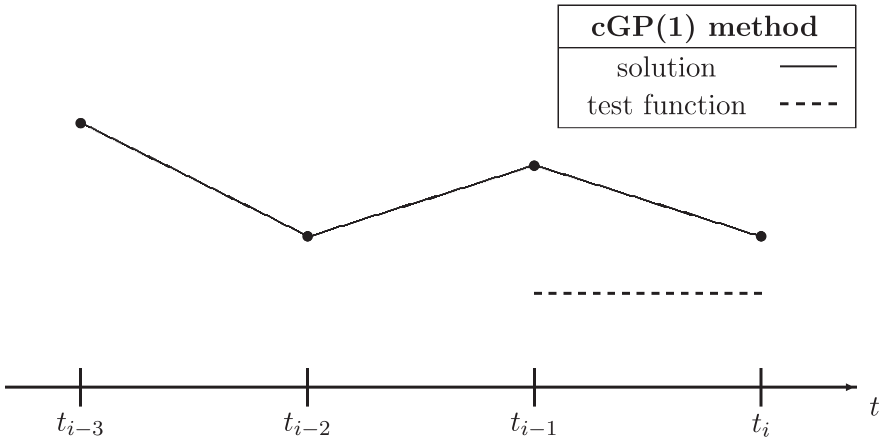

Figure 2.2: The cGP(1) method: Piecewise linear trial functions, globally continuous, and piecewise constant test functions.

continuous on $[0,T]$. The test functions in the space $L_\tau \subseteq L$ may be discontinuous at all points t_i $(i = 0,\dots,N-1)$. The value of any test function at t_i may be chosen arbitrary (e.g. right-sided or left-sided limit), since points are sets of measure zero. For both trial and test space the polynomial degree is chosen constant over all time intervals I_i, respectively. The spaces are defined such that the polynomial degree of the test functions is by one lower compared to the one of the trial functions. Since the trial functions must fulfill a continuity condition, the number of degrees of freedom is decreased by one on each interval, cf. Figure 2.2. The time-discrete spaces are defined as

$$W_\tau := \Big\{ u \in C(I,V) \,|\, u_{|_{I_i}} \in \mathbb{P}_k(I_i,V),\ 1 \le i \le N \Big\}, \tag{2.20}$$

$$L_\tau := \Big\{ \varphi \in L^2(I,V) \,|\, \varphi_{|_{I_i}} \in \mathbb{P}_{k-1}(I_i,V),\ 1 \le i \le N \Big\}. \tag{2.21}$$

The space of piecewise V-valued polynomials is

$$\mathbb{P}_k(I_i,V) := \left\{ u : I_i \to V \,|\, u(t) = \sum_{n=0}^{k} u_n t^n \,\forall t \in I_i,\ u_n \in V,\ 0 \le n \le k \right\},$$

for $1 \le i \le N$. This choice of the discrete spaces leads to a stable method [39] referred to as the *cGP(k) method* (or sometimes *dGP(k) method*) in the literature. Here, k denotes the polynomial degree in definitions (2.20) and (2.21). The resulting semi-discrete variational problem can be stated as follows: Find $u_\tau \in W_\tau$ such that

$$\int_0^T \Big(\langle \partial_t u_\tau - f, \varphi_\tau \rangle_{V^*,V} + a(u_\tau,\varphi_\tau) \Big)\, dt + (u_{\tau|t=0} - u_0, \varphi_{\tau|t=0})_H = 0, \tag{2.22}$$

for all $\varphi_\tau \in L_\tau$. As the test functions are discontinuous at points in time t_i, the discrete problem (2.22) can be solved as time-stepping scheme where the time intervals I_i are treated consecutively. Hence, problem (2.22) can be stated as: Find

$u_\tau \in W_\tau$ such that

$$\int_{t_{i-1}}^{t_i} \Big(\langle \partial_t u_\tau - f, \varphi_\tau \rangle_{V^*,V} + a(u_\tau, \varphi_\tau) \Big)\, dt = 0, \tag{2.23}$$

for all $i \in \{1, \dots, N\}$ and all $\varphi_\tau \in L_\tau$ and the initial condition $u_{\tau|t=0} = u_0$ holds. It is well-known that for linear problems the cGP(k) method is A-stable and unique solutions exists. For sufficiently smooth solutions of the continuous problem a priori error estimates are known. To formulate these, the solution is split into the parts

$$u(t) = u_0 + u^0(t), \quad u^0 \in W_0 := \{u \in W \mid u_{|t=0} = 0\}.$$

Assuming the existence of an interpolation operator $I_\tau : W_0 \to W_{0,\tau}$, where $W_{0,\tau} := \{u \in W_\tau \mid u_{|t=0} = 0\}$, with the following properties:

$$\begin{aligned} \left\| u^0 - I_\tau u^0 \right\|_{L^2(t_{i-1},t_i;V)} &\leq C(t_i - t_{i-1})^{k+1} \left\| \partial_t^{k+1} u^0 \right\|_{L^2(t_{i-1},t_i;V)}, \\ \left\| \partial_t (u^0 - I_\tau u^0) \right\|_{L^2(t_{i-1},t_i;V)} &\leq C'(t_i - t_{i-1})^{k} \left\| \partial_t^{k+1} u^0 \right\|_{L^2(t_{i-1},t_i;V)}, \end{aligned}$$

for each interval (t_{i-1}, t_i). Then the solution $u_\tau^0 \in W_{0,\tau}$ satisfies the following error estimate:

$$\left\| u^0 - u_\tau^0 \right\|_W \leq C'' \left(\sum_{i=1}^N (t_i - t_{i-1})^{2k} \left\| \partial_t^{k+1} u^0 \right\|_{L^2(t_{i-1},t_i;V)} \right)^{1/2}. \tag{2.24}$$

In terms of the maximum time step size $\delta := \max_{i=1,\dots,N}(t_i - t_{i-1})$ the following error estimate holds:

$$\left\| u^0 - u_\tau^0 \right\|_W \leq C''' \delta^k \left\| \partial_t^{k+1} u^0 \right\|_{L^2(0,T;V)}, \tag{2.25}$$

where C, C', C'' and C''' denote constants which are independent of the time steps and T. For a better estimate for the L^2-error, additional assumptions are needed. Assume $u \in H^1(t_{i-1}, t_i; V)$ for each interval (t_{i-1}, t_i). Let $w \in W_0$ denote the solution of the dual problem

$$\int_0^T \Big(\langle \partial_t w, \varphi \rangle_{V^*,V} + \langle A' w, \varphi \rangle_{V^*,V} \Big)\, dt = \int_0^T (r, \varphi)_H dt \quad \forall \varphi \in L^2(0,T;V).$$

Assume that for each right-hand side $r \in L^2(0,T;H)$ the solution fulfills $w \in H^1(0,T;V)$ and the a priori estimate

$$\| \partial_t w \|_{L^2(0,T;V)} \leq D \, \| r \|_{L^2(0,T;H)},$$

where D is a constant independent of r and T. Then for the discrete solution u_τ^0 the following error estimate holds

$$\left\| u^0 - u_\tau^0 \right\|_{L^2(0,T;H)} \leq D' \delta \left(\sum_{i=1}^N (t_i - t_{i-1})^{2k} \left\| \partial_t^{k+1} u^0 \right\|_{L^2(t_{i-1},t_i;V)} \right)^{1/2},$$

and

$$\left\| u^0 - u^0_\tau \right\|_{L^2(0,T;H)} \le D''\delta^{k+1} \left\| \partial_t^{k+1} u^0 \right\|_{L^2(0,T;V)},$$

where the constants D, D' and D'' are independent of the time-steps and T. Related proofs of these optimal error estimates and further details can be found in [39].

In the following let $k = 1$. In this case, the trial functions are linear in each interval $[t_{i-1}, t_i]$ and globally continuous. The test functions are constant in each (t_{i-1}, t_i) and may have discontinuities at all points of time t_i. Hence, there exist $u_{i-1}, u_i, \varphi_i \in V$ such that

$$\begin{aligned} u_\tau(t)_{|[t_{i-1},t_i]} &:= u_{i-1} + \frac{u_i - u_{i-1}}{t_i - t_{i-1}}(t - t_{i-1}), \\ \varphi_\tau(t)_{|(t_{i-1},t_i)} &:= \varphi_i. \end{aligned} \tag{2.26}$$

The time derivative of u_τ exists in the inner of each time interval as classical derivative of the linear function $u_\tau(t)_{|[t_{i-1},t_i]}$ and is constant within each interval:

$$\partial_t u_\tau(t)_{|(t_{i-1},t_i)} := \frac{u_i - u_{i-1}}{t_i - t_{i-1}}.$$

The corresponding time integral is given by

$$\int_{t_{i-1}}^{t_i} \langle \partial_t u_\tau, \varphi_\tau \rangle_{V^*,V} \, dt = (t_i - t_{i-1}) \left(\frac{u_i - u_{i-1}}{t_i - t_{i-1}}, \varphi_\tau \right)_H = (u_i - u_{i-1}, \varphi_\tau)_H.$$

The variational formulation of problem (2.23) can be stated in the form: Find $u_\tau \in W_\tau$ such that

$$(u_i - u_{i-1}, \varphi_\tau)_H + \int_{t_{i-1}}^{t_i} -(f, \varphi_\tau)_H + a(u_\tau, \varphi_\tau) \, dt = 0, \tag{2.27}$$

for all $i \in \{1, \dots, N\}$ and all $\varphi_\tau \in W_\tau$ and the initial condition $u_{\tau|t=0} = u_0$ holds. To calculate solutions of (2.27), the time integral can be evaluated using numerical quadrature rules. The *trapezoidal rule*

$$\int_a^b \Psi(t) \, dt \approx Q_t(\Psi) := \frac{b-a}{2} \left(\Psi(a) + \Psi(b) \right), \tag{2.28}$$

is of first order, which is exact if $a(\cdot,\cdot)$ is bilinear and f piecewise linear in time. In this case, the cGP(1) method corresponds to the Crank-Nicolson scheme. Applying this method to the nonlinear NSE, this quadrature rule is not exact. Using *Simpson's rule*

$$\int_a^b \Psi(t) \, dt \approx Q_s(\Psi) := \frac{b-a}{6} \left(\Psi(a) + 4\Psi\left(\frac{a+b}{2} \right) + \Psi(b) \right), \tag{2.29}$$

polynomials up to cubic degree lead to exact quadrature which is sufficient for the nonlinearity of the NSE (smooth volume force assumed). For clarity, the following abbreviating notations are introduced:

$$\Phi_i := \Phi(t_i), \quad \Phi_{i-1/2} := \frac{\Phi_{i-1} + \Phi_i}{2}. \tag{2.30}$$

Based on Simpson's rule, the time-discrete variational formulation has the form: Find $u_\tau \in W_\tau$ such that

$$\begin{aligned}(u_i - u_{i-1}, \varphi_\tau)_H + \frac{t_i - t_{i-1}}{6}\,(a(u_{i-1}, \varphi_\tau) + 4\,a(u_{i-1/2}, \varphi_\tau) + a(u_i, \varphi_\tau)&\\ -(f_{i-1}, \varphi_\tau)_H - 4\,(f_{i-1/2}, \varphi_\tau)_H - (f_i, \varphi_\tau)_H) &= 0,\end{aligned}$$

for all $i \in \{1, \ldots, N\}$ and all $\varphi_\tau \in W_\tau$.

For the NSE discrete subspaces of both trial spaces (velocity and pressure) and both test spaces need to be defined. The trial space of the velocity functions is the only space, that has continuity regularity. The discrete test functions and also the trial functions for the pressure are piecewise polynomials in time. The time-discrete spaces $X_\tau \subseteq X$, $Y_\tau \subseteq Y$ and $M_\tau \subseteq M$ are defined as

$$\begin{aligned}X_\tau &:= \left\{u \in C(I, V)\,|\,u_{|I_i} \in \mathbb{P}_1(I_i, V),\ 1 \le i \le N\right\},\\ Y_\tau &:= \left\{\varphi \in L^2(I, V)\,|\,u_{|I_i} \in \mathbb{P}_0(I_i, V),\ 1 \le i \le N\right\},\\ M_\tau &:= \left\{\varphi \in L^2(I, Q)\,|\,u_{|I_i} \in \mathbb{P}_0(I_i, Q),\ 1 \le i \le N\right\}.\end{aligned}$$

The constant, linear and quadratic parts (with respect to time) of the integrand in equation (2.11) are denoted by C, L and Q, respectively:

$$\begin{aligned}C(t) &:= (\partial_t v_\tau, \varphi_\tau) - (p_\tau, \nabla \cdot \varphi_\tau),\\ L(t) &:= \nu(\nabla v_\tau, \nabla \varphi_\tau) + (\nabla \cdot v_\tau, \psi_\tau),\\ Q(t) &:= ((v_\tau \cdot \nabla) v_\tau, \varphi_\tau),\\ F(t) &:= -(f, \varphi).\end{aligned}$$

On each interval I_i, the integral

$$\int_{t_{i-1}}^{t_i} R(t)\,dt, \quad R(t) := C(t) + L(t) + Q(t) + F(t),$$

can be determined using numerical quadrature rules. Simpson's rule yields exact results, assumed that the force term f is a piecewise polynomial of third order at most. On interval $[t_{i-1}, t_i]$, the value of the velocity at t_{i-1} is known due to the continuity of the trial space X_τ, i.e. $v_\tau(t_{i-1}) = v^{(i-1)}$. The time-discrete problem can be formulated: Find $(v^{(i)}, p^{(i)}) \in V \times H$ such that

$$\frac{t_i - t_{i-1}}{6}\left[R_{i-1} + 4R_{i-1/2} + R_i\right] = 0, \tag{2.31}$$

for all $(\varphi, \psi) \in V \times H$ and each $i \in \{1, \ldots, N\}$, further the initial condition $v_{\tau|t=0} = v_0$ must hold.

Remark 2. (Comparison to Crank Nicolson scheme) Due to the nonlinear term, the discretization based on the cGP(1) method differs from the Crank Nicolson scheme. Since

$$\begin{aligned}&((v^{i-1/2} \cdot \nabla) v^{i-1/2}, \varphi)\\ =\ &\frac{1}{4}((v^{i-1} + v^i) \cdot \nabla)(v^{i-1} + v^i), \varphi)\\ =\ &\frac{1}{4}((v^{i-1} \cdot \nabla) v^{i-1} + (v^{i-1} \cdot \nabla) v^i + (v^i \cdot \nabla) v^{i-1} + (v^i \cdot \nabla) v^i, \varphi),\end{aligned}$$

holds, the contribution of the nonlinear term $Q(t)$ on interval (t_{i-1}, t_i) to the discrete problem (2.31) is given by

$$\begin{aligned}
& \frac{t_i - t_{i-1}}{6} \left(Q_{i-1} + 4Q_{i-1/2} + Q_i\right) \\
= \; & \frac{t_i - t_{i-1}}{6} \Big(((v^{i-1} \cdot \nabla)v^{i-1}, \varphi) + 4((v^{i-1/2} \cdot \nabla)v^{i-1/2}, \varphi) + ((v^i \cdot \nabla)v^i, \varphi)\Big) \\
= \; & \frac{t_i - t_{i-1}}{6} \left(2Q_{i-1} + ((v^{i-1} \cdot \nabla)v^i + (v^i \cdot \nabla)v^{i-1}, \varphi) + 2Q_i\right).
\end{aligned}$$

In contrast, the contribution in case of a Crank Nicolson discretization would equal $\frac{t_i - t_{i-1}}{6} (3Q_{i-1} + 3Q_i)$. With respect to the constant and linear parts $C(t)$ and $L(t)$, and in case of a piecewise linear force-term f, the Crank Nicolson scheme and the cGP(1) method correspond.

For completeness, a discontinuous Galerkin method is shortly described in the following remark, where not only the discrete test functions may have discontinuities in time, but also the discrete trial functions. Because of the non-conformity $W_\tau \not\subseteq W$ with respect to the time-discretization, a modified variational formulation containing additional jumpterms defines the discrete problem.

Remark 3. (dG(k) method) To discretize the abstract variational problem (2.18) by a discontinuous Galerkin time stepping method, the time interval $[0, T]$ is partitioned based on (2.19) into half-open intervals

$$[0, T] = \{t_0\} \cup I_1 \cup I_2 \cup \cdots \cup I_N, \quad I_i := (t_{i-i}, t_i].$$

On each interval let the discrete test and trial space be defined as piecewise V-valued polynomials of degree $k-1$ where discontinuities are allowed at all times t_i, i.e.

$$W_\tau := L_\tau := \Big\{u \in L^2(I, V) \,|\, u_{|_{I_i}} \in \mathbb{P}_{k-1}(I_i, V),\ 1 \le i \le N\Big\}.$$

At the discontinuities, the jump of functions and one-sided limits are denoted by:

$$[\Phi]^{(i)} := \Phi^{(i,+)} - \Phi^{(i,-)},\ \Phi^{(i,+)} := \lim_{t \searrow t_i} \Phi(t),\ \Phi^{(i,-)} := \lim_{t \nearrow t_i} \Phi(t) = \Phi(t_i).$$

As before, the global problem can be decoupled and formulated as time-stepping scheme. On each interval I_i the corresponding problem has the following form: Find $u_\tau \in W_\tau$ such that

$$\int_{t_{i-1}}^{t_i} \Big(\langle \partial_t u_\tau - f, \varphi_\tau \rangle_{V^*,V} + a(u_\tau, \varphi_\tau) + ([u_\tau]^{(i-1)}, \varphi_\tau^{(i-1,+)})_H \Big)\, dt = 0, \tag{2.32}$$

holds for all $\varphi_\tau \in L_\tau$ and all $i = 1, \dots, N$. Further the initial condition must be fulfilled in the sense $u_\tau^{(0,-)} := u_0$, which has a contribution only through the jump-term for the interval $(t_0, t_1]$. This discretization is referred to as discontinuous Galerkin method (dG(k) method) in the literature. It is well-known that the resulting approximate solutions based on piecewise polynomials of order $k-1$ satisfy an error estimate of order $o(\delta^k)$, which is optimal (δ denotes the maximal time step size of the partitioning). Further details can be found e.g. in [48].

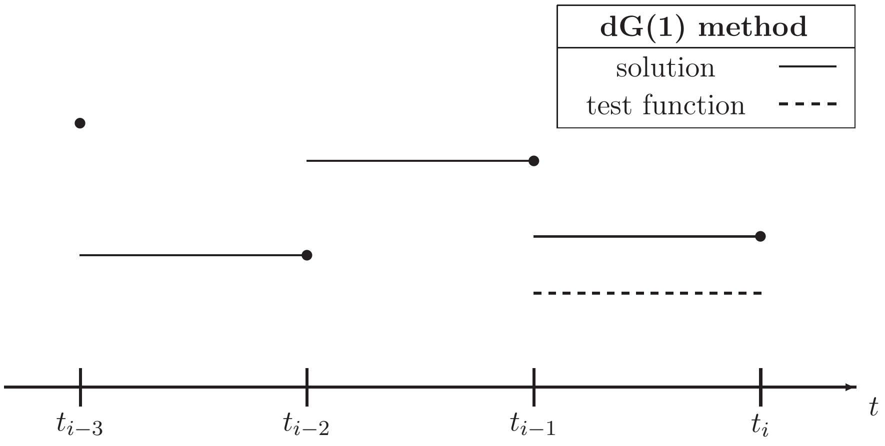

Figure 2.3: The dG(1) method: Piecewise constant trial and test functions.

In the simplest case, $k = 1$, the test and trial functions are piecewise constant functions in time, see Figure 2.3. On interval I_i, the discrete functions are defined by two elements $u_i, \varphi_i \in V$, i.e.

$$u_\tau(t)_{|(t_{i-1},t_i]} := u_i, \quad \varphi_\tau(t)_{|(t_{i-1},t_i]} := \varphi_i.$$

Since the trial function is constant, its time-derivative vanishes, i.e. $\partial_t u_{\tau|(t_{i-1},t_i)} \equiv 0$. Hence, the dG(1) method can be stated as the following time-stepping scheme: For each $i = 1, \dots, N$, find $u_i \in V$ such that

$$(u_i, \varphi)_H + (t_i - t_{i-1}) a(u_i, \varphi) = (u_{i-1}, \varphi)_H + (t_i - t_{i-1})(f(t_i), \varphi)_H, \tag{2.33}$$

for all $\varphi \in V$. Here, the time integral was evaluated using the box rule

$$\int_a^b \Psi(t)\, dt \approx Q_b(\Psi) := (b - a)\, \Psi(b). \tag{2.34}$$

In this case, problem (2.33) corresponds to the *Implicit Euler Scheme.*

It can be noted, that both the cGP(k) method and the dG(k) method have $k - 1$ unknown degrees of freedom (i.e. V-valued nodes) corresponding to each time-interval (t_{i-1}, t_i) that must be calculated. Since the approximate solutions are based on piecewise polynomials of order k in case of the cGP(k) method, the corresponding solutions are of order $k+1$, whereas the approximate solutions based on the dG(k) method consists of piecewise polynomials of order k and is related to an error of order k. Therefore the conforming discretizations that yields to the cGP(k) method should be investigated in the following.

2.4.2 Space Discretization

A mixed method for the discretization in space is considered. Therefore, finite dimensional subspaces of the continuous function spaces are defined. For the partition $\mathcal{T}_h$ of a polygonal domain $\Omega \subseteq \mathbb{R}^2$ consisting of quadrilaterals $K \in \mathcal{T}_h$ it holds that

$$\bar{\Omega} = \cup_{K \in \mathcal{T}_h} K, \quad \mathrm{Int}(K_1) \cap \mathrm{Int}(K_2) = \emptyset \;\; \forall K_1, K_2 \in \mathcal{T}_h,\, K_1 \neq K_2,$$

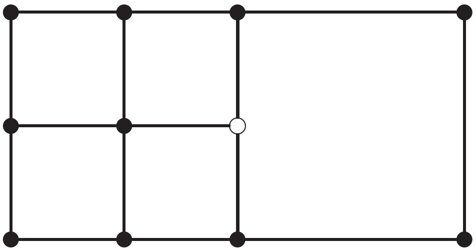

Figure 2.4: One cell neighboring a patch consisting of four refined cells with highlighted hanging node, bilinear finite element ansatz $\mathcal{Q}_1$ assumed.

where $\mathrm{Int}(K)$ denotes the interior of cell $K \in \mathcal{T}_h$. For cell K, the length parameter $h_K > 0$ is defined as its diameter, i.e. $h_K := \max_{x,y \in K} \|x - y\|$. The parameter h is defined as $h := \max_{K \in \mathcal{T}_h} h_K$.

Using Taylor-Hood elements for the discretization of the NSE, the velocity field is approximated by means of continuous, piecewise biquadratic functions and the pressure by continuous, piecewise bilinear functions. In case of homogeneous Dirichlet boundary conditions, the spaces of the form functions are defined as

$$\begin{aligned} V_h &:= \left\{ v_h \,|\, v_h \in C^0(\bar{\Omega})^2,\, v_{h_{|K}} \in \mathcal{Q}_2(K)^2 \;\forall K \in \mathcal{T}_h,\, v_h = 0 \text{ on } \partial\Omega \right\}, && (2.35) \\ Q_h &:= \left\{ p_h \,|\, p_h \in C^0(\bar{\Omega}),\, p_{h_{|K}} \in \mathcal{Q}_1(K) \;\forall K \in \mathcal{T}_h,\, \int_\Omega p_h \, dx = 0 \right\}. && (2.36) \end{aligned}$$

$\mathcal{Q}_i(K)$ denotes the polynomials with maximal degree of $i \geq 1$ in each variable defined on cell K, that reads in two space dimensions

$$\mathcal{Q}_i(K) := \left\{ u(x,y) = \sum_{0 \leq s,t \leq i} c_{st} x^s y^t,\, (x,y) \in K,\, c_{st} \in \mathbb{R} \right\}.$$

For periodic boundaries, the discrete spaces defined in (2.35) and (2.36) must be adapted to fulfill the corresponding periodicity condition (2.7). Typically, the Taylor-Hood elements are shortly denoted by $\mathcal{Q}_n/\mathcal{Q}_{n-1}$ where n denotes the polynomial degree of the velocity functions (i.e. $n = 2$ for the lowest order) and $n - 1$ denotes the polynomial degree of the pressure functions. For $n \geq 2$, the finite elements $\mathcal{Q}_n/\mathcal{Q}_{n-1}$ fulfill the Ladyshenskaja-Babušhka-Brezzi (LBB) condition [10]

$$\exists \beta > 0 : \quad \sup_{v_h \in V_h \setminus \{0\}} \frac{(\nabla \cdot v_h, p_h)}{\|v_h\|} \geq \beta \, \|p_h\| \quad \forall p_h \in Q_h \setminus \{0\}, \qquad (2.37)$$

and therefore are stable [11, 21]. In the literature, (2.37) is also denoted by discrete inf-sub condition.

In case of h-adapted meshes consisting of quadrilateral cells only, so-called *hanging nodes* exist, see Figure 2.4. These have to be treated in a way such that global conformity is guaranteed, which is a global continuity condition for the velocity and pressure functions in case of Taylor-Hood elements. To this end, a 1-irregularity condition must be fulfilled by the mesh, i.e. on each edge there may be one hanging node at most which is determined by an interpolation condition. In the following, $\mathcal{Q}_2/\mathcal{Q}_1$ elements are used as finite element space for all simulations and hanging nodes are treated as described in [25, 27].

2.4.3 Projection into Divergence-Free Spaces

The divergence-free condition in mixed method formulations of the NSE depends on the discretization. This means that a velocity field $\upsilon : \Omega \to \mathbb{R}^2$ is divergence-free in the discrete sense, if

$$(\nabla \cdot \upsilon, \varphi) = 0 \quad \forall \varphi \in V_h, \tag{2.38}$$

holds, where $V_h \subseteq V$ denotes the discrete space of the velocity functions used in the variational problem (2.11). For given velocity field $\tilde{\upsilon} \in L^2(\Omega)^2$ that does not fulfill condition (2.38), a projection step can be performed. This projection $P : L^2(\Omega)^2 \to V_h$ maps to the discrete approximate solution of the following minimization problem:

$$\min_{\upsilon \in H(div,\Omega)} \frac{1}{2} \left\| \upsilon - \tilde{\upsilon} \right\|^2_{L^2(\Omega)}, \quad \text{subject to } (\nabla \cdot \upsilon, \varphi) = 0 \quad \forall \varphi \in L^2(\Omega), \tag{2.39}$$

where

$$H(div, \Omega) := \left\{ u \,|\, u \in L^2(\Omega)^2,\ \nabla \cdot u \in L^2(\Omega) \right\}.$$

Problem (2.39) defines a L^2-projection under the constraint of υ to be divergence-free. The associated Lagrange functional is defined by

$$\mathcal{L} : H(div, \Omega) \times L^2(\Omega) \to \mathbb{R},$$

$$\mathcal{L}(\upsilon, \lambda) := \frac{1}{2}(\upsilon - \tilde{\upsilon}, \upsilon - \tilde{\upsilon}) + (\nabla \cdot \upsilon, \lambda).$$

A necessary condition for a solution of the optimization problem (2.39) is the stationarity of the Lagrange functional:

$$\begin{aligned} \mathcal{L}_\upsilon(\upsilon, \lambda)\varphi &= (\upsilon - \tilde{\upsilon}, \varphi) + (\nabla \cdot \varphi, \lambda) = 0 \quad \forall \varphi \in H(div, \Omega), \\ \mathcal{L}_\lambda(\upsilon, \lambda)\psi &= (\nabla \cdot \upsilon, \psi) = 0 \quad \forall \psi \in L^2(\Omega). \end{aligned}$$

This condition is connected to the following saddle point problem in the Hilbert spaces $H(div, \Omega)$ equipped with the graph norm of the divergence operator

$$\|\upsilon\|_{H(div,\Omega)} := (\|\upsilon\|^2_{L^2(\Omega)} + \|\nabla \cdot \upsilon\|^2_{L^2(\Omega)})^{1/2}.$$

For given $\tilde{\upsilon} \in L^2(\Omega)^2$, find $(\upsilon, \lambda) \in H(div, \Omega) \times L^2(\Omega)$ such that

$$\begin{aligned} a(\upsilon, \varphi) + b(\varphi, \lambda) &= (\tilde{\upsilon}, \varphi) \quad \forall \varphi \in H(div, \Omega), \\ b(\upsilon, \psi) &= 0 \qquad \forall \psi \in L^2(\Omega), \end{aligned} \tag{2.40}$$

with the bilinear operators $a : L^2(\Omega)^2 \times L^2(\Omega)^2 \to \mathbb{R}$, $(u, v) \mapsto a(u, v) := (u, v)_{L^2(\Omega)}$ and $b : H(div, \Omega) \times L^2(\Omega) \to \mathbb{R}$, $(u, \lambda) \mapsto b(u, \lambda) := (\nabla \cdot u, \lambda)$. This saddle point problem corresponds to a mixed formulation of Poisson's problem, as described in [9], for example. The operator $a(\cdot, \cdot)$ is coercive, since for $u \in H(div, \Omega)$ with $\nabla \cdot u = 0$, it holds $a(u, u) = (u, u) = \|u\|^2_{L^2(\Omega)} = \|u\|^2_{L^2(\Omega)} + \|\nabla \cdot u\|^2_{L^2(\Omega)} = \|u\|^2_{H(div,\Omega)}$. For the operator $b(\cdot, \cdot)$ the inf-sup condition

$$\exists \beta > 0 : \qquad \sup_{\upsilon \in H(div,\Omega) \setminus \{0\}} \frac{b(\upsilon, \lambda)}{\|\upsilon\|_{H(div,\Omega)}} \geq \beta \left\| \lambda \right\|, \quad \forall \lambda \in L \setminus \{0\},$$

can be proved, cf. [9]. The discrete spaces V_h and Q_h defined by (2.35) and (2.36) are subspaces of $H(div,\Omega)$ and $L^2(\Omega)$, respectively and fulfill the LBB condition (2.37). Therefore, the discrete solution $(\upsilon_h, \lambda_h) \in V_h \times Q_h$ of the saddle point problem

$$\begin{aligned} a(\upsilon_h, \varphi) + b(\varphi, \lambda_h) &= (\tilde{\upsilon}, \varphi) \quad \forall \varphi \in V_h, \\ b(\upsilon_h, \psi) &= 0 \qquad \forall \psi \in Q_h, \end{aligned} \tag{2.41}$$

has a unique solution $(\upsilon_h, \lambda_h) \in V_h \times Q_h$. By the solution of problem (2.41) a discrete divergence-free initial function $\upsilon_h := P(\tilde{\upsilon}) \in V_h$ can be calculated with smallest difference to the given function $\tilde{\upsilon} \in L^2(\Omega)^2$. For the solution $(P(\tilde{\upsilon}_0), \lambda_h) \in V_h \times Q_h$ of the discrete problem (2.41) the following error characterization holds [9]:

$$\begin{aligned} & \|\upsilon - \upsilon_h\|_{H(div,\Omega)} + \|\lambda - \lambda_h\|_{L^2(\Omega)} \\ \leq \; & C \left(\inf_{\varphi_h \in V_h} \|\upsilon - \varphi_h\|_{H(div,\Omega)} + \inf_{\psi_h \in Q_h} \|\lambda - \psi_h\|_{L^2(\Omega)} \right), \end{aligned}$$

where $(\upsilon, \lambda) \in H(div,\Omega) \times L^2(\Omega)$ denotes the solution of the continuous problem (2.40).

2.5 Numerical Solver

The discretization of the Navier-Stokes equations in terms of finite element methods in space and time as described in Section 2.4, results in a finite set of nonlinear equations that characterize approximate solutions of the continuous problem. Newton's method can be used to solve that system of nonlinear equations and leads to a sequence of large sparse linear problems. The accuracy up to which these linear problems must be solved can be determined for each loop of the iteration based on inexact Newton methods. The method that was used to calculate the solutions depicted in Chapters 4 and 5 is shortly summarized in the following.

Let $F : X \to Y$ denote a differentiable function that has a zero $x \in X$. For a given guess $x_0 \in X$, Newton's method defines a recursion to approximate the zero x:

$$x_{i+1} := x_i + \underbrace{F'(x_i)^{-1}(-F(x_i))}_{=:c_i}, \quad i = 0, 1, 2, \dots .$$

The calculation of the correction term c_i requires the solution of a linear problem for each iteration step:

$$F(x_i) + F'(x_i)c_i = 0. \tag{2.42}$$

In case of inexact methods, only approximate solutions for problem (2.42) are calculated. Given the so-called *forcing term* $\eta_i \in [0, 1)$, the approximations $\tilde{c}_i \approx c_i$ must fulfill

$$\left\| F(x_i) + F'(x_i)\tilde{c}_i \right\| \leq \eta_i \left\| F(x_i) \right\|. \tag{2.43}$$

Eisenstat and Walker [17] proposed the following choice for the forcing term η_i:

$$\eta_i := \frac{\|F(x_i) - F(x_{i-1}) - F'(x_{i-1})\tilde{c}_{i-1}\|}{\|F(x_{i-1})\|}, \quad i = 1, 2, \dots$$

which is defined in terms of the nonlinear residuals $F(x_{i-1})$ and $F(x_i)$. The term $F(x_{i-1}) + F'(x_{i-1})\tilde{c}_{i-1}$ represents the linear residual.

The resulting linear problems are solved iteratively using a preconditioned generalized minimal residual method (GMRES) [37]. The algebraic system of linear equations is preconditioned using an incomplete LU factorization [33, 34]. Numerical tests showed that the required accuracy of the first few Newton iterations could be chosen significantly smaller than the desired accuracy of the nonlinear solution itself. This lead to a reduction of the calculation time needed for the solution of the linear problems. The number of Newton steps of the inexact method was not increased compared to the standard method in which all linear problems (2.42) are solved with the same accuracy. For the numerical results presented later, the forcing term of the inexact method for the first iteration was chosen to be $\eta_0 := 1.0e - 4$.

3 Goal-Oriented Error Estimation

Many investigations of problems modeled by partial differential equations are targeted at the evaluation of local quantities such as point values or integrals of the solution over small regions. In such situations, the intention is to obtain good approximations with respect to these user-defined measures rather than global norms. The Dual Weighted Residual (DWR) method [2, 20] provides a generic framework to construct goal-oriented adaptive methods. This includes an a posteriori error estimator for the error in the quantity of interest defined in terms of the *goal functional*. The sensitivity of the goal functional with respect to perturbations of the solution is given through the solution of the *dual problem*. Additionally, the error contribution of each cell of the underlying mesh can be estimated and used to control the mesh-adaptation process, leading to efficient discrete models.

For the discretization of instationary problems in terms of space-time finite element methods, continuous variational problems based on integrals in space and time represent a natural setting. Solutions of the continuous problems typically are continuous in time, whereas the test functions need to be measurable in time only and therefore may be discontinuous. Hence, conforming discretizations can be defined that allow the decoupling of the global problem into a sequence of smaller problems, which can be solved successively by iterating through the time intervals similar to time-stepping methods based on finite difference schemes.

The discrete trial functions can be defined either as discontinuous functions in time (leading to non-conforming methods, see e.g. [40]) or as continuous functions. In the following, conforming discretizations for both primal and dual problems based on continuous trial functions and discontinuous test functions are investigated. The differing test and trial spaces lead to Petrov-Galerkin methods and require some modifications of the a posteriori error estimators given by the DWR method.

In this chapter an abstract error characterization is presented based on which computable error estimators for the error in a user-defined output functional can be derived. Since the evaluation of the error characterizations depends on the knowledge of unknown quantities, some aspects of different approximation strategies are discussed. Finally, a posteriori error estimators for the Navier-Stokes equations are presented. The corresponding error indicators allow to distinguish between between errors related to the discretization in space time. These can be used for mesh adaptation strategies where the spatial and temporal dimensions are treated separately.

3.1 Error Characterization for Petrov-Galerkin Approximations

The error characterization given in the following theorem represents the basis of goal-oriented error estimators as described later.

Theorem 4. *Let $X \subseteq Y$ be two normed spaces with dense inclusion. Let $\mathcal{F}$ be a three times continuously Fréchet differentiable functional on X and $\mathcal{F}'(x) \in Y^*$ for any $x \in X$. Let $\hat{x} \in X$ be a stationary point of $\mathcal{F}$ in the sense that*

$$\mathcal{F}'(\hat{x})y = 0 \quad \forall y \in Y. \tag{3.1}$$

A Petrov-Galerkin $\hat{x}_h \in X_h$ approximation in discrete spaces $X_h \subseteq X$ and $Y_h \subseteq Y$ is a solution of

$$\mathcal{F}'(\hat{x}_h)y_h = 0 \quad \forall y_h \in Y_h. \tag{3.2}$$

Then for arbitrary $\varphi_h \in Y_h$ it holds that

$$\mathcal{F}(\hat{x}) - \mathcal{F}(\hat{x}_h) = \frac{1}{2}\mathcal{F}'(\hat{x}_h)(\hat{x} - \hat{x}_h - \varphi_h) + \mathcal{R}_h, \tag{3.3}$$

with the remainder term $\mathcal{R}_h$ defined by

$$\mathcal{R}_h := \frac{1}{2}\int_0^1 s(s-1)\cdot \mathcal{F}'''(\hat{x}_h + se)(e,e,e)\ ds, \quad e := \hat{x} - \hat{x}_h.$$

Proof. The existence of a solution $\hat{x} \in X$ of (3.1) and a solution $\hat{x}_h \in X_h$ of (3.2) is assumed. For the parametrized smooth curve $\Phi : [0,1] \to X$, $s \mapsto \Phi(s) := \hat{x}_h + s(\hat{x} - \hat{x}_h)$ the first and second derivatives are $\Phi' \equiv \hat{x} - \hat{x}_h$ and $\Phi'' \equiv 0$, respectively. The line integral along the curve Φ can be written by the fundamental theorem of calculus [52] as

$$\mathcal{F}(\hat{x}) - \mathcal{F}(\hat{x}_h) = \int_0^1 \mathcal{F}'(\Phi(s))\Phi'(s)\, ds.$$

For the discretization error $e := \hat{x} - \hat{x}_h \in X \subseteq Y$ it holds that $\mathcal{F}'(\hat{x})e = 0$ by (3.1) and therefore

$$\mathcal{F}(\hat{x}) - \mathcal{F}(\hat{x}_h) = \frac{1}{2}\mathcal{F}'(\hat{x}_h)e + \int_0^1 \mathcal{F}'(\Phi(s))\Phi'(s)\, ds - \frac{1}{2}\left(\mathcal{F}'(\hat{x}_h)e + \mathcal{F}'(\hat{x})e\right).$$

For a two times continuously differentiable function $f : \mathbb{R} \to \mathbb{R}$, by applying two times integration by parts

$$\int_0^1 f(s)\, ds - \frac{1}{2}\left(f(0) + f(1)\right) = -\int_0^1 \left(s - \frac{1}{2}\right)\cdot f'(s)\, ds = \frac{1}{2}\int_0^1 s(s-1)\cdot f''(s)\, ds.$$

For $f(s) := \mathcal{F}'(\Phi(s))\Phi'(s)$ it holds

$$\begin{aligned} f''(s) &= \left(\frac{d}{ds}\right)^2 \left(\mathcal{F}'(\Phi(s))e\right) \\ &= \frac{d}{ds}\left(\mathcal{F}''(\Phi(s))(e,e)\right) \\ &= \mathcal{F}'''(\Phi(s))(e,e,e), \end{aligned}$$

and hence

$$\mathcal{F}(\hat{x}) - \mathcal{F}(\hat{x}_h) = \frac{1}{2}\mathcal{F}'(\hat{x}_h)e + \underbrace{\frac{1}{2}\int_0^1 s(s-1)\cdot\mathcal{F}'''(\hat{x}_h + se)(e,e,e)\,ds}_{=:\mathcal{R}_h}.$$

Due to (3.2) and the linearity of $\mathcal{F}'(\hat{x}_h)(\cdot)$ for arbitrary $\varphi_h \in Y_h$ holds

$$\begin{aligned}\mathcal{F}(\hat{x}) - \mathcal{F}(\hat{x}_h) &= \frac{1}{2}\mathcal{F}'(\hat{x}_h)(e - \varphi_h) + \mathcal{R}_h \\ &= \frac{1}{2}\mathcal{F}'(\hat{x}_h)(\hat{x} - \hat{x}_h - \varphi_h) + \mathcal{R}_h,\end{aligned}$$

which completes the proof. ☐

Remark 5. In the case of Galerkin approximations, the two discrete spaces in the definition of problem (3.2) coincide ($X_h = Y_h$). In this case, the discrete solution $\hat{x}_h$ in the direction expression on the right-hand side of equation (3.3) can be omitted, i.e.

$$\mathcal{F}(\hat{x}) - \mathcal{F}(\hat{x}_h) = \frac{1}{2}\mathcal{F}'(\hat{x}_h)(\hat{x} - \varphi_h) + \mathcal{R}_h,$$

for arbitrary $\varphi \in X_h$.

The error characterization given by Theorem 4 represents a fundamental component for goal-oriented adaptive techniques since it enables the quantification of the error of a Petrov-Galerkin approximation with respect to a user-defined output functional. In the following, the general concept is explained based on an abstract parabolic problem. Let V and H denote separable Hilbert spaces such that (V, H, V^*) forms a Gelfand triple. Furthermore, let $a : V \times V \to \mathbb{R}$ denote a continuous bilinear form, i.e. there exists $\alpha > 0$ such that

$$|a(u,v)| \leq \alpha \|u\|_V \|v\|_V \quad \forall u, v \in V,$$

and assume further that Gårding's inequality holds, i.e. for $\beta > 0$ and $\gamma \geq 0$

$$a(u,u) + \gamma \|u\|_H^2 \geq \beta \|u\|_V^2 \quad \forall u \in V.$$

For a given force term $f \in L^2(0,T;V^*)$, initial condition $u_0 \in H$ and $T > 0$, the following parabolic evolution problem has a unique solution [29]: Find $u \in W(0,T)$ such that

$$\rho(u)(\varphi) := \int_0^T \Big(\langle \partial_t u - f, \varphi\rangle_{V^*,V} + a(u,\varphi)\Big)\,dt + (u_{|t=0} - u_0, \varphi_{|t=0})_H = 0, \quad (3.4)$$

for all $\varphi \in L^2(0,T;V)$. In the following the short notations $W := W(0,T)$, $L := L^2(0,T;V)$ and $L^* = L^2(0,T;V^*)$ are used. Let $u \in W$ denote the solution of problem (3.4) and let $J(u)$ denote the quantity of interest, where the goal functional $J : L \to \mathbb{R}$ is defined by

$$J(u) := \int_0^T \left\langle j^{(1)}, u\right\rangle_{V^*,V} dt + (j^{(2)}, u_{|t=T})_H,$$

with $j^{(1)} \in L^*$ and $j^{(2)} \in H$. A Petrov-Galerkin approximation of problem (3.4) in finite dimensional spaces $W_h \subseteq W$ and $L_h \subseteq L$ is characterized by

$$u_h \in W_h : \quad \rho(u_h)(\varphi_h) = 0 \quad \forall \varphi_h \in L_h. \tag{3.5}$$

The error in J of a solution u_h can be characterized by Theorem 4. For this purpose, the Lagrange functional $\mathcal{L} : W \times W \to \mathbb{R}$ is introduced:

$$\mathcal{L}(u, z) := J(u) + \rho(u)(z). \tag{3.6}$$

A stationary point $(u, z) \in W \times W$ fulfills

$$\mathcal{L}'(u, z)(\varphi, \psi) = \mathcal{L}_u(u, z)\varphi + \mathcal{L}_z(u, z)\psi = 0 \quad \forall (\varphi, \psi) \in W \times W. \tag{3.7}$$

Due to the linearity of the derivatives, this stationary condition can be equivalently formulated by two independent conditions:

$$\begin{aligned} \mathcal{L}_u(u, z)\varphi &= 0 \quad \forall \varphi \in W, \\ \mathcal{L}_z(u, z)\psi &= 0 \quad \forall \psi \in W. \end{aligned}$$

Due to the linearity of the residual function ρ in the second argument and an extension of the test functions from space W to L, the first condition for a stationary point has the form

$$\mathcal{L}_z(u, z)\psi = \rho(u)(\psi) = 0 \quad \forall \psi \in L, \tag{3.8}$$

and corresponds to problem (3.4), which is denoted as *primal problem* in this context. The extension of the space of test functions from W to L can be justified by the fact that the inclusion $W \subseteq L$ is dense (see Lemma 1) and $\rho(u)(\cdot)$ is continuous on L. The latter can be shown as follows: For the bilinear operator $a(\cdot, \cdot)$ there exists a corresponding operator $A : V \to V^*$ defined by

$$u \in V : \quad \langle Au, v \rangle_{V^*,V} = a(u, v) \quad \forall v \in V. \tag{3.9}$$

Then for any $u \in L^2(0, T; V)$, it holds that $Au(t) \in V^*$ for almost every t. Since the bilinear operator $a(\cdot, \cdot)$ is bounded, for any $v \in L^2(0, T; V)$

$$\begin{aligned} \langle Au, v \rangle_{L^*,L} &= \int_0^T \langle Au(t), v(t) \rangle_{V^*,V} \, dt \\ &= \int_0^T a(u(t), v(t)) \, dt \\ &\leq \int_0^T \alpha \left\| u(t) \right\|_V \left\| v(t) \right\|_V \, dt \\ &\leq \alpha \left(\int_0^T \left\| u(t) \right\|_V^2 \, dt \right)^{1/2} \left(\int_0^T \left\| v(t) \right\|_V^2 \, dt \right)^{1/2} \\ &= \alpha \left\| u \right\|_L \left\| v \right\|_L . \end{aligned}$$

Hence, $Au \in L^*$ and therefore $(\partial_t u - f + Au) \in L^*$. Using integration by parts, see equation (2.1), the second stationary condition of (3.7) reads

$$\mathcal{L}_u(u, z)\varphi = \int_0^T \left(\left\langle j^{(1)} - \partial_t z, \varphi \right\rangle_{V^*,V} + a_u(u, z)\varphi \right) dt + (j^{(2)} + z_{|t=T}, \varphi_{|t=T})_H = 0,$$

for all $\varphi \in W$. The adjoint operator $A_u^* : V \to V^*$ for $a(\cdot,\cdot)$ fulfills for each $z \in V$

$$\langle A_u^* z, \varphi \rangle_{V^*,V} = a_u(u,z)\varphi \quad \forall \varphi \in V.$$

In case of a bilinear operator $a(\cdot,\cdot)$, it holds $a_u(u,z)\varphi = a(\varphi, z)$ and the adjoint operator $A_u^* z \in L^*$ can be defined analogously to equation (3.9). Introducing

$$\rho_u^*(z)(\varphi) := \int_0^T \left\langle j^{(1)} - \partial_t z + A_u^* z, \varphi \right\rangle_{V^*,V} dt + (j^{(2)} + z_{|t=T}, \varphi_{|t=T})_H,$$

the so-called *dual problem* can be stated in shorter notation: Find $z \in W$ such that

$$\rho_u^*(z)(\varphi) = 0 \quad \forall \varphi \in L, \tag{3.10}$$

where the space of test functions has been extended from W to L analogously to the case of the primal problem. As a result, the stationary condition (3.7) can be stated in terms of the residuals of the primal and dual problems:

$$(u,z) \in W \times W : \quad \rho(u)(\psi) + \rho_u^*(z)(\varphi) = 0 \quad \forall (\varphi, \psi) \in L \times L. \tag{3.11}$$

For nonlinear $a(\cdot,\cdot)$ necessary conditions for the existence of $Au \in L^*$ and $A^* z \in L^*$ as well as statements on existence and uniqueness of solutions for problem (3.7) can be found in [19, 29]. With these definitions of the primal and dual residual, the fundamental error characterization for goal-oriented adaptive methods can be stated. It can be proven analogously to the variant for Galerkin approximations described in [2].

Corollary 6. *(Goal-oriented error characterization) Let $J : L \to \mathbb{R}$ be a three times continuously Fréchet differentiable functional. Let $u \in W$ denote the solution of problem (3.4) and $u_h \in W_h \subseteq W$ a Petrov-Galerkin approximation with test space $L_h \subseteq L$. The error in the goal functional J can be characterized by*

$$J(u) - J(u_h) = \frac{1}{2}\left(\rho(u_h)(z + z_h - \varphi_h) + \rho_{u_h}^*(z_h)(u - u_h - \psi_h)\right) + \mathcal{R}_3, \tag{3.12}$$

with arbitrary $\varphi_h, \psi_h \in L_h$. The remainder $\mathcal{R}_3$ is of third order in the error $e := (e_u, e_z)^T$, where $e_u := u - u_h$ and $e_z := z - z_h$:

$$\mathcal{R}_3 := \int_0^1 \mathcal{L}'''(u_h + s e_u, z_h + s e_z)(e,e,e)s(s-1)\, ds. \tag{3.13}$$

z and z_h denote the continuous solution and the corresponding discrete Petrov-Galerkin approximation of problem (3.10), respectively.

Remark 7. For the conforming discrete spaces $W_h \subseteq W$ and $L_h \subseteq L$ it may hold that $W_h \nsubseteq L_h$, although $W \subseteq L$. Consequently, the discrete solutions $u_h, z_h \in W_h$ of the discrete primal and dual problems are not necessarily included in the discrete test space L_h.

Proof. With the residuals of the primal and dual problems defined as before, a stationary point $(u,z) \in W \times W$ of the Lagrange functional $\mathcal{L}(u,z)$ as defined in (3.6) fulfills condition (3.11), i.e.

$$\mathcal{L}'(u,z)(\varphi,\psi) = \rho(u)(\psi) + \rho_u^*(z)(\varphi) = 0 \quad \forall(\varphi,\psi) \in L \times L.$$

For finite dimensional subspaces $W_h \subseteq W$ and $L_h \subseteq L$, an approximate solution $(u_h,z_h) \in W_h \times W_h$ of the stationary point (u,z) is characterized by

$$\mathcal{L}'(u_h,z_h)(\varphi_h,\psi_h) = \rho(u_h)(\psi_h) + \rho_{u_h}^*(z_h)(\varphi_h) = 0 \quad \forall(\varphi_h,\psi_h) \in L_h \times L_h.$$

To apply Theorem 4, define $x := (u,z) \in X := W \times W$, $Y := L \times L$ and $\mathcal{F} : X \to \mathbb{R}$ by $\mathcal{F}(x) := \mathcal{L}(u,z)$. Furthermore, let the $x_h := (u_h,z_h) \in X_h := W_h \times W_h$ and $Y_h := L_h \times L_h$. Then

$$\mathcal{L}(u,z) - \mathcal{L}(u_h,z_h) = \frac{1}{2}\mathcal{L}'(u_h,z_h)(u - u_h - \varphi_h, z - z_h - \psi_h) + \mathcal{R}_3, \tag{3.14}$$

with remainder term $\mathcal{R}_3 := \int_0^1 \mathcal{L}'''(u_h + se_u, z_h + se_z)(e,e,e)s(s-1)\,ds$, where $e := (e_u,e_z)$, $e_u := u - u_h$, $e_z := z - z_h$ and arbitrary $\varphi_h,\psi_h \in L_h$.

For stationary points $(u,z) \in W \times W$ it holds that $\mathcal{L}(u,z) = J(u) + \rho(u)(z) = J(u)$ since $\rho(u)(z) = 0$. For for the Petrov-Galerkin approximation $(u_h,z_h) \in W_h \times W_h$, $\mathcal{L}(u_h,z_h) = J(u_h) + \rho(u_h)(z_h)$, analogously. Hence, equation (3.14) can equivalently be written as:

$$J(u) - J(u_h) - \rho(u_h)(z_h) = \frac{1}{2}\left(\rho(u_h)(z - z_h - \psi_h) + \rho_{u_h}^*(z_h)(u - u_h - \varphi_h)\right) + \mathcal{R}_3, \tag{3.15}$$

for arbitrary $(\varphi_h,\psi_h) \in L_h \times L_h$. Note that the residuals $\rho(u_h)(\cdot)$ and $\rho_{u_h}^*(z_h)(\cdot)$ vanish on L_h. Since the solutions $u_h, z_h \in W_h$ the residuals $\rho(u_h)(z_h)$ and $\rho_{u_h}^*(z_h)(u_h)$ cannot be neglected (see Remark 7). Adding $\rho(u_h)(z_h)$ to both sides of (3.15) yields the error characterization (3.12).

Recalling the definition of the Lagrange functional $\mathcal{L}(u,z) := J(u) + \rho(u)(z)$, the remainder term $\mathcal{R}_3$ as defined in (3.13) can be verified by

$$\begin{aligned}
& \mathcal{L}'''(u_h + se_u, z_h + se_z)(e,e,e) \\
= \; & \left(\frac{d}{ds}\right)^3 \mathcal{L}(u_h + se_u, z_h + se_z) \\
= \; & \left(\frac{d}{ds}\right)^3 \big(J(u_h + se_u) + \rho(u_h + se_u)(z_h + se_z)\big) \\
= \; & \left(\frac{d}{ds}\right)^2 \big(J'(u_h + se_u)e_u + \rho'(u_h + se_u)e_u(z_h + se_z) + \rho(u_h + se_u)e_z\big) \\
= \; & \frac{d}{ds}\big(J''(u_h + se_u)(e_u,e_u) + \rho''(u_h + se_u)(e_u,e_u)(z_h + se_z) \\
& \quad +2\rho'(u_h + se_u)(e_u,e_z)\big) \\
= \; & J'''(u_h + se_u)(e_u,e_u,e_u) + \rho'''(u_h + se_u)(e_u,e_u,e_u)(z_h + se_z) \\
& \quad +3\rho''(u_h + se_u)(e_u,e_u,e_z).
\end{aligned}$$

This implies that the remainder term vanishes in the case of a linear goal functional and linear primal problem. □

Remark 8. If the discrete test and trial spaces coincide, i.e. $W_h = L_h$, it holds that $\rho(u_h)(\varphi_h) = \rho^*_{u_h}(z_h)(\psi_h) = 0$ for all $\varphi_h, \psi_h \in W_h$. In that case, the error characterization (3.12) results in the variant described in [2]:

$$J(u) - J(u_h) = \frac{1}{2}\big(\rho(u_h)(z - \varphi_h) + \rho^*_{u_h}(z_h)(u - \psi_h)\big) + \mathcal{R}_3.$$

The following characterizations are defined only in terms of one of the two unknown exact solutions $u, z \in W$ of the primal and dual problems.

Corollary 9. *(Simplified error representations) The error in J can be characterized by the following two simplified representations:*

$$\begin{aligned} J(u) - J(u_h) &= \rho(u_h)(z - \varphi_h) - \mathcal{R}_2, && (3.16)\\ J(u) - J(u_h) &= \rho^*_{u_h}(z_h)(u - u_h - \psi_h) + \rho(u_h)(z_h - \varphi_h) + \tilde{\mathcal{R}}_2, && (3.17) \end{aligned}$$

for all $\varphi_h, \psi_h \in L_h$ with remainder terms

$$\mathcal{R}_2 := \int_0^1 \big(\rho''(u_h + se_u)(e_u, e_u)z + J''(u_h + se_u)(e_u, e_u)\big)\, s\, ds, \quad \tilde{\mathcal{R}}_2 := 2\mathcal{R}_3 + \mathcal{R}_2,$$

that are of second order in the error $e := (e_u, e_z)^T$.

Proof. The identity (3.16) can be verified as in the case of Galerkin approximations, cf. [2], by integration by parts:

$$\begin{aligned} \mathcal{R}_2 &= \int_0^1 \big(\rho''(u_h + se_u)(e_u, e_u)z + J''(u_h + se_u)(e_u, e_u)\big)\, s\, ds \\ &= -\int_0^1 \big(\rho'(u_h + se_u)e_u z + J'(u_h + se_u)e_u\big)\, ds + \underbrace{\rho'(u)e_u z + J'(u)e_u}_{=\rho^*_u(z)e_u = 0} \\ &= -\left(\underbrace{\rho(u)z}_{=0} + J(u) - \rho(u_h)z - J(u_h)\right) \\ &= -J(u) + J(u_h) + \rho(u_h)(z). \end{aligned}$$

Then the identity (3.16) follows from $\rho(u_h, \varphi_h) = 0 \;\forall \varphi_h \in L_h$. By the error characterization (3.12) it holds:

$$\begin{aligned} & 2(J(u) - J(u_h)) \\ =\; & \rho(u_h)(z + z_h - \varphi_h) + \rho^*_{u_h}(z_h)(u - u_h - \psi_h) + 2\mathcal{R}_3 \\ =\; & \rho(u_h)(z - \varphi_h) - \mathcal{R}_2 + \rho(u_h)(z_h) + \rho^*_{u_h}(z_h)(u - u_h - \psi_h) + 2\mathcal{R}_3 + \mathcal{R}_2 \\ =\; & J(u) - J(u_h) + \rho(u_h)(z_h) + \rho^*_{u_h}(z_h)(u - u_h - \psi_h) + 2\mathcal{R}_3 + \mathcal{R}_2. \end{aligned}$$

Subtracting $J(u) - J(u_h)$ on both sides and the fact that $\rho(u_h)(\varphi_h) = 0$ holds for any $\varphi_h \in L_h$, proves the identity (3.17). ☐

3.2 A Posteriori Error Estimation

Based on Corollaries 6 and 9, the discretization error of approximate solutions with respect to user-defined goal functionals can be characterized in terms of the unknown exact solutions $u, z \in W$ of the primal and dual problems and remainder terms. To calculate estimations for this error it is necessary to consider modifications of the error characterization (3.12) or one of the simplified variants (3.16)-(3.17).

The remainder terms $\mathcal{R}_2, \tilde{\mathcal{R}}_2$ and $\mathcal{R}_3$ are typically neglected. These terms vanish analytically for many applications, e.g. in the case of a linear primal problem and linear goal functional. The unknown exact solutions $u, z \in W$ can be replaced by approximations $u \approx \hat{u}$ and $z \approx \hat{z}$. It is essential that these approximations are not functions in the discrete test space of the Petrov-Galerkin approximation, i.e. $\hat{u}, \hat{z} \notin L_h$, since the related error estimates would always be zero. Based on these modifications, the error characterization $E(u_h) \approx J(u) - J(u_h)$ obtained from (3.12) has the form:

$$E(u_h) \quad := \quad \frac{1}{2}\left(\rho(u_h)(\hat{z} + z_h - \varphi_h) + \rho^*_{u_h}(z_h)(\hat{u} - u_h - \psi_h)\right), \tag{3.18}$$

with arbitrary functions $\varphi_h, \psi_h, \alpha_h \in L_h$. Based on the simplified characterizations (3.16) and (3.17), evaluable error estimators can be defined analogously. Neglecting the remainder terms and replacing the unknown exact solutions by approximations the two error representations have the form

$$E_P(u_h) \quad := \quad \rho(u_h)(\hat{z} - \varphi_h), \tag{3.19}$$

$$E_D(u_h) \quad := \quad \rho^*_{u_h}(z_h)(\hat{u} - u_h - \psi_h) + \rho(u_h)(z_h - \varphi_h), \tag{3.20}$$

for arbitrary $\varphi_h, \psi_h \in L_h$.

Remark 10. For the discrete test space L_h and the trial space W_h of Petrov-Galerkin methods it may hold that $W_h \nsubseteq L_h$. In this case, the finite element solutions $u_h, z_h \in W_h$ can be used as replacements for the primal and dual solutions, i.e. $\hat{u} := u_h$ and $\hat{z} := z_h$ without leading to vanishing error estimates. The error representation (3.18) then has the form

$$\begin{aligned} E(u_h) \quad &= \quad \frac{1}{2}\left(\rho(u_h)(z_h + z_h - 2\varphi_h) + \rho^*_{u_h}(z_h)(u_h - u_h - \psi_h)\right) \\ &= \quad \rho(u_h)(z_h - \varphi_h), \end{aligned} \tag{3.21}$$

for arbitrary $\varphi_h \in L_h$ and $\psi_h \equiv 0$. In this case, the simplified characterization E_P given in equation (3.19) and the characterization characterization (3.21) coincide.

3.2.1 Evaluation Aspects

Essential questions concerning the quality of the error estimations and the efficiency of resulting adaptive methods are related to the replacements $\hat{u}, \hat{z}$ of the unknown exact solutions u, z leading to a posteriori error estimations. How should the exact solutions be approximated such that the corresponding estimates are reliable? Does mesh refinement based on these estimates lead to efficient discrete models that allow accurate determination of the user-defined quantity of interest? To tackle these questions, a systematic comparison of several evaluation strategies has been carried out based on scenarios with known analytical solutions, see Chapter 4.

In the following, different strategies to determine approximations $\hat{u} \approx u$ and $\hat{z} \approx z$ are discussed. In general, these approaches apply similarly to the temporal and the spatial structures. The calculation of finite element solutions in higher-order spaces is one obvious option, but the related computational cost is comparably high. A block-strategy is proposed, in which local Dirichlet problems are solved, nested in a global defect-correction loop. The computational effort can be controlled by an adequate stopping criterion for this iterative method. Furthermore, interpolation strategies are presented that are widely used, since the corresponding approximations can be calculated at very low computational cost. In the following, the approximation with respect to the spatial structure is investigated. For this purpose, the case of Galerkin approximations of stationary problems and a discrete trial and test space denoted by $V_h \subseteq V$ is assumed. The treatment with respect to the temporal structure is discussed subsequently.

3.2.1.1 Higher-Order Finite Element Solution

Let $u_h \in V_h$ and $z_h \in V_h$ denote the Galerkin approximations of the primal and dual solutions $u, z \in V$. The replacements of these unknown exact solutions are defined as the finite element solutions $\hat{u}, \hat{z} \in \hat{V}_h$ in a higher-order finite element space $\hat{V}_h \subseteq V$. The residuals that need to be evaluated for the a posteriori error representations (3.18), (3.19) and (3.20) as well as related error indicators are

$$\rho(u_h)(\hat{z} - I_h(\hat{z})), \quad \rho^*_{u_h}(z_h)(\hat{u} - I_h(\hat{u})).$$

The discrete functions $\varphi_h, \psi_h \in V_h$ are defined in terms of an interpolation operator

$$I_h : V \to V_h, \tag{3.22}$$

e.g. by nodal interpolation. This strategy leads to accurate approximations of the unknown quantities in the error representations, but the related computational effort is considerable. A drawback is that although higher-order solutions of the primal and dual problems are calculated, the estimations characterize the solution of u_h only.

3.2.1.2 Block Strategy

The block strategy represents a compromise with respect to computational cost and accuracy between the calculation of finite element approximations in higher-order finite element spaces and methods of pure interpolation. Instead of solving the globally coupled problem, local auxiliary problems are examined. This has successfully been applied to Poisson's problem in the framework of error estimators for global error norms [3, 50]. In the following, the solution of local Dirichlet problems embedded in a global defect-correction loop associated to the considered higher-order finite element discretization is discussed.

In the case of the Navier-Stokes equations, the divergence-free condition of the primal and the dual problem can be considered in terms of a mixed method, where

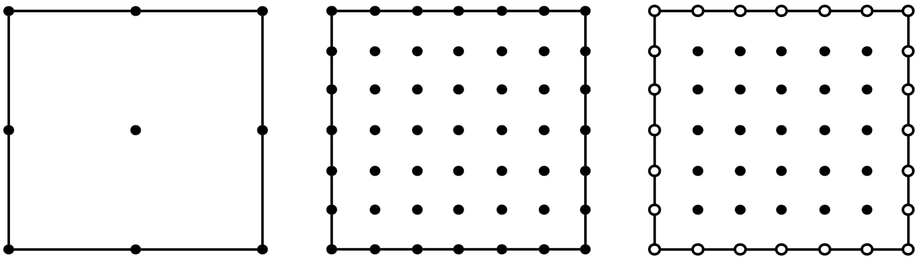

Figure 3.1: DOFs corresponding to initial (left) and higher-order FE space (middle) located within one cell; highlighted DOFs on the cell's boundary (right).

the discrete function spaces are defined as stable pair of higher-order finite element spaces $\hat{V}_h \times \hat{Q}_h \subset V \times Q$ (e.g. Taylor-Hood elements). Here, V denotes the velocity space and Q the pressure space. This discretization leads to system matrices $\mathcal{A}$ of the following form (after a permutation of the degree of freedom numbering, if necessary):

$$\underbrace{\begin{bmatrix} A & B^T \\ B & 0 \end{bmatrix}}_{=:\mathcal{A}} \begin{bmatrix} z \\ q \end{bmatrix} = \begin{bmatrix} j^{(1)} \\ 0 \end{bmatrix},$$

where A represents the convection-diffusion parts of the PDE, B and B^T represent discrete divergence and gradient matrices. $(z, q)^T$ denotes the solution vector and $j^{(1)}$ the load vector corresponding to the user-defined goal functional. This linear system is solved using a preconditioned Richardson iteration:

$$\begin{bmatrix} z_{i+1} \\ q_{i+1} \end{bmatrix} := \begin{bmatrix} z_i \\ q_i \end{bmatrix} + \omega C^{-1} \begin{bmatrix} Res_i^z \\ Res_i^q \end{bmatrix}, \tag{3.23}$$

with relaxation parameter ω. The block triangular preconditioning matrix C and the defect are defined by:

$$C := \begin{bmatrix} \tilde{A} & \tilde{B}^T \\ 0 & I \end{bmatrix}, \tag{3.24}$$

$$\begin{bmatrix} Res_i^z \\ Res_i^q \end{bmatrix} := \begin{bmatrix} j^{(1)} \\ 0 \end{bmatrix} - \begin{bmatrix} A & B^T \\ B & 0 \end{bmatrix} \begin{bmatrix} z_i \\ q_i \end{bmatrix}, \tag{3.25}$$

where I denotes the identity matrix. The residual vector $(Res_i^z, Res_i^q)^T$ can be assembled directly without defining the global matrix $\mathcal{A}$. Matrix $\tilde{A}$ has the same entries as A, except for each index n that corresponds to a degree of freedom (DOF) of the velocity on any cell's boundary (see highlighted DOFs in Figure 3.1):

$$\tilde{A}_{n,m} := \begin{cases} 0, & \text{if } n \text{ corresponds to a DOF on cell boundary, } n \neq m \\ 1, & \text{if } n \text{ corresponds to a DOF on cell boundary, } n = m \\ A_{n,m}, & \text{otherwise.} \end{cases}$$

The matrix $\tilde{B}^T$ also has modifications at DOFs corresponding to velocity DOFs at cell boundaries:

$$\tilde{B}^T_{n,m} := \begin{cases} 0, & \text{if } n \text{ corresponds to a DOF on cell boundary} \\ B^T_{n,m}, & \text{otherwise.} \end{cases}$$

Given the discrete dual solution $(z_h, p_h) \in V_h \times Q_h$, the initial value of the iteration (3.23) can be calculated by a nodal interpolation operator $\hat{I}_h : V_h \times Q_h \to \hat{V}_h \times \hat{Q}_h$, which results in a change of basis if $V_h \times Q_h \subset \hat{V}_h \times \hat{Q}_h$. The starting point is defined by

$$(z_0, p_0) := \hat{I}_h(z_h, q_h).$$

Due to the definition of $\tilde{A}$ and $\tilde{B}^T$ only couplings within the same cell are considered. Hence, the correction quantity $(Corr^z_i, Corr^q_i)^T$ can be calculated independently for each cell. The matrix $\tilde{A}$ can be reordered such that it consists of independent blocks, where each block corresponds to one cell. The local problem on cell K for iteration i has the form

$$\omega \begin{bmatrix} \tilde{A}_K & \tilde{B}^T_K \\ 0 & I_K \end{bmatrix}^{-1} \begin{bmatrix} Res^z_{K,i} \\ Res^q_{K,i} \end{bmatrix} = \begin{bmatrix} Cor^z_{K,i} \\ Cor^q_{K,i} \end{bmatrix}, \tag{3.26}$$

which represents a Dirichlet problem for cell K. Only the computation of the residual is a global operation which takes into account the global couplings of the problem. But this is in general not a very expensive calculation in the overall solution procedure and its computation also has large parallelization potential. This block strategy should not be used as a solver, but only for some iterations steps to approximate the cellwise interpolation error needed for the error estimation. The numerical tests described in Chapter 4 suggest that the calculation of approximations based on the block strategy in which only one or two iterations were calculated already yields reliable a posteriori error estimates. A big advantage of this iterative procedure lies in the possibility to control the computational cost and accuracy by determining the number of iterations.

The application of this procedure is denoted by the operator $\mathcal{B} : V_h \times Q_h \to \hat{V}_h \times \hat{Q}_h$, i.e. the approximation of the exact dual solution is given by $(\hat{z}, \hat{q}) := \mathcal{B}(z_h, q_h)$. The primal residual that is evaluated for the error estimation has the following form:

$$\rho(v_h, p_h)(\mathcal{B}(z_h, q_h) - I_h(\mathcal{B}(z_h, q_h))).$$

Approximate solutions $(\hat{u}, \hat{p})$ of the primal problem can in principle be calculated analogously. In this case, the local matrices within the Richardson iteration (3.23) represent linearizations of the nonlinear system and depend on the iteration step, i.e. $\tilde{A}_K \equiv \tilde{A}^i_K$. Still, the calculation of the correction term can be done independently for each cell in parallel.

3.2.1.3 Higher-Order Interpolation

The main drawback of the methods described previously is related to the comparatively high computational cost associated to the higher-order elements, even if only needed locally as proposed in Section 3.2.1.2. In practice, a commonly used approach relies on extrapolation techniques taking advantage of available patch structures in

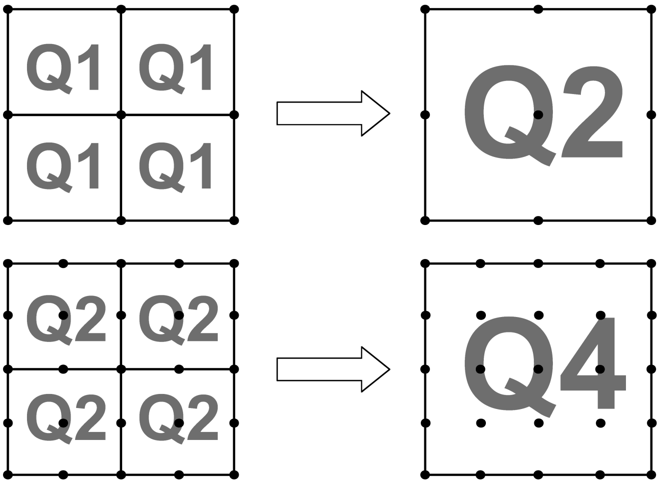

Figure 3.2: Four small cells forming one bigger cell with higher finite element ansatz.

the considered mesh. Theoretically, theses techniques are only valid under strong regularity assumptions both with respect to the mesh and the solution. However these methods are used in a much wider setup, since they rely only on the definition of an adequate interpolation operator, which is usually computationally quite inexpensive.

The considered interpolation scheme can be applied very efficiently to meshes that consist of patches. This means that a mesh consisting of quadrilaterals can be coarsened such that four neighboring cells form one cell in the coarsened mesh (see Figure 3.2). For ease of presentation, Taylor-Hood elements [11] are assumed for the discretization. The idea of higher-order interpolation as described in [2] is to interpret the finite elements in a patch consisting of four cells as one finite element in the common father cell. Therefore, the degrees of freedom of the four cells with finite element ansatz $\mathcal{Q}_n$, $n \in \{1, 2\}$, are used as degrees of freedom in the father cell which has finite element ansatz $\mathcal{Q}_m$, where $m = 2n$ (cf. Section 2.4.2).

In Figure 3.2 for the case of $\mathcal{Q}_1$ and $\mathcal{Q}_2$ cells, a patch of four cells (left) and the corresponding father cell (right) is shown. In meshes that don't have such a patch structure, for each cell a virtual patch cell can be defined and used for the interpolation, which is computationally more expensive, see e.g. to [13] for more details. The higher-order interpolation operator is denoted by

$$\hat{I}_{2h} : V_h \to \hat{V}_h. \tag{3.27}$$

In this special situation it holds $I_h(\hat{I}_{2h}(u_h)) \equiv u_h$ and $I_h(\hat{I}_{2h}(z_h)) \equiv z_h$. Hence, the residuals that are evaluated for the error characterizations have the form

$$\rho(u_h)(\hat{I}_{2h}(z_h) - z_h), \quad \rho^*_{u_h}(z_h)(\hat{I}_{2h}(u_h) - u_h).$$

3.2.1.4 Temporal Structure of Solutions

Using space-time finite element methods, the discrete solutions of time-dependent problems are functions in time, e.g. piecewise linear for the cGP(1) method. The

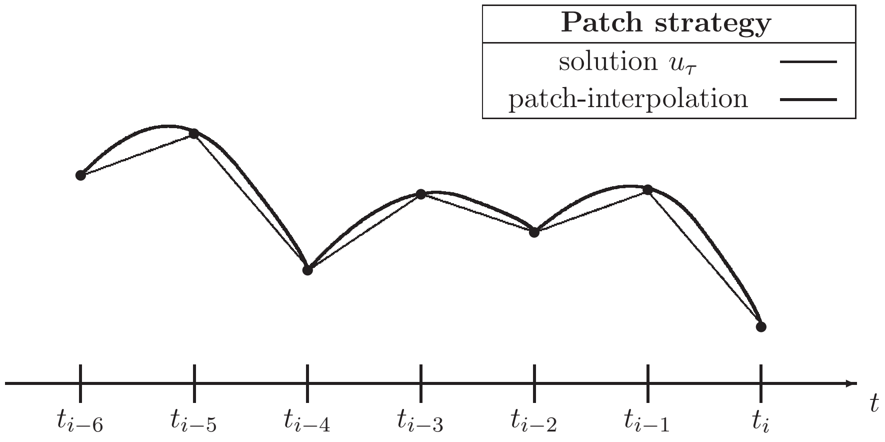

Figure 3.3: For a discrete solution consisting of piecewise linear functions, the nodal values of two neighboring cells lead to a piecewise quadratic function.

time-discrete space is denoted by W_τ and is a subspace of the continuous space W. For the evaluation of the error estimators, approximations of the exact primal and dual solutions must be defined. Analogously to the treatment of the spatial structure of solutions, there are different possibilities to define replacements $\hat{u} \approx u$ and $\hat{z} \approx z$ for these in general unknown exact solutions.

Obviously, finite element solutions based on a higher-order finite element space can be calculated, e.g. piecewise quadratic functions in time (cGP(2) method) instead of piecewise linear functions (cGP(1) method). Alternatively, finite element problems based on a finer temporal resolution, i.e. smaller time step sizes, can be solved. Both strategies lead to higher computational cost for the evaluation of the error estimator (including the solution of the approximate solution) than for the calculation of the discrete primal solution itself. Cheaper approaches by patch-wise interpolation can be defined analogously to the spatial case. Several neighboring time-intervals are treated jointly as one common patch and the solution can be interpreted as one cell in a higher-order finite element space, see Figure 3.3. The arbitrary discrete test functions in the error estimators (3.18)-(3.20) can be defined by nodal interpolation, i.e.

$$I_\tau : W \to L_\tau. \tag{3.28}$$

Note that the range of the interpolation operator is the discrete test space L_τ. Since $L_\tau \neq W_\tau$, the interpolation of the discrete solutions $u_\tau, z_\tau \in W_\tau$ into L_τ can be non-zero, i.e. $u_\tau - I_\tau(u_\tau) \neq 0$ and $z_\tau - I_\tau(z_\tau) \neq 0$. For the cGP(1) method, the temporal structure of a discrete solution and corresponding interpolation into the discrete test space L_τ is indicated in Figure 3.4.

In the special case of Petrov-Galerkin approximations, the discrete solutions $u_\tau, z_\tau \in W_\tau$ can be used as replacements for the exact solutions to evaluate the error characterizations. This leads to the error estimator variant (3.21) described in Remark 10:

$$E(u_\tau) = \rho(u_\tau)(z_\tau - I_\tau(z_\tau)),$$

in which only the primal residual needs to be evaluated.

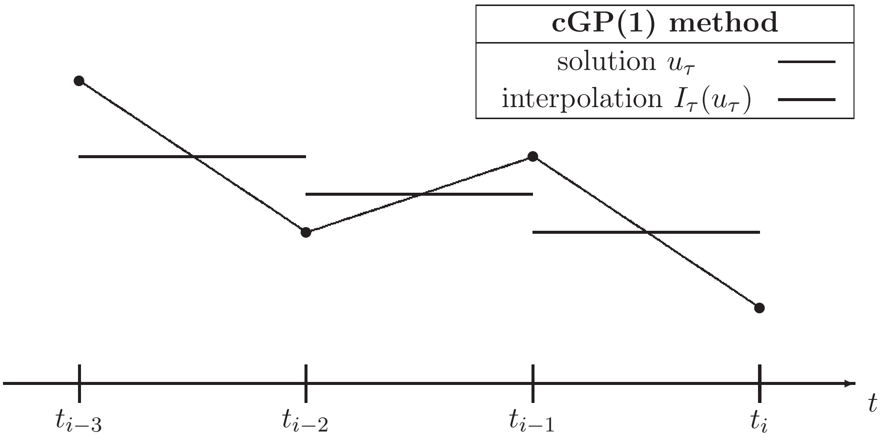

Figure 3.4: The cGP(1) method leads to piecewise linear solutions in time. The weights used for error estimation are the difference between the solution and the interpolation into piecewise constant functions.

The discretization of the Navier-Stokes equation described in Section 2.4.1 is based on piecewise constant pressure functions in time. In this case, a higher-order interpolation operator can be introduced to calculate a piecewise linear pressure representation at very low cost. Let $W^{(\mathrm{p})}$ denote the solution space corresponding to the pressure function and $W_\tau^{(\mathrm{p})}$ the discrete subspace which is the solution space of the Petrov-Galerkin method. A discrete pressure $p_\tau \in W_\tau^{(\mathrm{p})}$ can be transformed into a piecewise linear representation in terms of the operator $\hat{I}_\tau : W_\tau^{(\mathrm{p})} \to W^{(\mathrm{p})}$:

$$\hat{I}_\tau(p_\tau)(t) := p_\tau(t_i) + \frac{p_\tau(t_i) - p_\tau(t_{i-1})}{t_i - t_{i-1}}(t - t_{i-1}), \quad t \in [t_{i-1}, t_i], \tag{3.29}$$

for any $i = 1, \dots N$, see Figure 3.5. This interpolation operator will be used for the numerical experiments described in Chapter 5.

3.2.1.5 Numerical Quadrature

In the context of goal-oriented adaptive methods and space-time discretizations as presented in Section 2.4, integrals in space and time play a central role. Their calculation in terms of numerical quadrature can be very costly such that these can make up a substantial part of the overall computational effort. Especially if the integrands are not smooth, accurate quadrature requires intensive calculations. The integrals over the entire space-time domain can be evaluated by summing up the integrals over each cell.

Gaussian quadrature rules are widely used because polynomials up to degree $2n - 1$ can be integrated exactly while evaluating only n quadrature points. The one-dimensional quadrature rule for interval $[0, 1]$ is defined as

$$\int_{x=0}^{1} f(x)\,dx \approx Q_n(f) := \sum_{i=1}^{n} w_i \cdot f(x_i), \tag{3.30}$$

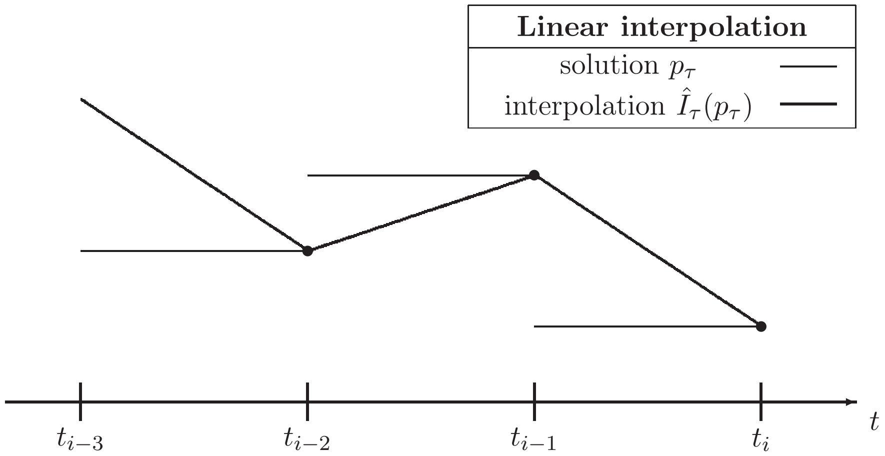

Figure 3.5: Piecewise linear interpolation of a piecewise constant function.

with weights w_j and nodes x_j, $j \in \{1, n\}$. By the method of separation of variables, product formulas can be derived [45] to evaluate the integrals over quadrilateral cells within the spatial mesh. For a cell $[0,1]^2$ the corresponding quadrature rule has the form

$$\int_{x_1=0}^{1} \int_{x_2=0}^{1} f(x_1, x_2)\, dx \approx Q_{n,m}(f) := \sum_{i=1}^{n} \sum_{j=1}^{m} w_i w_j \cdot f(x_i, x_j), \tag{3.31}$$

which is exact as long as f is a polynomial of order $2n-1$ in the first and of order $2m-1$ in the second argument at most. For the evaluation of the residuals needed for error estimation, the polynomial degree of the integrand can be large as the following two examples show. Consider a spatial discretization of the Navier-Stokes equations with Taylor-Hood elements, i.e. piecewise biquadratic functions for the velocity and bilinear functions for the pressure variable. The error estimator (3.18) contains the residual expression $\rho(\upsilon_h)(\hat{z} - z_h - \varphi_h)$, where $\hat{z}$ denotes an approximation of the exact dual solution. Assuming the higher-order interpolation strategy described in Section 3.2.1.3, the approximation $\hat{z}$ is a polynomial of fourth order in each space direction. In this case, the integration of the nonlinear term of the Navier-Stokes equations, $((\upsilon_h \cdot \nabla)\upsilon_h, \hat{z})_{L^2(\Omega)}$, on each cell $K \in \mathcal{T}_h$ requires the quadrature of a polynomial of order eight in each space direction. For an exact evaluation with a Gaussian quadrature rule (3.31), $m = n = 5$ is necessary, hence 25 quadrature points per cell in the spatial mesh are needed in 2D. Another delicate aspect with respect to quadrature is related to the goal functional J. If J is defined as the integral of a non-smooth function j, as later used in Section 5.2, for example, the evaluation of $J(\upsilon_h) = (j, \upsilon_h)$ and the right-hand side of the dual problem $\nabla J(\upsilon_h)\varphi = (j, \varphi)$ can also necessitate costly quadrature rules.

For time-dependent problems, further integrations with respect to time must be evaluated. If the basis of the test and trial functions are not well-suited to the quadrature rule, the computational cost can increase considerably. In [39], Schieweck proposes the usage of a $k+1$ Gauß-Lobatto formula (exact for polynomials up to order $2k-1$) for the discretization with the cGP(k) method. For linear problems, the integrands are piecewise polynomials of order $2k-1$, because the test functions are of order $k-1$ while the trial functions are of order k, hence the quadrature is exact. In this case, the adjustment of quadrature rule and basis functions can lead to a significant decoupling and reduction of the related computational cost for the calculation of the integrals. For nonlinear problems on the other hand, such a level of decoupling cannot be achieved. For the evaluation of the error estimates presented before, the test functions are replaced by higher-order solutions. The nonlinear term of the Navier-Stokes equations represents the part of the integrand with the highest polynomial degree. Already for the the case of $k=1$, assuming the usage of the discrete dual solution z_τ as approximation for the exact solution (see Remark 10), leads to an integral of the form $\int_{i_{i-1}}^{t_i}((\upsilon_\tau \cdot \nabla)\upsilon_\tau, z_\tau)_{L^2(\Omega)}dt$ that must be evaluated. Here, the integrand is a polynomial of order three, as each of the functions υ_τ, z_τ is piecewise linear in time. Such integrals can be evaluated using Simpson's rule (exact for polynomials of third order), for example:

$$\int_a^b \Psi(t)\,dt \approx Q_s(\Psi) := \frac{b-a}{6}\left(\Psi(a) + 4\Psi\left(\frac{a+b}{2}\right) + \Psi(b)\right). \tag{3.32}$$

3.2.2 Derivation of Error Indicators

Based on the a posteriori error estimators given in Section 3.2, the accuracy of approximate solutions with respect to the investigator's quantity of interest can be determined and used to define stopping criteria for adaptive methods. In an additional localization step, the error contributions from each cell in the space-time mesh can be quantified leading to so-called *error indicators.* Using this information, adaptive methods can be based on refining or coarsening the cells which have very large or very small error indicators, respectively.

To define cellwise error indicators, the residuals ρ and ρ^* of the primal and dual problems are given in terms of integrals over space and time and are formulated as sums over cell and edge residuals. The problems are assumed to have smooth data and the mesh $\mathcal{T}_h$ coincides with the domain Ω. Due to the polynomial structure of the discrete solutions when restricted to each cell, the residual can be rewritten in terms of cell and edge integrals. The procedure is demonstrated for the error characterization (3.19), where the primal residual $\rho(u_h)(\Phi)$ must be evaluated. The test function is defined by $\Phi := \hat{z} - I_h(\hat{z})$ and u_h denotes the Petrov-Galerkin approximations of the primal problem and $\hat{z}$ represents a higher-order approximation of the dual solution. The error characterization is written as a sum over the cell contributions:

$$|E_P(u_h)| \;\; := \;\; \Big|\sum_{K\in\mathcal{T}_h} \rho(u_h)(\Phi)_{|K}\Big|.$$

By integration by parts, the integral over a cell $K \in T_h$ can be written as an integral over the cell and a further integral over the cell-boundary, i.e.

$$(\rho(u_h)(\Phi))_{|K} = (R,\Phi)_K + (\bar{r},\Phi)_{\partial K},$$

where $R(u_h)$ denotes the *cell* or *interior residual* corresponding to the residual part defined on the cell and $\bar{r}(u_h)$ the residual part corresponding to the cell's edges. The latter can be further redistributed over neighboring cells leading to jumps over inter-cell edges and integrals along the domain's boundary $\partial\Omega$. The quantity $r(u_h)$ is denoted by *boundary* or *edge residual.* Hence

$$(\rho(u_h)(\Phi))_{|K} \quad = \quad (R(u_h), \Phi)_K + \sum_{\gamma \in \Gamma(K)} (r(u_h), \Phi)_\gamma,$$

where $\Gamma(K)$ denotes the set of edges of cell K. The error indicator for cell K is defined as the absolute value of the cell residual and the summed edge residuals corresponding to that cell. For the error estimator variant E_P, the upper bound η_P is given in terms of error indicators $\eta_{P,K} \geq 0$ for any cell K of the mesh:

$$|E_P(u_h)| \leq \eta_P := \sum_{K \in \mathcal{T}_h} \eta_{P,K}, \quad \eta_{P,K} := \Big|(R(u_h), \Phi)_K + \sum_{\gamma \in \Gamma(K)} (r(u_h), \Phi)_\gamma\Big|.$$

In terms of the error indicators defined by

$$\begin{aligned} \eta_{D,K} \quad &:= \quad \Big|(R^*(z_h), \Psi)_K + \sum_{\gamma \in \Gamma(K)} (r^*(z_h), \Psi)_\gamma\Big|, \\ \eta_{PD,K} \quad &:= \quad \Big|(R(u_h), \Phi)_K + (R^*(z_h), \Psi)_K + \sum_{\gamma \in \Gamma(K)} (r(u_h), \Phi)_\gamma + (r^*(z_h), \Psi)_\gamma\Big|, \end{aligned}$$

upper bounds η_D and η_{PD} for the error estimates E_D and E_{PD} can be defined. Here, R^* and r^* denote the cell and edge residuals corresponding to the dual problem and the test function is defined by $\Psi := \hat{u} - u_h - I_h(\hat{u} - u_h)$, where u_h denotes the Petrov-Galerkin approximation and $\hat{u}$ a higher-order approximation of the primal problem. The test function Φ used for the primal residual is defined as $\Phi := \hat{z} + z_h - I_h(\hat{z} + z_h)$ to calculate error indicators corresponding to $\eta_{PD,K}$, cf. equation (3.18). The cell and edge residuals for the Navier-Stokes equation will be derived in Section 3.3.

The presented approach to define error indicators is discussed in [5] in the context of Galerkin approximations. Furthermore, for Poisson's problem, the indicators $\eta_{P,K}$ are further estimated by

$$\eta_P \leq \bar{\eta}_P := \sum_{K \in \tau_h} \bar{\eta}_{P,K}, \quad \bar{\eta}_{P,K} := \rho_K \omega_K$$

in terms of error indicators $\bar{\eta}_{P,K}$ defined as product of the cell residuals ρ_K and the weights ω_K, given by

$$\rho_K := \left(\|R(u_h)\|_K^2 + h_K^{-1} \|r(u_h)\|_{\partial K}^2\right)^{1/2}, \quad \omega_K := \left(\|\Phi\|_K^2 + h_K \|\Phi\|_{\partial K}^2\right)^{1/2}.$$

Here, h_K denotes the cell diameter as defined in Section 2.4.2. For this choice of error indicators, the authors of [5] show that the weights satisfy $\omega_K \approx C h_K^2 \left\|\nabla^2 z\right\|_K$.

Alternative localization approaches have been proposed in the literature. For example, an approach based on nodal contributions is described by Braack and Ern

[7]. The error contribution for single nodes is defined using nodal interpolation. To control the mesh adaptation process, it is suitable to characterize the error contribution of cells. To this end, the nodal error indicators must be redistributed over the neighboring cells in a further step.

For a space-time finite element discretization, indicators that distinguish between the error contribution related to the discretization in space and time are needed. To this end, Schmich and Vexler [40] proposed to split the error in J into two parts:

$$J(u) - J(u_{h\tau}) = (J(u) - J(u_\tau)) + (J(u_\tau) - J(u_{k\tau})),$$

where $u \in W$, $u_\tau \in W_\tau$ and $u_{h\tau} \in W_{h\tau}$ are solutions of the continuous, the time-discrete and the fully discrete problem. In the following, conforming discretizations in space and time are assumed. Consider the three problems in terms of the Lagrange functional $\mathcal{L}$:

$$\begin{aligned}
u, z \in W: &\quad \mathcal{L}'(u,z)(\varphi,\psi) &=& \; 0 \quad \forall \varphi, \psi \in L, && (3.33)\\
u_\tau, z_\tau \in W_\tau: &\quad \mathcal{L}'(u_\tau,z_\tau)(\varphi_\tau,\psi_\tau) &=& \; 0 \quad \forall \varphi_\tau, \psi_\tau \in L_\tau, && (3.34)\\
u_{h\tau}, z_{h\tau} \in W_{h\tau}: &\quad \mathcal{L}'(u_{h\tau},z_{h\tau})(\varphi_{h\tau},\psi_{h\tau}) &=& \; 0 \quad \forall \varphi_{h\tau}, \psi_{h\tau} \in L_{h\tau}, && (3.35)
\end{aligned}$$

where $W \subseteq L$ denotes the continuous, $W_\tau \subseteq L_\tau$ denotes the time-discrete and $W_{h\tau} \subseteq L_{h\tau}$ denotes the fully discrete spaces (the latter are used for the space-time finite element method). For clarity, the characterization of the primal and dual solutions in terms of the Lagrange functional is used instead of the primal and dual residuals. The conformity of the semi-discrete and fully discrete spaces holds, since $W_{h\tau} \subseteq W_\tau \subseteq W$ and $L_{h\tau} \subseteq L_\tau \subseteq L$. Applying Corollary 6 to the problems (3.33)-(3.34) and (3.34)-(3.35), it holds that

$$\begin{aligned}
\mathcal{L}(u,z) - \mathcal{L}(u_\tau,z_\tau) &= \frac{1}{2}\mathcal{L}'(u_\tau,z_\tau)(u - u_\tau - \varphi_\tau, z - z_\tau - \psi_\tau) + \mathcal{R}_\tau,\\
\mathcal{L}(u_\tau,z_\tau) - \mathcal{L}(u_{\tau h},z_{\tau h}) &= \frac{1}{2}\mathcal{L}'(u_{h\tau},z_{h\tau})(u_\tau - u_{h\tau} - \varphi_{h\tau}, z_\tau - z_{h\tau} - \psi_{h\tau}) + \mathcal{R}_h.
\end{aligned}$$

It must be noted, that for the continuous solution it holds $\mathcal{L}(u,z) = J(u) - \rho(u)(z) = J(u)$, and for the semi-discrete and fully discrete solutions it holds $\mathcal{L}(u_\tau,z_\tau) = J(u_\tau) - \rho(u_\tau)(z_\tau)$ and $\mathcal{L}(u_{\tau h},z_{\tau h}) = J(u_{\tau h}) - \rho(u_{\tau h})(z_{\tau h})$, respectively. Hence,

$$\begin{aligned}
J(u) - J(u_\tau) &= \mathcal{L}(u,z) - \mathcal{L}(u_\tau,z_\tau) + \rho(u_\tau)(z_\tau),\\
J(u_\tau) - J(u_{h\tau}) &= \mathcal{L}(u_\tau,z_\tau) - \rho(u_\tau)(z_\tau) - \mathcal{L}(u_{\tau h},z_{\tau h}) + \rho(u_{\tau h})(z_{\tau h}).
\end{aligned}$$

Therefore, the error in J can be characterized in terms of the primal and dual residuals. For the error corresponding to the time discretization holds

$$\begin{aligned}
J(u) - J(u_\tau) &= \frac{1}{2}\big(\rho(u_\tau)(z - z_\tau - \varphi_\tau) + \rho^*_{u_\tau}(z_\tau)(u - u_\tau - \psi_\tau)\big)\\
&\quad + \rho(u_\tau)(z_\tau) + \mathcal{R}_\tau\\
&= \frac{1}{2}\big(\rho(u_\tau)(z + z_\tau - \varphi_\tau) + \rho^*_{u_\tau}(z_\tau)(u - u_\tau - \psi_\tau)\big) + \mathcal{R}_\tau, \qquad (3.36)
\end{aligned}$$

for arbitrary and $\varphi_\tau, \psi_\tau \in L_\tau$ with remainder term $\mathcal{R}_\tau$ and for the error corresponding to the space discretization holds

$$\begin{aligned} J(u_\tau) - J(u_{h\tau}) &= \frac{1}{2}\left(\rho(u_{h\tau})(z_\tau - z_{h\tau} - \varphi_{h\tau}) + \rho^*_{u_{\tau h}}(z_{h\tau})(u_\tau - u_{h\tau} - \psi_{h\tau})\right) \\ &\quad -\rho(u_\tau)(z_\tau) + \rho(u_{h\tau})(z_{h\tau}) + \mathcal{R}_h \\ &= \frac{1}{2}\left(\rho(u_{h\tau})(z_\tau + z_{h\tau} - \varphi_{h\tau}) + \rho^*_{u_{\tau h}}(z_{h\tau})(u_\tau - u_{h\tau} - \psi_{h\tau})\right) \\ &\quad -\rho(u_\tau)(z_\tau) + \mathcal{R}_h, \end{aligned} \tag{3.37}$$

for arbitrary $\varphi_{h\tau}, \psi_{h\tau} \in L_{h\tau}$ with remainder term $\mathcal{R}_h$. To derive computable estimators, modifications of these characterizations have to be done, as already described in Section 3.2. The remainder terms are neglected and the unknown quantities used as test functions of the residuals are replaced by approximations $\hat{u} \approx u$, $\hat{z} \approx z$ and $\hat{u}_\tau \approx u_\tau$, $\hat{z}_\tau \approx z_\tau$. As before, the functions $\varphi_\tau, \psi_\tau \in L_\tau$ and $\varphi_{h\tau}, \psi_{h\tau} \in L_{h\tau}$ can be chosen arbitrarily without changing the values of the error characterizations. Defining these by

$$\begin{aligned} \psi_\tau &:= I_\tau(\hat{u} - \hat{u}_\tau), \quad & \varphi_\tau &:= I_\tau(\hat{z} + \hat{z}_\tau), \\ \psi_{h\tau} &:= I_{h\tau}(\hat{u}_\tau - u_{h\tau}), \quad & \varphi_{h\tau} &:= I_{h\tau}(\hat{z}_\tau + z_{h\tau}), \end{aligned}$$

with interpolation operators $I_\tau : L \to L_\tau$ and $I_{h\tau} : L \to L_{h\tau}$ leads to small weights of the residuals. But the semi-discrete functions $(u_\tau, z_\tau) \in W_\tau \times W_\tau$ are not known. Schmich and Vexler propose to replace the residual functionals $\rho(u_\tau)$ and $\rho^*_{u_\tau}(z_\tau)$ by the discrete functionals $\rho(u_{\tau h})$ and $\rho^*_{u_{\tau h}}(z_{\tau h})$. Furthermore, the semi-discrete residual $\rho(u_\tau)(z_\tau)$ in equation (3.37) is neglected. The resulting computable error characterizations $E^{(time)}(u_{h\tau}) \approx J(u) - J(u_\tau)$ and $E^{(space)}(u_{h\tau}) \approx J(u_\tau) - J(u_{h\tau})$ related to the time and space discretizations are given by

$$E^{(time)}(u_{h\tau}) := \frac{1}{2}\left(\rho(u_{h\tau})(\hat{z} + \hat{z}_\tau - \psi_\tau) + \rho^*_{u_{\tau h}}(z_{h\tau})(\hat{u} - \hat{u}_\tau - \varphi_\tau)\right), \tag{3.38}$$

$$E^{(space)}(u_{h\tau}) := \frac{1}{2}\left(\rho(u_{h\tau})(\hat{z}_\tau + z_{h\tau} - \psi_{h\tau}) + \rho^*_{u_{\tau h}}(z_{h\tau})(\hat{u}_\tau - u_{h\tau} - \varphi_{h\tau})\right). \tag{3.39}$$

Integration by parts, redistribution of edge residuals in terms of jump-terms and cellwise application of the triangle inequality (as described in Section 3.2.2) yields error indicators related to the time and space structure, respectively:

$$\begin{aligned} |J(u) - J(u_{h\tau})| &\le |J(u) - J(u_\tau)| + |J(u_\tau) - J(u_{h\tau})| \\ &\le \sum_{i=1}^{N_{\text{time}}} \sum_{K \in \mathcal{T}_h(i)} \eta^{(time)}_{iK} + \eta^{(space)}_{iK}. \end{aligned} \tag{3.40}$$

Here, N_{time} denotes the number of time-steps used for the time discretization. The spatial triangulation $\mathcal{T}_h(i)$ may vary on each interval (t_{i-1}, t_i) for $i \in \{1, \dots, N_{\text{time}}\}$. The validity of the temporal and spatial error indicators can be exemplified numerically. Figure 3.6 shows the summed error indicators

$$\eta^{(time)}(u_{h\tau}) := \sum_{i=1}^{N_{time}} \sum_{K \in \mathcal{T}_h(i)} \eta^{(time)}_{iK}, \quad \eta^{(space)}(u_{h\tau}) := \sum_{i=1}^{N_{time}} \sum_{K \in \mathcal{T}_h(i)} \eta^{(space)}_{iK},$$

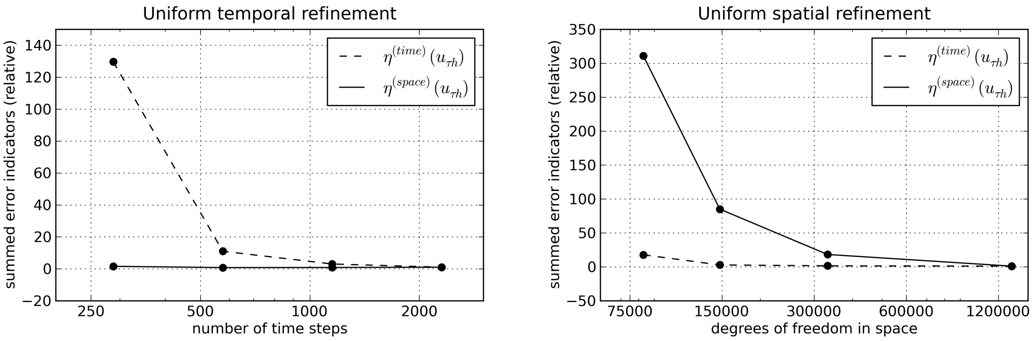

Figure 3.6: Summed error indicators corresponding to temporal and spatial discretization for the case of uniform refinement of the temporal mesh (left) and uniform refinement of the spatial mesh (right).

for the instationary scenario presented in Chapter 5 corresponding to uniformly refined meshes and time partitions. The left panel shows simulations based on a spatial mesh with 36.864 degrees of freedom. The temporal error indicators decrease while the spatial indication remains at a constant level. In contrast, the panel on the right shows simulations based on a constant time step size of 300 s which corresponds to 1,152 time steps and consecutive uniformly refined meshes. In this case, the error indicators related to the time discretization remain at the same order of magnitude, while the indicators for the space discretization are clearly decreasing.

Based on the error indicators $\eta_{iK}^{(time)}$ and $\eta_{iK}^{(space)}$ given in (3.40), it is convenient to define further reduced indicators that are suitable for the specific mesh adaptation to be done. For the time-dependent numerical simulations carried out later, a single spatial mesh was used for the complete time interval, i.e $\mathcal{T}_h(i) \equiv \mathcal{T}_h$ for all $i \in \{1, \dots, N_{\text{time}}\}$. To this end, the definition of the following spatial error indicator is adequate:

$$\eta_K^{(space)} := \max_{i=1}^{N_{\text{time}}} \left(\eta_{i,K}^{(space)} / (t_i - t_{i-1}) \right) \quad \forall K \in \mathcal{T}_h. \tag{3.41}$$

A common restriction of time-discretizations is to use identical time-steps over the spatial domain. Appropriate temporal error indicators for the determination of optimal time-steps can then be defined by

$$\eta_i^{(time)} := \max_{K \in \mathcal{T}_h(i)} \eta_{iK}^{(time)} \quad \forall i \in \{1, \dots, N_{\text{time}}\}. \tag{3.42}$$

3.2.3 Post-processed Quantity of Interest

In the context of goal-oriented methods, the main interest is to determine a user-defined quantity described in terms of the goal functional J. For an approximate solution u_h, the error $J(u) - J(u_h)$ can be estimated in terms of a posteriori error estimators, denoted by $E(u_h)$ in this section, as described before. If the estimation $E(u_h)$ is a good approximation to the true error $J(u) - J(u_h)$, the post-processed quantity of interest

$$\tilde{J}(u_h) := J(u_h) + E(u_h), \tag{3.43}$$

should be a good approximation to the exact value $J(u)$. Analog representations can be defined for the simplified error representations:

$$\begin{aligned} \tilde{J}_P(u_h) &:= J(u_h) + E_P(u_h), \\ \tilde{J}_D(u_h) &:= J(u_h) + E_D(u_h). \end{aligned} \tag{3.44}$$

These post-processed approximations have been calculated and compared to the canonical approximation $J(u_h)$ in the numerical simulations in Chapters 4 and 5.

3.3 Error Estimation for the Navier-Stokes Equations

In this section goal-oriented error estimators and corresponding local indicators for the Navier-Stokes equations are derived. To this end, the variational problem in terms of integrals in space and time that was introduced in Section 2.2 is considered. For $f \in L^2(0,T;V_{div})$ and $\upsilon_0 \in H_{div}$, a weak solution $(\upsilon, p) \in X \times M$ of the Navier-Stokes equations satisfies

$$\rho(\upsilon,p)(\varphi,\psi) = 0 \quad \forall(\varphi,\psi) \in Y \times M. \tag{3.45}$$

Here, the residual is defined as

$$\begin{aligned} \rho(\upsilon,p)(\varphi,\psi) := \int_0^T \Big(&\langle \partial_t \upsilon, \varphi \rangle_{V^*,V} + ((\upsilon \cdot \nabla)\upsilon - f, \varphi) + \nu(\nabla \upsilon, \nabla \varphi) - (p, \nabla \cdot \varphi) \\ &+ (\nabla \cdot \upsilon, \psi) \Big)\, dt + (\upsilon_{|t=0} - \upsilon_0, \varphi_{|t=0}). \end{aligned}$$

The spaces are defined as

$$\begin{aligned} X &:= W(0,T) \cap L^4(0,T;V) \cap L^\infty(0,T;H), \\ Y &:= L^2(0,T;V) \cap L^\infty(0,T;H), \\ M &:= L^2(0,T;Q). \end{aligned}$$

Let the goal functional $J : Y \to \mathbb{R}$ considered in the following be defined by

$$J(\upsilon) := \int_0^T \left\langle j^{(1)}, \upsilon \right\rangle_{V^*,V} dt + (j^{(2)}, \upsilon_{|t=T}),$$

where $j^{(1)} \in Y^*$ and $j^{(2)} \in Q$. A Lagrange functional $\mathcal{L} : (X \times M) \times (X \times M) \to \mathbb{R}$ is defined by

$$\mathcal{L}((\upsilon,p),(z,q)) := J(\upsilon,p) + \rho(\upsilon,p)(z,q). \tag{3.46}$$

A stationary point $((\upsilon,p),(z,q)) \in (X \times M) \times (X \times M)$ of the Lagrange functional can be characterized by vanishing derivatives:

$$\mathcal{L}_{(z,q)}((\upsilon,p),(z,q))(\varphi,\psi) = 0 \quad \forall(\varphi,\psi) \in X \times M, \tag{3.47}$$

$$\mathcal{L}_{(\upsilon,p)}((\upsilon,p),(z,q))(\varphi,\psi) = 0 \quad \forall(\varphi,\psi) \in X \times M. \tag{3.48}$$

Condition (3.47) is equivalent to the variational problem (3.45) and called the *primal problem* in this context. For the equivalence, the replacement of the test space X by

Y must be justified. Due to the linearity of the Lagrange functional in the third and fourth arguments, it holds $\mathcal{L}_z((v,p),(z,q))\varphi = \rho(v,p)(\varphi,q)$ and $\mathcal{L}_q((v,p),(z,q))\psi = \rho(v,p)(z,\psi)$ for all $(\varphi,\psi) \in X \times M$. Furthermore, the residual $\rho(v,p)(\cdot,\psi) : X \to \mathbb{R}$ is continuous in $L^2(0,T;V)$, where the continuity of the linear parts can be shown as described in Section 3.1. The nonlinear term has the form $\int_0^T n(v,v,\varphi)\,dt$. For the trilinear form $n : V \times V \times V \to \mathbb{R}$ defined by

$$n(a,b,c) := ((a \cdot \nabla)b, c)_{L^2(\Omega)},$$

it holds

$$|n(a,b,c)| \leq \sqrt{2}\,\|a\|_H^{1/2}\,\|a\|_V^{1/2}\,\|b\|_V\,\|c\|_H^{1/2}\,\|c\|_V^{1/2} \tag{3.49}$$

for all $a,b,c \in V$, cf. [47]. For every $a,b \in V$, a functional $N(a,b) \in V^*$ exists such that

$$\langle N(a,b),\varphi\rangle_{V^*,V} = n(a,b,\varphi) \quad \forall \varphi \in V.$$

Let $v \in X$. Then for almost every $t \in [0,T]$ $N(v(t),v(t)) \in V^*$ and furthermore,

$$\begin{aligned}
&\langle N(v,v),\varphi\rangle_{L^2(0,T;V)^*,L^2(0,T;V)} \\
= &\int_0^T \langle N(v(t),v(t)),\varphi(t)\rangle_{V^*,V}\,dt \\
= &\int_0^T n(v(t),v(t),\varphi(t))\,dt \\
\leq &\int_0^T \sqrt{2}\,\|v(t)\|_H^{1/2}\,\|v(t)\|_V^{3/2}\,\|\varphi(t)\|_H^{1/2}\,\|\varphi(t)\|_V^{1/2}\,dt \\
\leq &\int_0^T \sqrt{2}\,\|v(t)\|_H^{1/2}\,\|v(t)\|_V^{3/2}\,\|\varphi(t)\|_V\,dt.
\end{aligned}$$

By definition of the space X, it holds $X \subseteq L^\infty(0,T;H)$ and for any $v \in X$ there exists $M > 0$ such that $\|v(t)\|_H \leq M$ for almost all $t \in [0,T]$. Hence,

$$\begin{aligned}
&\langle N(v,v),\varphi\rangle_{L^2(0,T;V)^*,L^2(0,T;V)} \\
\leq &\sqrt{2MT}\int_0^T \|v(t)\|_V^{3/2}\,\|\varphi(t)\|_V\,dt \\
\leq &\sqrt{2MT}\left(\int_0^T \|v(t)\|_V^3\,dt\right)^{1/2}\left(\int_0^T \|\varphi(t)\|_V^2\,dt\right)^{1/2} \\
= &\sqrt{2MT}\,\|v\|_{L^3(0,T;V)}^{3/2}\,\|\varphi\|_{L^2(0,T;V)}\,.
\end{aligned}$$

Since $v \in X$, and therefore $v \in L^4(0,T;V)$, it follows that $N(v,v) \in L^2(0,T;V)^*$. Since the space $W(0,T) \cap L^4(0,T;V)$ is a dense subspace of $L^2(0,T;V)$ (see Lemma 1), problem (3.47) can be formulated in the larger space Y, which leads to (3.45).

The second stationary condition (3.48) leads to the *dual problem.* Let $(v,z) \in X \times X$. Due to the linearity of the Lagrange functional in the second argument (pressure component), it holds that $\mathcal{L}_p((v,p),(z,q))\psi = \mathcal{L}((v,\psi),(z,q))$ for all $\psi \in M$. The v-derivative of the nonlinear term $\int_0^T n(v,v,z)\,dt$ in direction φ is given by

$\int_0^T n(v,\varphi,z)+n(\varphi,v,z)\,dt$. As n is bounded, see (3.49), a functional $N^*: V\times V\to V^*$ can be defined such that for arbitrary $a,b,c\in V$ it holds that

$$\langle N^*(a,b),c\rangle_{V^*,V} = n(a,c,b)+n(c,a,b).$$

Hence, for almost every $t\in[0,T]$ it holds that $N^*(v(t),z(t))\in V^*$. Furthermore,

$$\begin{aligned}
&\langle N^*(v,z),\varphi\rangle_{L^2(0,T;V)^*,L^2(0,T;V)}\\
={}& \int_0^T \langle N^*(v(t),z(t)),\varphi(t)\rangle_{V^*,V}\,dt\\
={}& \int_0^T \Big(n(v(t),\varphi(t),z(t))+n(\varphi(t),v(t),z(t))\Big)\,dt\\
\le{}& \sqrt{2}\int_0^T \Big(\|v(t)\|_H^{1/2}\|v(t)\|_V^{1/2}\|\varphi(t)\|_V\|z(t)\|_H^{1/2}\|z(t)\|_V^{1/2}\\
&\qquad+\|\varphi(t)\|_H^{1/2}\|\varphi(t)\|_V^{1/2}\|v(t)\|_V\|z(t)\|_H^{1/2}\|z(t)\|_V^{1/2}\Big)\,dt\\
\le{}& \sqrt{2}\int_0^T 2\|v(t)\|_V\|\varphi(t)\|_V\|z(t)\|_V\,dt.
\end{aligned}$$

Since $v,z\in X$, it holds

$$\begin{aligned}
&\langle N^*(v,z),\varphi\rangle_{L^2(0,T;V)^*,L^2(0,T;V)}\\
\le{}& \sqrt{8}\int_0^T \|v(t)\|_V\|z(t)\|_V\|\varphi(t)\|_V\,dt\\
\le{}& \sqrt{8}\left(\int_0^T \|v(t)\|_V^2\|z(t)\|_V^2\,dt\right)^{1/2}\left(\int_0^T \|\varphi(t)\|_V^2\,dt\right)^{1/2}\\
\le{}& \sqrt{8}\left(\int_0^T \|v(t)\|_V^4\,dt\right)^{1/4}\left(\int_0^T \|z(t)\|_V^4\,dt\right)^{1/4}\left(\int_0^T \|\varphi(t)\|_V^2\,dt\right)^{1/2}\\
={}& \sqrt{8}\|v\|_{L^4(0,T;V)}\|z\|_{L^4(0,T;V)}\|\varphi\|_{L^2(0,T;V)}.
\end{aligned}$$

Integration by parts yields

$$\int_0^T \langle\partial_t\varphi,z\rangle_{V^*,V}\,dt = -\int_0^T\langle\partial_t z,\varphi\rangle_{V^*,V}\,dt+(\varphi_{|t=T},z_{|t=T})-(\varphi_{|t=0},z_{|t=0}).$$

The remaining terms in the definition of the dual residual are linear and therefore it is continuous in $L^2(0,T;V)$. Hence, problem (3.48) can be formulated in the larger space Y leading to the following dual problem: Find $(z,q)\in X\times M$ such that

$$\rho_v^*(z,q)(\varphi,\psi)=0\quad\forall(\varphi,\psi)\in Y\times M, \tag{3.50}$$

where the dual residual is defined by

$$\begin{aligned}
\rho_v^*(z,q)(\varphi,\psi) := \int_0^T\Big(&\Big\langle -\partial_t z+j^{(1)},\varphi\Big\rangle_{V^*,V}+((v\cdot\nabla)\varphi+(\varphi\cdot\nabla)v,z)+\nu(\nabla z,\nabla\varphi)\\
&-(\psi,\nabla\cdot z)+(\nabla\cdot\varphi,q)\Big)\,dt+(\varphi_{|t=T},z_{|t=T}+j^{(2)}).
\end{aligned}$$

Finally, the stationary conditions (3.47)-(3.48) for $(\upsilon, p, z, q) \in X \times M \times X \times M$ can be stated in terms of the primal and dual residuals:

$$\rho(\upsilon, p)(\varphi_1, \psi_2) + \rho^*_\upsilon(z, q)(\varphi_2, \psi_2) = 0, \tag{3.51}$$

for any $(\varphi_1, \psi_1, \varphi_2, \psi_2) \in Y \times M \times Y \times M$. For a no-slip boundary, the strong form of the dual problem corresponding to the variational problem (3.50) has the form

$$\begin{aligned} -\partial_t z + (\nabla \upsilon)^T z - (\nabla \cdot \upsilon) z - (\upsilon \cdot \nabla) z - \nu \Delta z - \nabla q &= -j^{(1)} \quad \text{in } I \times \Omega, && (3.52)\\ \nabla \cdot z &= 0 \quad \text{in } I \times \Omega, && (3.53)\\ z_{|t=T} &= -j^{(2)} \quad \text{in } \Omega, && (3.54)\\ z &= 0 \quad \text{in } I \times \partial\Omega. && (3.55) \end{aligned}$$

Existence, uniqueness and regularity statements for problem (3.52)-(3.55) can be found in [29], for example.

Based on the primal problem (3.45) and the dual problem (3.50), Petrov-Galerkin approximations can be defined in finite dimensional subspaces in terms of space-time finite element methods as described in Section 2.4, i.e. $V_h \subseteq V$, $Q_h \subseteq Q$, $X_{\tau h} \subseteq X$, $Y_{\tau h} \subseteq Y$, and $M_{\tau h} \subseteq M$. The error of the approximation of the primal problem with respect to the goal functional can be characterized using Corollary 6:

$$\begin{aligned} J(\upsilon) - J(\upsilon_{\tau h}) &= \frac{1}{2}\rho(\upsilon_{\tau h}, p_{\tau h})(z + z_{\tau h} - \varphi_1, q - q_{\tau h} - \psi_1)\\ &\quad + \frac{1}{2}\rho^*_{\upsilon_{\tau h}}(z_{\tau h}, q_{\tau h})(\upsilon - \upsilon_{\tau h} - \varphi_2, p - p_{\tau h} - \psi_2) + \mathcal{R}_3. \end{aligned} \tag{3.56}$$

Here, $\upsilon_{\tau h}, z_{\tau h} \in X_{\tau h}$ and $p_{\tau h}, q_{\tau h} \in M_{\tau h}$ denote the approximate solutions of the primal and dual problems and the discrete functions $\varphi_1, \varphi_2 \in Y_{\tau h}$ and $\psi_1, \psi_2 \in M_{\tau h}$ may be chosen arbitrary. $\mathcal{R}_3$ denotes the remainder term. To calculate estimations of the error $J(\upsilon) - J(\upsilon_{\tau h})$ and corresponding error indicators, the unknown exact solutions in (3.56) are replaced by approximations and the remainder term is neglected as described in Section 3.2. The primal residual $\rho(\upsilon_{\tau h}, p_{\tau h})(Z, Q)$ with $(Z, Q) \in Y \times M$ has the form

$$\begin{aligned} \rho(\upsilon_{\tau h}, p_{\tau h})(Z, Q) &= \int_0^T \Big((\partial_t \upsilon_{\tau h} + (\upsilon_{\tau h} \cdot \nabla)\upsilon_{\tau h} - f, Z) + \nu(\nabla \upsilon_{\tau h}, \nabla Z)\\ &\quad - (p_{\tau h}, \nabla \cdot Z) + (\nabla \cdot \upsilon_{\tau h}, Q)\Big)\, dt + (\upsilon_{\tau h|t=0} - \upsilon_0, Z_{|t=0}). \end{aligned}$$

It is assumed that $\upsilon_0 \in V_h$ is an adequate start solution, hence $\upsilon_{\tau h|t=0} \equiv \upsilon_0$. The remaining integrals over the global space-time domain can be written as a sum of space-time integrals over all cells in the space-time mesh. For almost every $t \in (0, T)$ the spatial integral over cell $K \in \mathcal{T}_h(t)$ has the form

$$\begin{aligned} \rho_K &:= (\partial_t \upsilon_{\tau h} + (\upsilon_{\tau h} \cdot \nabla)\upsilon_{\tau h} - f, Z)_K - (p_{\tau h}, \nabla \cdot Z)_K + \nu(\nabla \upsilon_{\tau h}, \nabla Z)_K\\ &\quad + (\nabla \cdot \upsilon_{\tau h}, Q)_K\\ &= (\partial_t \upsilon_{\tau h} + (\upsilon_{\tau h} \cdot \nabla)\upsilon_{\tau h} - f + \nabla p_{\tau h} - \nu \Delta \upsilon_{\tau h}, Z)_K + (\nabla \cdot \upsilon_{\tau h}, Q)_K\\ &\quad + (\nu \partial_n \upsilon_{\tau h} - p_{\tau h} n, Z)_{\partial K}, \end{aligned}$$

where n denotes the outward unit normal vector of the boundary ∂K of cell K. On the boundary $\gamma := \partial K' \cap \partial \hat{K}$ between each pair of neighboring cells $K', \hat{K} \in \mathcal{T}_h(t)$ there are two contributions to the residual given by integrals over γ:

$$(\nu \partial_{n'} \upsilon'_{\tau h} - p'_{\tau h} n', Z')_\gamma \quad \text{and} \quad (\nu \partial_{\hat{n}} \hat{\upsilon}_{\tau h} - \hat{p}_{\tau h} \hat{n}, \hat{Z})_\gamma,$$

where $(\cdot)'$ and $\widehat{(\cdot)}$ denote the values of $(\cdot)$ on the cells K' and $\hat{K}$, respectively. Since Z is globally continuous (in space), it holds that $Z := Z' = \hat{Z}$ on γ. Furthermore, the normal unit vectors are anti parallel, i.e. $n := n' = -\hat{n}$, hence the residual contribution corresponding to γ is given by

$$(\nu \partial_{n'} \upsilon'_{\tau h} - p'_{\tau h} n', Z')_\gamma + (\nu \partial_{\hat{n}} \hat{\upsilon}_{\tau h} - \hat{p}_{\tau h} \hat{n}, \hat{Z})_\gamma = \nu([\partial_n \upsilon_{\tau h}], Z)_\gamma - ([p_{\tau h}] n, Z)_\gamma, \quad (3.57)$$

where $[\partial_n \upsilon_{\tau h}] := \partial_n \upsilon'_{\tau h} - \partial_n \hat{\upsilon}_{\tau h}$ denotes the jump of the normal derivative and $[p_{\tau h}] := p'_{\tau h} - \hat{p}_{\tau h}$ the jump of the pressure at the common cell boundary γ. For each cell $K \in \mathcal{T}_h(t)$ and each edge $\gamma \in \Gamma_h(t)$, the cell residual r and the edge residual R are given by:

$$\begin{aligned} R &:= \partial_t \upsilon_{\tau h} + (\upsilon_{\tau h} \cdot \nabla) \upsilon_{\tau h} - f + \nabla p_{\tau h} - \nu \Delta \upsilon_{\tau h}, \\ r &:= \begin{cases} \frac{1}{2} \nu [\partial_n \upsilon_{\tau h}] - \frac{1}{2} [p_{\tau h}] n, & \text{if } \gamma \not\subseteq \partial\Omega \text{ (inter-cell boundary)} \\ \nu \partial_n \upsilon_{\tau h} - p_{\tau h} n, & \text{if } \gamma \subseteq \partial\Omega. \end{cases} \end{aligned}$$

For the discretization in space with Taylor-Hood elements (see Section 2.4.2), the discrete pressure variable is globally continuous in space. In this case, the pressure contribution to the edge residual vanishes, i.e. $[p_{\tau h}] \equiv 0$. The primal residual corresponding to cell $K \in \mathcal{T}_h(t)$ and time interval $(t_{i-1}, t_i) \subseteq [0, T]$ can be written in the form

$$\rho_{K,i} := \int_{t_{i-1}}^{t_i} \Big((R, Z)_K + (\nabla \cdot \upsilon_{\tau h}, Q)_K + (r, Z)_{\partial K} \Big)\, dt. \quad (3.58)$$

To specify the dual residual $\rho^*_{\upsilon_h}(z_{\tau h}, q_{\tau h})(U, P)$ with $(U, P) \in Y \times M$, a goal functional J of the form

$$J(\upsilon) := \int_0^T \left\langle j^{(1)}, \upsilon \right\rangle_{V^*, V} dt + (j^{(2)}, \upsilon_{|t=T}),$$

is assumed. The residual is given by

$$\begin{aligned} \rho^*_{\upsilon_h}(z_{\tau h}, q_{\tau h})(U, P) \;=\; & \int_0^T \Big((j^{(1)} - \partial_t z_{\tau h}, U) + ((\upsilon_{\tau h} \cdot \nabla) U + (U \cdot \nabla) \upsilon_{\tau h}, z_{\tau h}) \\ & + \nu (\nabla z_{\tau h}, \nabla U) - (P, \nabla \cdot z_{\tau h}) + (\nabla \cdot U, q_{\tau h}) \Big)\, dt \\ & + (U_{|\mathrm{t=T}}, z_{\tau h|t=T} + j^{(2)}). \end{aligned}$$

Assuming $j^{(2)} \in V_h$, the contribution corresponding at $t = T$ vanishes, as $z_{\tau h|t=T} \equiv -j^{(2)}$. For almost all t, the contribution for cell $K \in \mathcal{T}_h(t)$ is

$$\begin{aligned} \rho^*_K \;:=\; & (j^{(1)} - \partial_t z_{\tau h}, U)_K + ((\upsilon_{\tau h} \cdot \nabla) U + (U \cdot \nabla) \upsilon_{\tau h}, z_{\tau h})_K + \nu (\nabla z_{\tau h}, \nabla U)_K \\ & - (P, \nabla \cdot z_{\tau h})_K + (\nabla \cdot U, q_{\tau h})_K \\ =\; & (j^{(1)} - \partial_t z_{\tau h} + ((\nabla \upsilon_{\tau h})^T - (\nabla \cdot \upsilon_{\tau h}) - (\upsilon_{\tau h} \cdot \nabla)) z_{\tau h} - \nu \Delta z_{\tau h} - \nabla q_{\tau h}, U)_K \\ & - (\nabla \cdot z_{\tau h}, P)_K + ((\upsilon_{\tau h} \cdot n) z_{\tau h} + \nu \partial_n z_{\tau h} + q_{\tau h} n, U)_{\partial K}, \end{aligned}$$

where integration by parts and the following identities have been utilized:

$$\begin{aligned}((U\cdot\nabla)\upsilon_{\tau h}, z_{\tau h})_K &= ((\nabla\upsilon_{\tau h})^T z_{\tau h}, U)_K,\\ ((\upsilon_{\tau h}\cdot\nabla)U, z_{\tau h})_K &= -((\nabla\cdot\upsilon_{\tau h})z_{\tau h}+(\upsilon_{\tau h}\cdot\nabla)z_{\tau h}, U)_K+((\upsilon_{\tau h}\cdot n)z_{\tau h}, U)_{\partial K}.\end{aligned}$$

The contributions corresponding to cell $K\in\mathcal{T}_h(t)$ and to each edge $\gamma\in\Gamma_h(t)$ are given in terms of the cell residuals R^* and the edge residuals r^*:

$$R^* := j^{(1)} - \partial_t z_{\tau h} + ((\nabla\upsilon_{\tau h})^T - (\nabla\cdot\upsilon_{\tau h}) - (\upsilon_{\tau h}\cdot\nabla))z_{\tau h} - \nu\Delta z_{\tau h} - \nabla q_{\tau h},$$

$$r^* := \begin{cases} \frac{1}{2}\nu[\partial_n z_{\tau h}] + \frac{1}{2}[q_{\tau h}]n, & \text{if } \gamma\not\subseteq\partial\Omega \text{ (inter-cell boundary)}\\ (\upsilon_{\tau h}\cdot n)z_{\tau h} + \nu\partial_n z_{\tau h} + q_{\tau h}n, & \text{if } \gamma\subseteq\partial\Omega.\end{cases}$$

If conforming finite element discretizations in space are used, both $\upsilon_{\tau h}$ and $z_{\tau h}$ are globally continuous and therefore the term $-(\upsilon_{\tau h}\cdot n)z_{\tau h}$ leads to a vanishing contribution at inter-cell boundaries. In case of Taylor-Hood elements, also the dual pressure variable $q_{\tau h}$ is continuous in space and the jump-term $[q_{\tau h}]\equiv 0$. The resulting dual residual corresponding to cell $K\in\mathcal{T}_h(t)$ and time interval $(t_{i-1}, t_i)\subseteq[0,T]$ has the form

$$\rho^*_{K.i} := \int_{t_{i-1}}^{t_i}\Big((R^*, U)_K - (\nabla\cdot z_{\tau h}, P)_K + (r^*, U)_{\partial K}\Big)\,dt. \tag{3.59}$$

Using the definitions (3.58) and (3.59) of the local residual contributions $\rho_{K,i}$ and $\rho^*_{K,i}$ of the primal and dual problems, respectively, the global residuals can be written as

$$\begin{aligned}\rho(\upsilon_{h\tau}, p_{h\tau})(Z,Q) &= \sum_{i=1}^{N_{time}}\sum_{K\in\mathcal{T}_h(i)}\rho_{K,i},\\ \rho^*_{\upsilon_{h\tau}}(z_{h\tau}, q_{h\tau})(U,P) &= \sum_{i=1}^{N_{time}}\sum_{K\in\mathcal{T}_h(i)}\rho^*_{K,i}.\end{aligned}$$

Choosing the test functions (Z,Q) and (U,P) adequately, the error characterizations based on (3.56) can be evaluated. Further, cellwise error indicators related to the space and time discretization can be defined as described in Section 3.2.2.

4 Stationary Problems

In this chapter, adaptive numerical simulations of stationary fluid problems with analytically known exact solution are presented. The scenarios are related to meteorological phenomena and are modeled using the incompressible Navier-Stokes equations in 2D. Since the exact solution – the velocity component is denoted by u – is known for these applications, the quantity of interest $J(u)$ can be determined. This allows the quantification of the error $J(u) - J(u_h)$ of approximate solutions u_h. In this case, the characteristics of goal-oriented error estimators for the error in J, i.e. $E(u_h) \approx J(u) - J(u_h)$, and resulting adaptive methods can be inspected by means of numerical experiments. In particular, different strategies for the approximation of the primal and dual solutions can be analyzed and compared regarding the resulting error estimates and optimized meshes.

The following variational formulation is the basis of the discrete model. For given non-homogeneous Dirichlet boundary conditions, $\upsilon \equiv g$ on $\partial\Omega$, the velocity function is split into the homogeneous part $\upsilon_0 \in V := H_0^1(\Omega)^2$ and a divergence-free part $\upsilon_g \in H^1(\Omega)$ with $\upsilon_g \equiv g$ on $\partial\Omega$. Then the variational formulation of the primal problem has the form: Find $(\upsilon_0, p) \in V \times Q$ such that

$$((\upsilon \cdot \nabla)\upsilon, \varphi) + \nu(\nabla\upsilon, \nabla\varphi) - (p, \nabla \cdot \varphi) + (\nabla \cdot \upsilon, \psi) = (f, \varphi), \tag{4.1}$$

for all $(\varphi, \psi) \in V \times Q$, where $\upsilon := \upsilon_g + \upsilon_0$. V denotes the space of the velocity field and $Q := L_0^2(\Omega) = \{p \in L^2(\Omega) \,|\, \int_\Omega p(x)\, dx = 0\}$ the pressure space. For a goal functional $J : H^1(\Omega)^d \to \mathbb{R}$, $\upsilon \mapsto (j^{(1)}, \upsilon)_\Omega$, the corresponding dual problem can be derived as described in Section 3.3. The dual problem has homogeneous Dirichlet boundary conditions and the corresponding variational formulation has the form: Find $(z, q) \in V \times Q$ such that

$$((\upsilon \cdot \nabla)\varphi + (\varphi \cdot \nabla)\upsilon, z) + \nu(\nabla z, \nabla\varphi) - (\psi, \nabla \cdot z) + (\nabla \cdot \varphi, q) = (-j^{(1)}, z), \tag{4.2}$$

for all $(\upsilon, p) \in V \times Q$. To calculate approximate solutions of problems (4.1) and (4.2) the function spaces V and Q are conformingly discretized using Taylor-Hood elements, see Section 2.4.2 for details. The iterative procedure of error estimation and mesh refinement, denoted by Dual Weighted Residual (DWR) method, is illustrated in Algorithm 4.1. Starting with an initial coarse uniform mesh, the primal and dual problems are solved, and the error in the user-defined goal functional J of the approximate solution is estimated and localized. Based on the resulting cellwise error indicators, the underlying mesh is refined. Due to the employed mesh adaptation strategy, all cells with error indication higher than a given fraction $\alpha \in [0, 1]$ of the highest error indicator in the current mesh will be refined. In the ith iteration of the DWR method, assuming an error indication $\eta_K^{(i)} \geq 0$ for each cell $K \in T_h(i)$, the cells in the set

$$A(i) := \left\{ K \in \mathcal{T}_h^{(i)} \,|\, \eta_K^{(i)} \geq \alpha \eta_{max}^{(i)} \right\}, \quad \eta_{max}^{(i)} := \max_{K \in \mathcal{T}_h^{(i)}} \{\eta_K^{(i)}\},$$

Algorithm 4.1 Adaptation cycle of the DWR method.

```
1. $i \leftarrow 0$
2. Calculate discrete primal solution $(v_h, p_h) \in V_h \times Q_h$
3. Calculate discrete dual solution $(z_h, q_h) \in V_h \times Q_h$
4. Calculate higher-order solutions $(U, P) \approx (u, p)$ and $(Z, Q) \approx (z, q)$
5. Estimate error in $J$ and compute error indicators
6. Refine cells $K \in A(i)$
7. Quit, if number of degrees of freedom $> M_{DOF}$
8. $i \leftarrow i + 1$ and repeat with step 2
```

are selected to be refined. This refinement iteration is repeated until a user-defined maximal number of degrees of freedom $M_{DOF} > 0$ is achieved. For symmetrical scenarios, this strategy allows the same treatment of cells with identical error indication which leads to symmetrical meshes. For the numerical simulations presented in the following, the refinement parameter is set to $\alpha = 1/16$. Since cells with a large error contribution are refined in each iteration step, the resulting meshes tend towards a uniform distribution of the estimated error contribution.

In the following, the considered scenarios are introduced. Thereafter the corresponding goal-oriented adaptive simulations based on different variants of the error estimator are presented and compared. The simulations were performed using the multi-purpose finite element library **HiFlow³** [28]. The reference values of the quantities of interest were calculated at high number of digits of precision using Maple$^{\text{TM}}$ [35]. This high precision is needed, since on adapted meshes very accurate approximations can be calculated. The following investigation has already been published in [4].

4.1 Taylor-Green Vortex

The first scenarios are based on the well-known Taylor-Green vortex [14] consisting of two pairs of counter-rotating vortices. The analytical solution of the Navier-Stokes equations is given by

$$\begin{aligned} v_1(x) &:= -e^{-2}\cos(x_1)\sin(x_2), \\ v_2(x) &:= e^{-2}\sin(x_1)\cos(x_2), \\ p(x) &:= -e^{-4}(\cos(2x_1)+\cos(2x_2))/4, \end{aligned}$$

on the domain $\Omega = [\frac{1}{2}\pi; \frac{5}{2}\pi]^2$. Figure 4.1 shows the velocity field in terms of glyphs and the corresponding coloring is based on the vorticity (curl of the velocity field), where blue regions mark clockwise and red regions mark counter-clockwise rotations. Furthermore, the pressure field is shown, where regions of low pressure are located within the vortices. The corresponding right-hand side of the Navier-Stokes equations with kinematic viscosity $\nu = 1$ is given by

$$\begin{aligned} f_1(x) &= -2e^{-2}\cos(x_1)\sin(x_2), \\ f_2(x) &= 2e^{-2}\sin(x_1)\cos(x_2). \end{aligned}$$

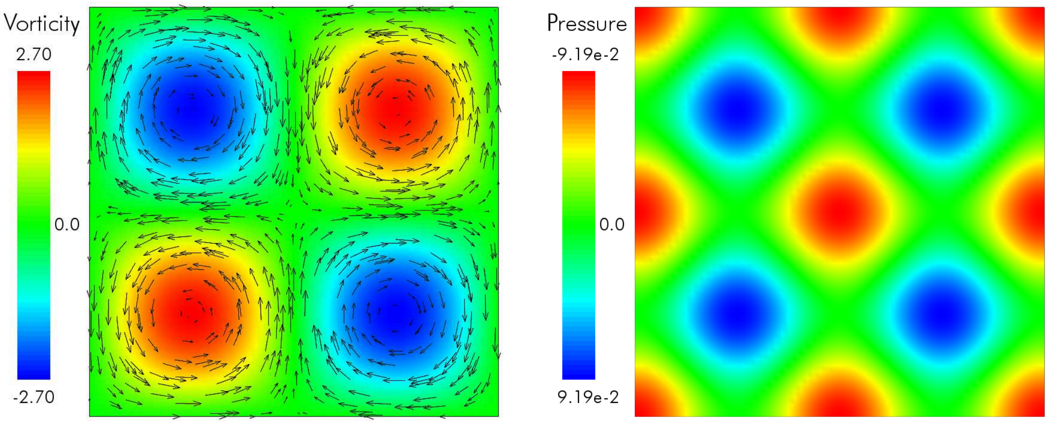

Figure 4.1: Taylor-Green vortex: Velocity field, colored by vorticity (left) and pressure (right).

4.1.1 Scenario 1: Point Value of Velocity

For a given point $\hat{x} \in \Omega$, the x_1-component of the velocity at this position is the quantity of interest. The goal functional is defined as the regularized point value by means of an integral over a small neighborhood:

$$v_1(\hat{x}) \approx J_1(v) := \frac{1}{|B(\hat{x},\epsilon)|} \int_{B(\hat{x},\epsilon)} v_1(x)\, dx.$$

Here, $B(\hat{x},\epsilon)$ is a ball with radius $\epsilon > 0$, centered at $\hat{x}$ and $|B(\hat{x},\epsilon)|$ its surface. The radius is $\epsilon := \epsilon(h_{min}) := h_{min}/4$, where $h_{min} := \min_{K\in\mathcal{T}_h} \{\operatorname{diam} K\}$ is the smallest cell diameter in the mesh $\mathcal{T}_h$. For point $\hat{x} = (6.2, 3.8)$ the reference value is

$$J_1(v) \approx J_1^{\text{ref}} := 8.2519625992351e - 2.$$

In Figure 4.2 the dual velocity corresponding to J_1 is visualized. Further an example of an optimized mesh after several loops of the DWR method is shown.

4.1.2 Scenario 2: Weighted Integral of Vorticity (I)

For this scenario the quantity of interest is defined on a larger region in terms of a weighted integral of the vorticity, i.e.

$$J_2(v) := \int_\Omega w_1(x) \cdot \nabla \times v(x)\, dx,$$

with reference value

$$J_2(v) \approx J_2^{\text{ref}} := 4.2212012520232e - 1.$$

The weight function is defined by

$$w_1(x) := \sin\left(-\frac{x_1^2}{4\pi} + \frac{5x_1}{4} - \frac{9\pi}{16}\right) \sin\left(-\frac{x_2^2}{4\pi} + \frac{5x_2}{4} - \frac{9\pi}{16}\right), \quad x \in \Omega,$$

and is visualized in Figure 4.3. The velocity of the dual solution and an optimized mesh corresponding to this goal functional is shown in Figure 4.4.

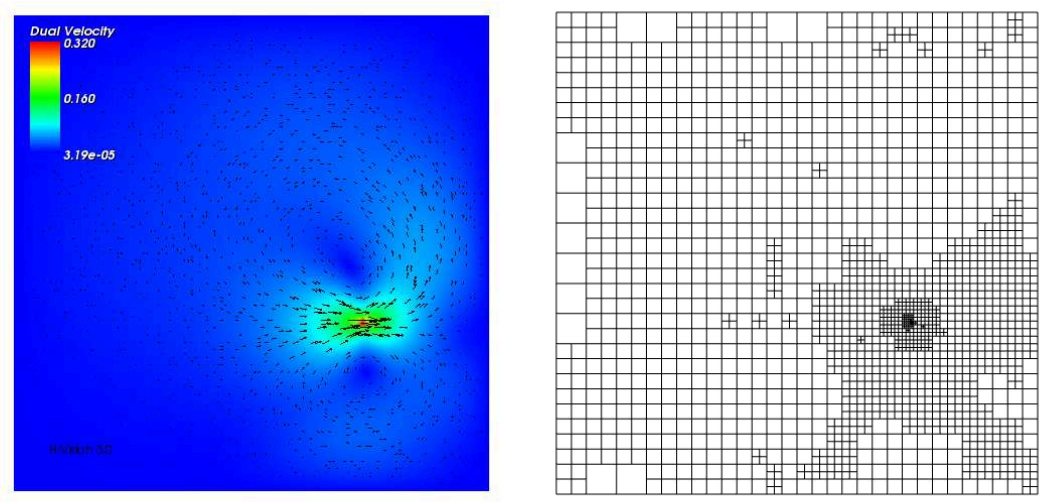

Figure 4.2: Point value of velocity, scenario 1: (left) dual velocity and (right) example of an optimized mesh.

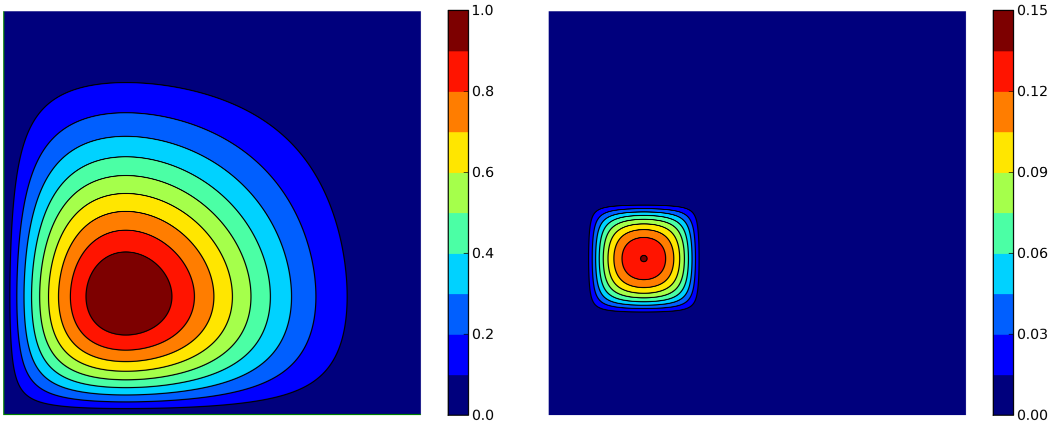

Figure 4.3: Weight function ω_1 related to scenario 2 (left) and weight function ω_2 related to scenario 3 (right).

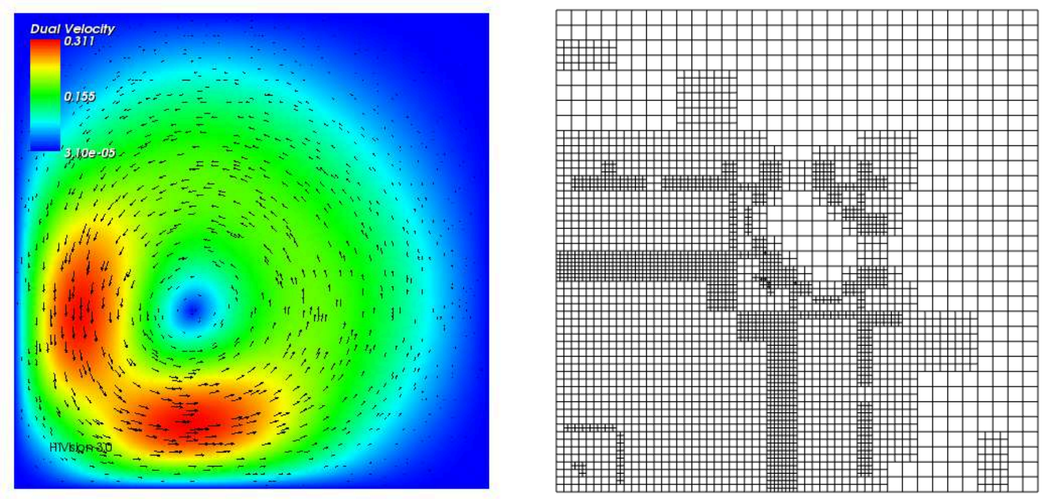

Figure 4.4: Weighted integral of vorticity (I), scenario 2: (left) dual velocity and (right) example of an optimized mesh.

4.1.3 Scenario 3: Weighted Integral of Vorticity (II)

For point $\tilde{x} = (3.0, 4.0)$, a weight function with small support close to $\tilde{x}$ is defined by

$$w_2(x) := \begin{cases} \exp\left(\frac{1}{(x_1-\tilde{x}_1)^2-1} + \frac{1}{(x_2-\tilde{x}_2)^2-1}\right), & \text{if } \|x-\tilde{x}\|_\infty \leq 1 \\ 0, & \text{else,} \end{cases},$$

see also Figure 4.3. The goal functional is defined as the weighted integral of vorticity, i.e.

$$J_3(v) := \int_\Omega w_2(x) \cdot \nabla \times v(x)\, dx,$$

and the reference value is

$$J_3(v) \approx J_3^{\text{ref}} := 2.9422745464403e-2.$$

A visualization of the dual velocity and corresponding mesh is shown in Figure 4.5.

4.2 Single Vortex

The following scenarios include a simplified tropical cyclones defined as monopolar vortex with smooth vorticity profile and azimuthal velocity, called *Gaussian vortex*. Such idealized representations of tropical cyclones are used e.g. by Scheck et al. [38] to investigate the dynamical behavior of such phenomena. For $\Omega := [-1, 1]^2$

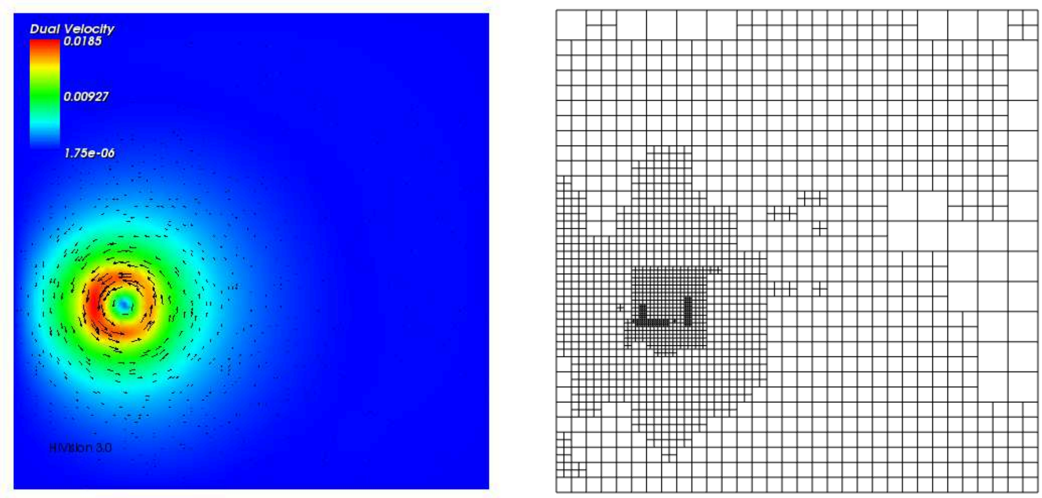

Figure 4.5: Weighted integral of vorticity (II), scenario 3: (left) dual velocity and (right) example of an optimized mesh.

the exact solution is given by

$$\begin{aligned} v_1(x) &:= \frac{x_2}{r_0^2} \cdot e^{-\frac{x_1^2+x_2^2}{2r_0^2}}, \\ v_2(x) &:= -\frac{x_1}{r_0^2} \cdot e^{-\frac{x_1^2+x_2^2}{2r_0^2}}, \\ p(x) &:= -\frac{1}{2r_0^2} \cdot e^{-\frac{x_1^2+x_2^2}{r_0^2}}. \end{aligned}$$

Figure 4.6 shows the corresponding velocity field in terms of glyphs and coloring based on the vorticity. Regions of low pressure are located in the vortex core. The radius parameters is set to $r_0 = 0.15$ and the kinematic viscosity to $\nu = 1$. The corresponding right-hand side of the Navier-Stokes equations is defined by

$$\begin{aligned} f_1(x) &= \nu \frac{x_2(4r_0^2 - x_1^2 - x_2^2)}{r_0^6} \cdot e^{-\frac{x_1^2+x_2^2}{2r_0^2}}, \\ f_2(x) &= -\nu \frac{x_1(4r_0^2 - x_1^2 - x_2^2)}{r_0^6} \cdot e^{-\frac{x_1^2+x_2^2}{2r_0^2}}, \end{aligned}$$

and corresponds to effects of viscosity, since (v_1, v_2, p) is a solution of the Euler equations, i.e. $\nu = 0$, with homogeneous right-hand side.

4.2.1 Scenario 4: Point Value of Vorticity

The vorticity at the point $\bar{x} = (0.35, 0.45)$ is the quantity of interest and the corresponding goal functional is defined as the following regularization:

$$\nabla \times v(\bar{x}) \approx J_4(v) := \frac{1}{|B(\bar{x}, \epsilon)|} \int_{B(x_0,\epsilon)} \nabla \times v(x)\, dx.$$

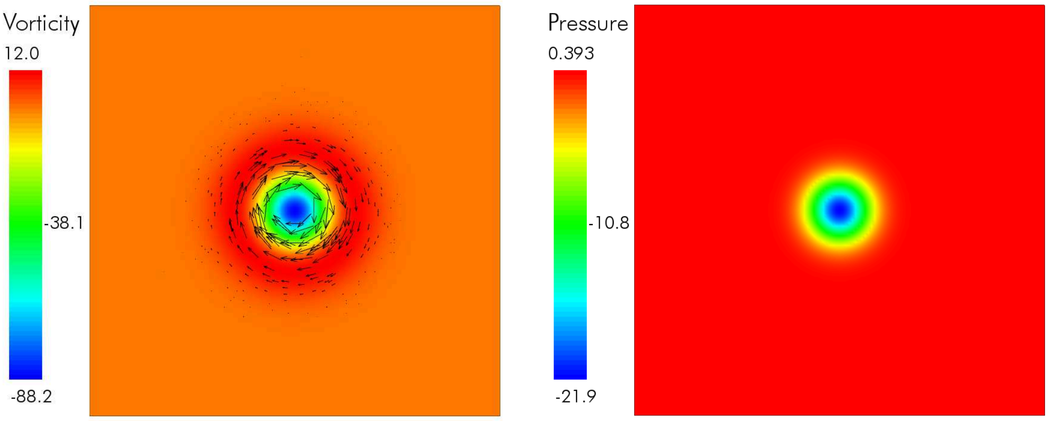

Figure 4.6: Single vortex: Velocity field, colored by vorticity (left) and pressure (right).

Again, $B(\bar{x}, \epsilon)$ is a ball with radius $\epsilon > 0$, centered at $\bar{x}$, $|B(\bar{x}, \epsilon)|$ its surface and $\epsilon := h_{min}/4$, where $h_{min} := \min_{K \in \mathcal{T}_h} \{\operatorname{diam} K\}$ is the smallest cell diameter in the current mesh $\mathcal{T}_h$. The vorticity at point $\bar{x}$ can be evaluated to be

$$J_4(v) \approx J_4^{\text{ref}} := 4.0385153437245e - 1.$$

A visualization of the dual velocity and an optimized mesh is given in Figure 4.7.

4.2.2 Scenario 5: Kinetic Energy

For the last scenario in this chapter, the goal functional is defined as integrated kinetic energy over the domain Ω, i.e.

$$J_5(v) := \|v\|_\Omega^2 = (v, v)_\Omega = \int_\Omega v(x) \cdot v(x)\, dx.$$

As this goal functional is nonlinear, the right-hand side of the dual problem is defined in terms of its linearization, i.e. $(j^{(1)}, \varphi)_\Omega := -\nabla J_5(v)\varphi$. The linearization is given by

$$\begin{aligned}
\nabla J_5(v)(\varphi) &= \lim_{\lambda \to 0} \frac{J_5(v + \lambda\varphi) - J_5(v)}{\lambda} \\
&= \lim_{\lambda \to 0} \frac{1}{\lambda} \left[(v + \lambda\varphi, v + \lambda\varphi)_\Omega - (v, v)_\Omega\right] \\
&= \lim_{\lambda \to 0} \frac{1}{\lambda} \left[(v, v)_\Omega + 2\lambda(v, \varphi)_\Omega + \lambda^2(\varphi, \varphi)_\Omega - (v, v)_\Omega\right] \\
&= 2(v, \varphi)_\Omega.
\end{aligned}$$

The reference value for the integrated kinetic energy is

$$J_5(v) \approx J_5^{\text{ref}} := 3.1415926535898.$$

The dual solution and an optimized mesh is shown in Figure 4.8.

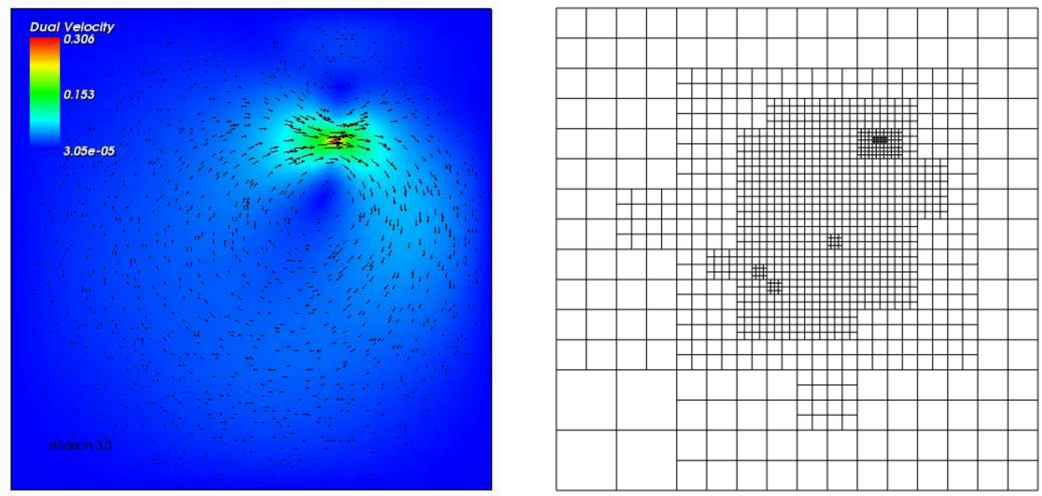

Figure 4.7: Point value of vorticity, scenario 4: (left) dual velocity and (right) example of an optimized mesh.

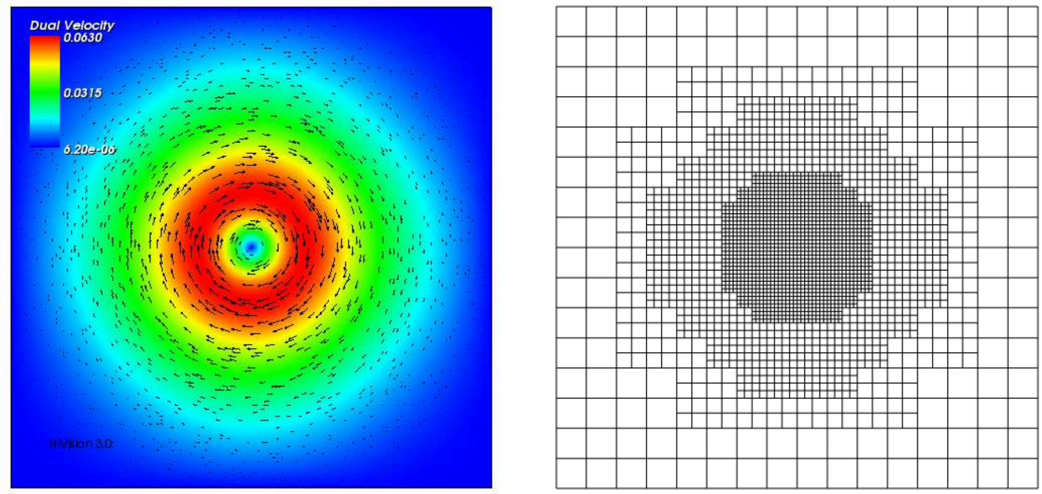

Figure 4.8: Kinetic Energy, scenario 5: (left) dual velocity and (right) example for an optimized mesh.

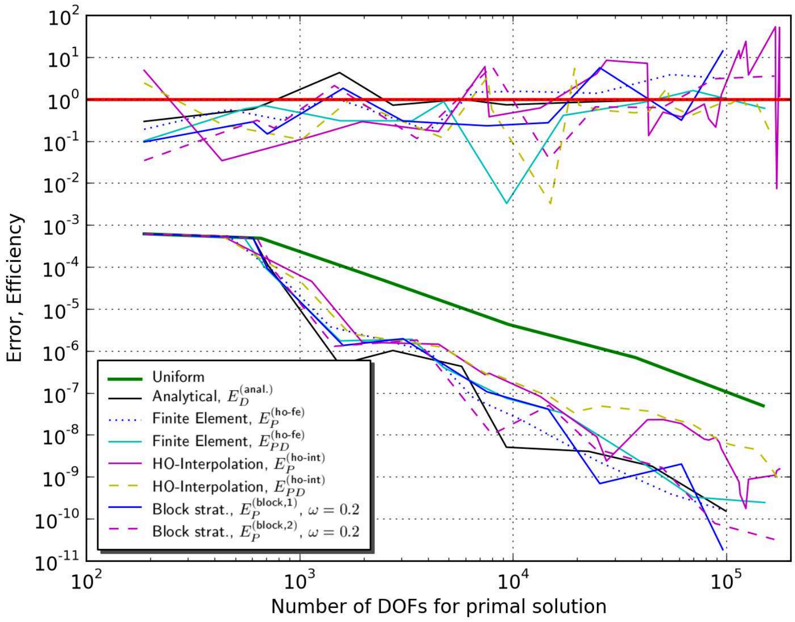

Figure 4.9: Error and efficiency plots for scenario 1.

4.3 Numerical Results

For the presented scenarios and estimator variants, sequences of numerical simulations on uniform as well as locally refined meshes have been carried out. Based on these simulations, the quality of the error estimations and the resulting adaptive methods can be quantified. The efficiency of the estimators is analyzed on uniform meshes in terms of the *efficiency index* defined by

$$I_{\text{eff}} := \left| \frac{E(\upsilon_h)}{J(\upsilon) - J(\upsilon_h)} \right|. \tag{4.3}$$

Estimators are efficient if I_{eff} is close to one. In this case, the estimation is close to the true error. It must be noted, that the efficiency index can be evaluated in this special case, since the reference value $J(\upsilon)$ is known, because the exact solution υ and the definition of the goal functional J are given analytically. The error estimation $E(\upsilon_h)$ stands for the the variants E_{PD}, E_P and E_D as defined by (3.18), (3.19) and (3.20). The finite element solutions of the primal and dual problems are Galerkin approximations of (4.1) and (4.2) in discrete spaces consisting of Taylor-Hood elements $\mathcal{Q}_2/\mathcal{Q}_1$. For the error estimator variants E_{PD}, E_P and E_D a further upper index is added that denotes the strategy used to determine the replacement of the exact solution. The short names as well as the finite element spaces corresponding to the different strategies are given in the following table:

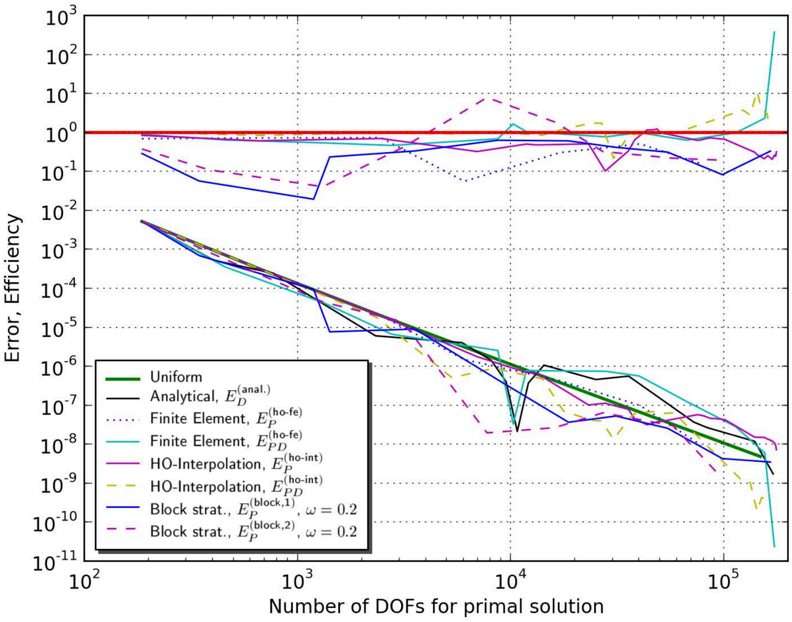

Figure 4.10: Error and efficiency plots for scenario 2.

Strategy	Short Name	Structure
Higher-order finite element solution	ho-fe	$\mathcal{Q}_3/\mathcal{Q}_2$
Block strategy (with n iterations)	block,n	$\mathcal{Q}_3/\mathcal{Q}_2$
Higher-order interpolation	ho-int	$\mathcal{Q}_4/\mathcal{Q}_2$
Analytical solution	anal.	anal. repr.

Each of Figure 4.9-4.13 shows the error $J(v) - J(v_h)$ and the corresponding efficiency index for sequences of adaptive simulations for the different scenarios. The thick green line corresponds to solutions on uniform meshes. The efficiency plots indicate to what extent an estimated error (given by the error estimator) and corresponding true error in J (by evaluation of $J(v) - J(v_h)$) agree. In the appendix, for each scenario and error estimator variant, details of numerical simulations based on uniform meshes are given in a series of tabulars. These include the efficiency index, the estimated error $E(v_h)$ in its different variants, the true error in J and the error of the post-processed value $\tilde{J}(v_h)$, as defined in Section 3.2.3.

To analyze the efficiency of the error estimators, the following reduction of the efficiency indices for the scenarios and estimator variants is performed. The mean relative deviation of the efficiency indicators (MRD)

$$MRD := \frac{1}{N}\sum_{i=1}^{N} I_{\text{rel}}(i), \quad I_{\text{rel}} := \frac{|1 - I_{\text{eff}}|}{\min(1, I_{\text{eff}})},$$

is introduced to quantify the difference between the estimated error and the real error in J. Tabular 4.1 and 4.2 contain the MRD corresponding to uniform and locally refined meshes, respectively. For each combination of scenario and error

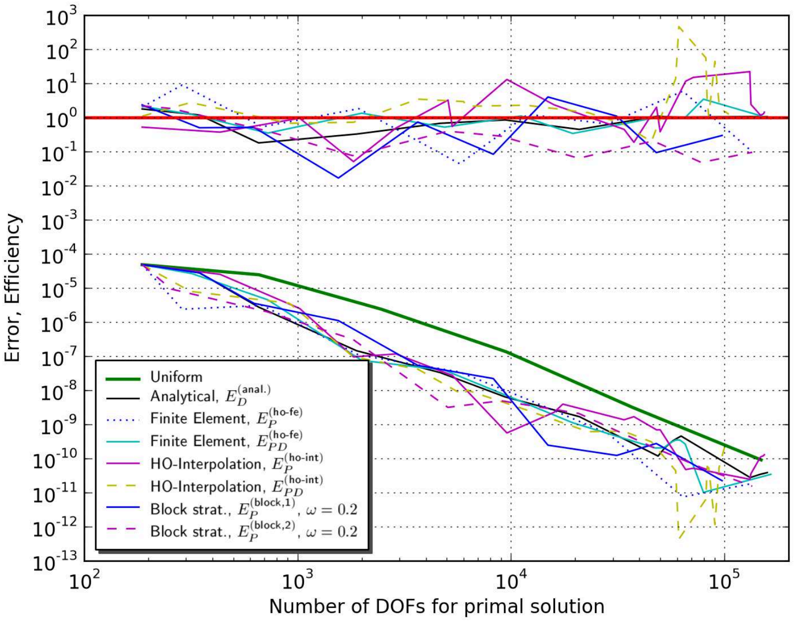

Figure 4.11: Error and efficiency plots for scenario 3.

estimator variant, the MRD is determined. In doing so, all consecutively refined meshes resulting from the adaptation cycle of the DWR method and accordingly the series of uniform meshes are considered. The last row shows a further reduction in terms of the mean average of the MRD values standing above, which is discussed in the following.

The error estimator variant $E_D^{(\text{anal.})}$ makes use of the analytical solution of the primal problem and has the lowest MRD. Although this variant cannot be used for general applications since the exact solution is typically unknown, it can serve as a reference for the current investigation. The ordering of the evaluation strategies with respect to the averaged MRD values roughly reflects the computational cost associated with the evaluation of the error estimators. The estimators that make use of higher-order finite element solutions, $E_P^{(\text{ho-fe})}$ and $E_{PD}^{(\text{ho-fe})}$, are the most efficient ones, but are computationally expensive. The estimators based on higher-order interpolation, $E_P^{(\text{ho-int})}$ and $E_{PD}^{(\text{ho-int})}$, show higher MRD but are comparably cheap to compute. The block strategy leads to estimators $E_P^{(\text{block,1})}$ and $E_P^{(\text{block,2})}$ that have MRD in between.

The economy of the adaptive methods can be quantified in terms of the ratio of the error in J and the related number of unknowns of the underlying discrete model. Figures 4.9-4.13 show that except for scenario 2, the DWR method based on different error estimators leads to economical meshes on which the quantity of interest can be approximated more accurately compared to uniform meshes with the same number of unknowns. The error in J is approximately reduced by one order of magnitude compared to uniform meshes. Furthermore, it can be observed that the block strategy leads to slightly more economical meshes, especially for the

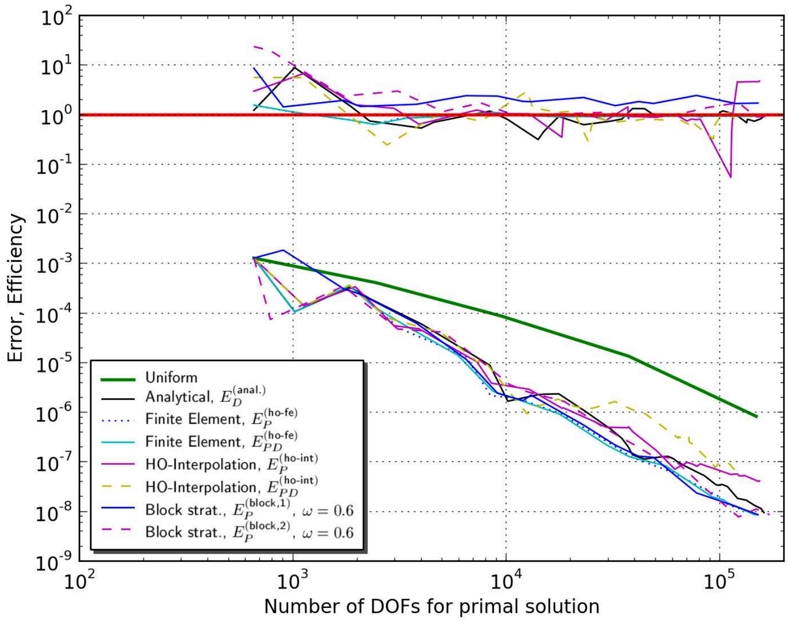

Figure 4.12: Error and efficiency plots for scenario 4.

	$E_D^{(\text{anal.})}$	$E_P^{(\text{ho-fe})}$	$E_{PD}^{(\text{ho-fe})}$	$E_P^{(\text{ho-int})}$	$E_{PD}^{(\text{ho-int})}$	$E_P^{(\text{block,1})}$	$E_P^{(\text{block,2})}$
Scen.1	0.75	0.76	0.75	2.76	7.22	3.30	2.47
Scen.2	0.00	0.40	0.11	0.47	0.18	2.20	1.76
Scen.3	1.02	1.18	1.07	1.74	3.82	3.35	2.81
Scen.4	1.44	1.67	1.67	3.17	1.58	0.89	2.02
Scen.5	0.00	0.01	0.01	0.06	0.08	0.19	0.19
Avg.	**0.64**	**0.8**	**0.72**	**1.64**	**2.58**	**1.99**	**1.85**

Table 4.1: MRD for series of simulations on uniform meshes.

scenarios 1,4 and 5.

The post-processed goal value $\tilde{J}(\upsilon_h)$, introduced in Section 3.2.3, and the canonical approximation $J(\upsilon_h)$ can be compared based on the values given in the tabulars in the appendix. For the majority of the performed numerical simulations, the post-processed goal value, represents a better approximation of the exact value $J(\upsilon)$ than the alternative $J(\upsilon_h)$. In most instances, the error $|\tilde{J}(\upsilon_h) - J(\upsilon)|$ is up to one order of magnitude lower than $|J(\upsilon_h) - J(\upsilon)|$, and for scenarios 2 and 5, the enhancement is significantly higher.

4.4 Concluding Remarks

Based on the presented numerical simulations, the reliability of the a posteriori error representation can be quantified. For the considered scenarios, the error estimations are good approximations of the true error in J for approximate solutions calculated

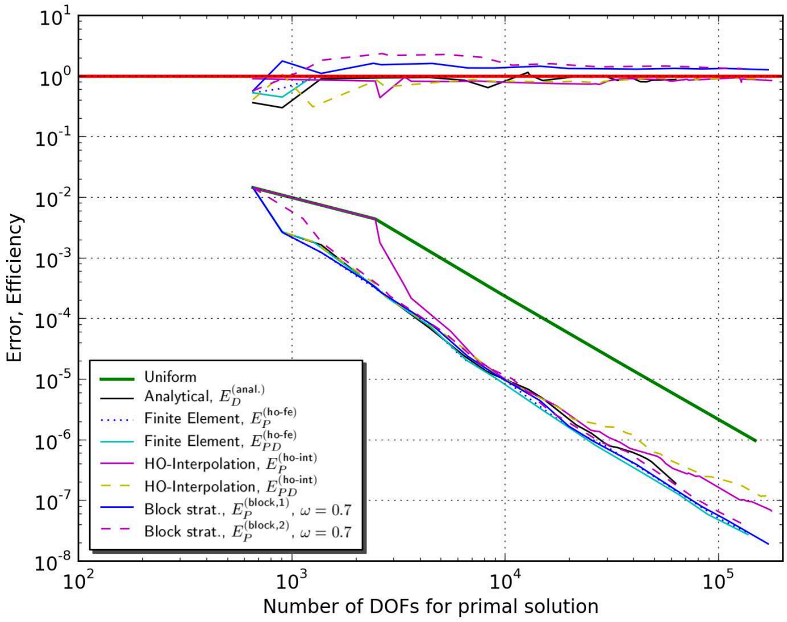

Figure 4.13: Error and efficiency plots for scenario 5.

	$E_D^{(\text{anal.})}$	$E_P^{(\text{ho-fe})}$	$E_{PD}^{(\text{ho-fe})}$	$E_P^{(\text{ho-int})}$	$E_{PD}^{(\text{ho-int})}$	$E_P^{(\text{block},1)}$	$E_P^{(\text{block},2)}$
Scen.1	0.77	1.82	29.35	13.24	15.31	4.66	7.19
Scen.2	0.00	3.91	28.81	1.57	1.14	8.64	5.91
Scen.3	0.66	5.15	0.58	4.56	26.94	8.88	6.74
Scen.4	0.51	0.18	0.17	1.74	0.84	1.26	2.72
Scen.5	0.34	0.11	0.15	0.21	0.24	0.41	0.65
Avg.	**0.46**	**2.23**	**11.81**	**4.26**	**8.89**	**4.77**	**4.64**

Table 4.2: MRD for series of simulations on adapted meshes.

on uniform as well as adapted meshes. Except for scenario 2, the efficiency of the optimized meshes is significantly higher compared to uniform meshes. This suggests that the underlying error indicators and the mesh refinement strategy are appropriate.

The evaluation of the error estimators requires the calculation of a higher-order replacement of the exact primal and dual solutions. The related computational cost roughly reflects the quality of the approximation in terms of the efficiency of the resulting estimation and the economy of corresponding adaptive methods. The higher-order interpolation strategy can lead to good error estimations that can be calculated at very low cost. But for the efficient calculation, a patch-structure of the underlying mesh is needed. The proposed block strategy offers the ability to control the quality of the approximation and the computational effort in terms of adequate stopping criteria of the iteration. Furthermore, it has good parallelization potential and does not require a patch-structure of the underlying mesh.

5 The Instationary Problem

In this chapter, a posteriori error estimators and related techniques of goal oriented adaptivity that have been discussed in Chapter 3 are applied to a scenario of tropical cyclone (TC) dynamics. In the context of such instationary problems, both the primal and dual problem are time-dependent and can lead to intensive computations and large memory requirements. Accurate mesh adaptation strategies are vital to construct economical discretizations at reasonable efforts.

In the following, the scenario of two mutually interacting TCs is presented and goal functionals are introduced that are correlated with the storm positions. Subsequently, a detailed description of the adaptive method is given. This includes aspects related to the calculation of the error estimator and mesh adaptation strategy for the space-time discretization. Finally, the numerical results based on the proposed goal functionals are reported and discussed with respect to different error metrics.

5.1 Interacting Tropical Cyclones

Once a TC has formed over warm tropical waters, the motion of the storm is influenced by several effects. At low latitudes, the trade winds move the storm in westward direction. The Coriolis force, due to the Earth's rotation, leads to a motion in northwestern direction for counter-clockwise (cyclonic) vortices. Once the storm enters the mid-latitudes, it is advected eastward, before it is dissolved or converted into an extra-tropical cyclone. Landfalling TCs can cause tremendous damage and are among the most lethal geophysical hazards. Therefore, the prediction of the storm tracks and intensity is an important problem and subject of current research, for an overview see [18]. While considerable progress in predicting TC motion has been made in the last decades, there are situations in which it is particularly difficult to forecast the TC track. One of these situations is the interaction of two TCs, which can change the storm structure and lead to complex tracks.

In this work, the interaction of two TCs is investigated based on an idealized model. The storms are represented by vortices that are closely located such that their profiles overlap at the initial state. During the first hours, the storms start orbiting around each other. Depending on the initial separation distance, the two cyclones can merge after some time or move in different directions, i.e. diverge from one another. The two idealized TCs are located within a space-periodic domain $\Omega := [-L_1, L_1] \times [-L_2, L_2]$, where $L_1 = 2000\,\mathrm{km}$ and $L_2 = 1732\,\mathrm{km}$. The initial separation of the two storms is $D = 400\,\mathrm{km}$. The initial position of the vortices is $(-D/2, 0)$ and $(D/2, 0)$. Both vortices have the same symmetrical profiles which are defined in terms of their tangential wind field as introduced in [42]:

$$v_T(s) = v_0 \frac{s(1 + (6b/2a)s^4)}{(1 + as^2 + bs^6)^2}, \tag{5.1}$$

where $s := r/r_0$. For $a = 0.3398$, $b = 5.377 \times 10^{-4}$, $v_0 = 71.521\,\mathrm{m/s}$ and $r_0 = 100\,\mathrm{km}$. The maximal tangential wind is $40\,\mathrm{m/s}$ at the radius $r = r_0$. The initial condition of the velocity field is defined as a sum of the velocity profiles of the two storms. For this scenario, a time horizon of $T := 96\,\mathrm{h}$ is considered.

In Figure 5.1, the motion and development of the two storms during the first 96 hours is visualized in terms of the vorticity (curl of the velocity field). Red areas indicate high vorticity regions and represent the storm positions. Dark blue regions indicate zones of negative vorticity resulting from the wind profile (5.1) and correspond to the anticyclonic outflow of real TCs. During the first hours, the two vortices start orbiting around each other. In this phase, the cores are strongly deformed and temporarily connected. Also the zone of negative vorticity around the cores is restructured and after 12 hours two separate negative vorticity regions have developed. These regions can be interpreted as anticyclones. Together with the positive cores they form two cyclone-anticyclone pairs that start to propagate away from each other along straight tracks. The moment at which the motion turns from orbiting into straight direction determines the final direction of the storm tracks. Small perturbations in the initial state can influence when this transition takes place and thus can have a strong influence on the final storm positions. The high sensitivity to the initial conditions is also evident from the fact that for a slightly smaller initial separation, a qualitatively different solution is found – the two TCs merge, see Figure 5.2. In a cooperation with the Institute for Meteorology and Climate Research (IMK) at the Karlsruhe Institute of Technology (KIT), this scenario has been chosen as a benchmark problem for adaptive methods.

Several investigations of interacting TCs can be found in the literature. In [41], the authors analyze the connection between the vorticity distribution of the storms and the possibility of a merger depending on the initial separation. The formation of fast propagating cyclone-anticyclone pairs is investigated in [49]. The cyclone-anticyclone pair formation discussed before is analyzed in [6] based on numerical simulations and laboratory experiments, see Figure 5.3.

5.2 Model

The dynamics of the idealized TCs can be described by means of the two-dimensional barotropic model introduced in Section 2.3. The kinematic viscosity parameter is set to $\nu = 0.005\,\mathrm{km^2/s}$. Since the Coriolis acceleration corresponds mainly to a moving frame of reference for this scenario, its contribution is neglected. The barotropic model corresponds to the time-dependent incompressible Navier-Stokes equations in 2D, i.e.

$$\begin{aligned}
\partial_t v + (v \cdot \nabla) v - \nu \Delta v + \nabla p &= 0 \quad \text{in } [0,T] \times \Omega, && (5.2)\\
\nabla \cdot v &= 0 \quad \text{in } [0,T] \times \Omega, && (5.3)\\
v_{|t=0} &= v_0 \quad \text{in } \Omega, && (5.4)
\end{aligned}$$

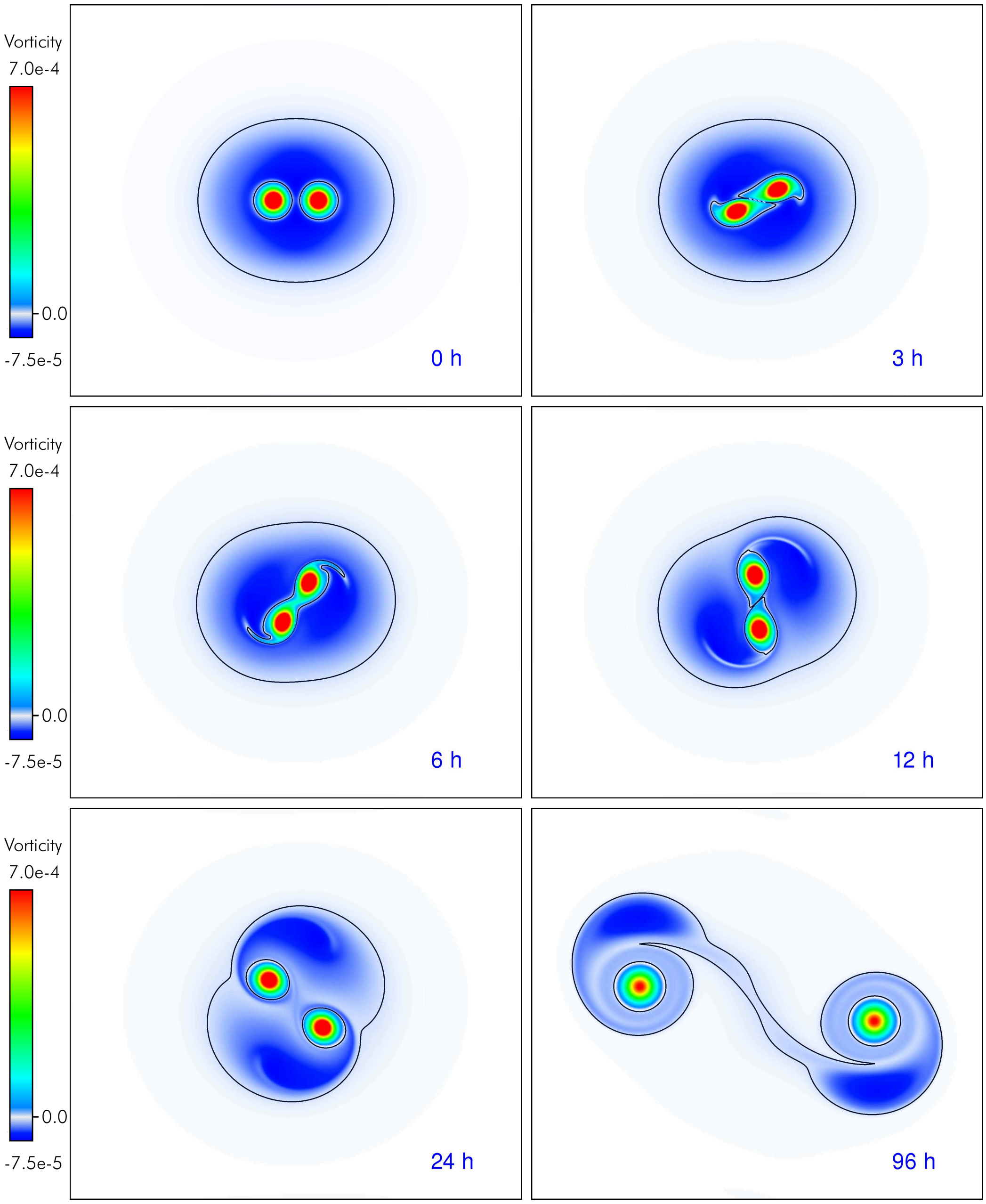

Figure 5.1: Development of two idealized tropical cyclones. Red regions indicate the position of the storm cores. The black contour line highlights vorticity of $-8.0 \cdot 10^{-6}\,1/\mathrm{s}$.

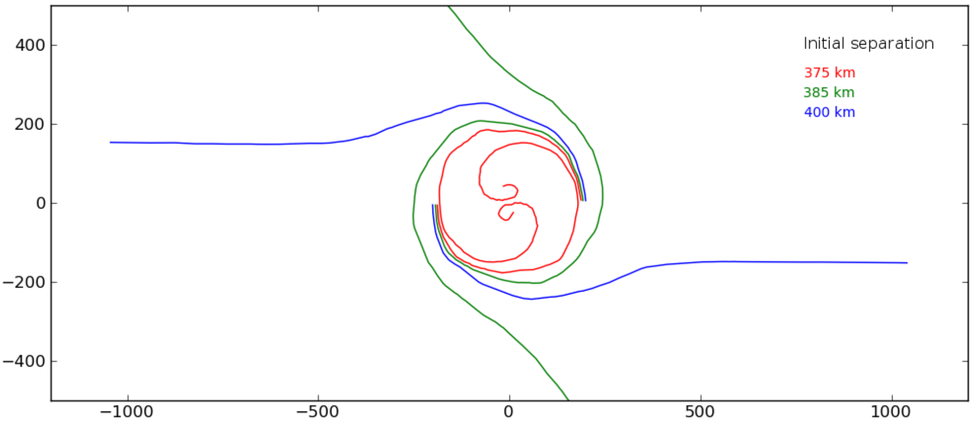

Figure 5.2: Initial separation distances of 375 km, 385 km and 400 km lead to strongly varying storm tracks: For initial separation of 375 km, the two vortices merge.

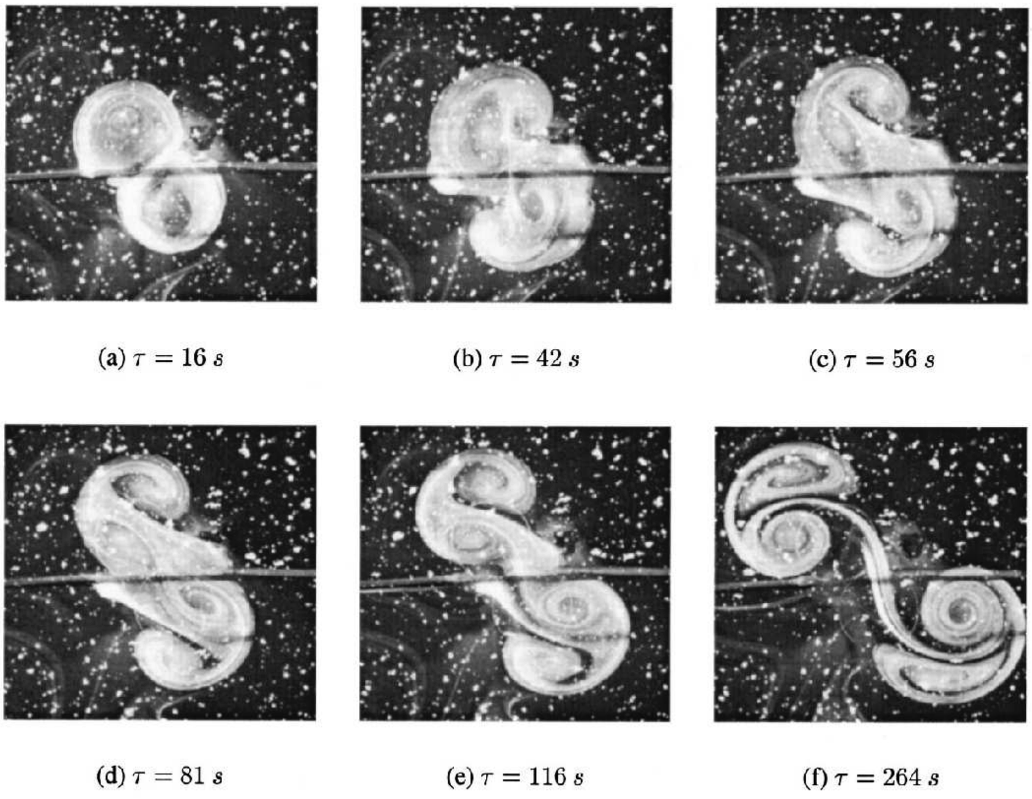
(a) $\tau = 16\ s$
(b) $\tau = 42\ s$
(c) $\tau = 56\ s$
(d) $\tau = 81\ s$
(e) $\tau = 116\ s$
(f) $\tau = 264\ s$

Figure 5.3: Photographs of a laboratory experiment of two interacting vortices conducted by Beckers et al. [6]. Reprinted with permission from Beckers, M.; Clercx, H. J. H.; van Heijst, G. J. F. & Verzicco, R., Dipole formation by two interacting shielded monopoles in a stratified fluid, *Phys. Fluids*, **2002**, *14*, 704–720. Copyright 2002, American Institute of Physics.

equipped with a periodic boundary condition in space:

$$v(t, x + 2L_i e_i) = v(t, x), \quad p(t, x + 2L_i e_i) = p(t, x) \quad i = 1, 2, \tag{5.5}$$

for all $x \in \mathbb{R}^2$ and all $t \in [0, T]$. For problem (5.2)-(5.5), a variational formulation of the form (2.11) is considered. Approximate solutions are calculated in terms of a space-time finite element discretization. Applying the cGP(1) method, the trial functions for the velocity are piecewise linear and globally continuous functions in time, whereas the trial functions for the pressure as well as all test functions are piecewise constant. For the discretization in space, stable Taylor-Hood elements $\mathcal{Q}_2/\mathcal{Q}_1$ are employed. The initial velocity field of the discrete problem is defined as the projection of v_0 into the space of discrete divergence-free functions. Details for these discretization aspects are given in Section 2.4.

5.3 Definition of Goal Functionals

For the following investigations, the storm positions after four days of development are of interest and should be predicted accurately. The storm positions can be characterized by the points of maximal vorticity. For goal-oriented error estimation as presented in Chapter 3, goal functionals that are three-times differentiable are required. Since the characterization of the storm position in terms of the region of maximal vorticity does not fulfill the necessary regularity, smooth functionals that are correlated to the storm positions are introduced in the following.

5.3.1 Scenario 1: Integral of Vorticity over Fixed Region

For the first investigation, the position of only one of the storms after 96 hours is chosen to be the quantity of interest. Since the two storms are in interaction during the initial phase, the second storm has also great influence. One question to be addressed is to what extent this influence will be accounted for by the adaptive method and the resulting optimized meshes.

The storm that has final position on the left side should be of interest. The goal functional is defined as vorticity, integrated over that storm's core after 96 hours of development. The region that defines the core is approximated by a circle around the storm center $Pos_{fix} = (-1043.678\,\text{km}, 153.365\,\text{km})$ with radius of $r_{fix} = 93\,\text{km}$. These two parameters Pos_{fix} and r_{fix} are known a priori (determined from high-resolution reference simulations). In terms of the indicator function $\mathbf{1}_{V,fix} : \Omega \to \{0, 1\}$

$$\mathbf{1}_{V,fix}(x) := \begin{cases} 1, & \text{if } \|x - Pos_{fix}\|_{l^2} \leq r_{fix} \\ 0, & \text{else,} \end{cases}$$

the corresponding goal functional is defined by

$$J_{V,fix}(v) := \int_\Omega \mathbf{1}_{V,fix}(x)\, \nabla \times v(x, T)\, dx.$$

At the radius r_{fix}, the vorticity is approximately 50% lower than at the center and the vorticity gradient is strong. Therefore, small changes of the storm position have strong influence on the vorticity integral given by $J_{V,fix}$. For this goal functional, the reference value is

$$J_{V,fix}(v) \approx J_{V,fix}^{(ref)} := 14.486\,\mathrm{k}m^2/\mathrm{s}.$$

It should be noted that this goal functional is defined in terms of the two parameters Pos_{fix} and r_{fix} that were obtained from the reference solution. Certainly, such parameters are not known in realistic setups.

5.3.2 Scenario 2: Integral of Vorticity over High Vorticity Region

For this investigation, the final positions of both storms is chosen as the quantity of interest. The goal functional is defined as vorticity integral over both storm cores. In contrast to the previously defined goal functional, the storm cores are not given a priori but are characterized by regions in which vorticity is higher than 50% of the maximum vorticity. These regions are characterized in terms of the indicator function $\mathbf{1}_V : \Omega \to \{0,1\}$

$$\mathbf{1}_V(x) := \begin{cases} 1, & \text{if } \nabla \times \bar{v}(x) \geq 0.5 \cdot \max_{x\in\Omega}\{\nabla \times \bar{v}(x)\} \\ 0, & \text{else,} \end{cases}$$

and the goal functional is defined as

$$J_V(v) := \int_\Omega \mathbf{1}_V(x)\, \nabla \times v(x,T)\, dx.$$

Here, $\bar{v} : \Omega \to \mathbb{R}^2$ denotes some approximation of the velocity field at final time, i.e. $\bar{v}(x) \approx v(T,x)$ for each $x \in \Omega$. It should be stressed that the indicator function $\mathbf{1}_V$ is defined in terms of $\bar{v}$ which is treated as a constant when differentiating J_V. Thus, the influence of perturbations with respect to the change of vorticity within the fixed region can be measured. For this goal functional, the corresponding reference value is

$$J_V(v) \approx J_V^{(ref)} := 30.740\,\mathrm{k}m^2/\mathrm{s}.$$

5.3.3 Scenario 3: Integral of Energy over High Energy Region

The next goal functional includes the intensity of the winds by measuring the kinetic energy. Again, the final positions of both storms are of interest. The functional is defined as kinetic energy at final time, integrated over regions where the energy is higher than 90% of its maximum value close to the storms:

$$J_E(v) := \int_\Omega \mathbf{1}_E(x)\, v(x,T) \cdot v(x,T)\, dx.$$

The spatial region is characterized by the indicator function $\mathbf{1}_E : \Omega \to \{0,1\}$

$$\mathbf{1}_E(x) := \begin{cases} 1, & \text{if } \bar{v}(x,T) \cdot \bar{v}(x,T) \geq 0.9 \cdot \max_{x\in\Omega}\{\bar{v}(x,T) \cdot \bar{v}(x,T)\} \\ 0, & \text{else,} \end{cases}$$

where again $\bar{v} : \Omega \to \mathbb{R}^2$ denotes some approximation of the velocity field at final time. For this goal functional, the corresponding reference value is

$$J_E(v) \approx J_E^{(ref)} := 41.614\,\mathrm{k}m^4/s^2.$$

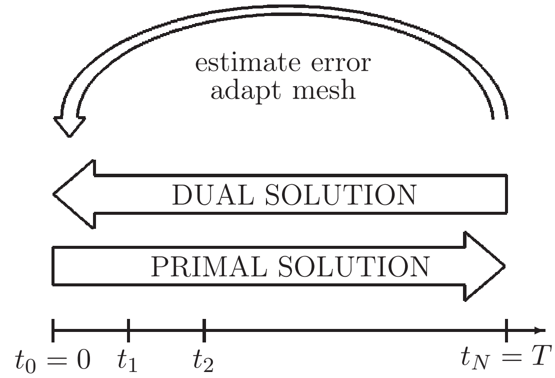

Figure 5.4: Adaptation cycle of the DWR method for time-dependent problems: Solution of the primal and dual problems, estimation of the error and mesh optimization.

5.4 Adaptive Method

Although time-dependent problems are covered in the general framework of the DWR method, its application to such problems can be challenging. In each adaptation cycle of the DWR method, the primal and dual solutions must be calculated. Further, higher-order approximations must be determined with respect to the temporal and spatial dimension. This is followed by the evaluation of the error estimator and the error indicators that control the subsequent mesh adaptation step. Since the dual problem is posed backward in time and depends on the primal solution (in case of nonlinear problems), the dual problem can be formulated and solved not until the primal problem has been solved, see Figure 5.4.

For the chosen discretization, the error estimators for Petrov-Galerkin methods described in Section 3.2 are appropriate. The error contributions corresponding to the space and time discretization are quantified separately as described in Section 3.2.2:

$$J(u) - J(u_{\tau h}) \approx E^{(time)}(u_{\tau h}) + E^{(space)}(u_{\tau h}). \tag{5.6}$$

Before the precise definition of the estimators $E^{(time)}(u_{\tau h})$ and $E^{(space)}(u_{\tau h})$ is given, the related function spaces and aspects of higher-order interpolation are outlined. The primal solution of the continuous problem (2.11) is denoted by $u = (v_1, v_2, p)^T \in X \times M$. Here, u consists of the velocity component $v = (v_1, v_2)^T$ and the pressure component p. The solution of the dual problem (3.50) is denoted by $z = (z_1, z_2, q)^T \in X \times M$. The test functions for both problems are denoted by $Y \times M$. The function spaces X, Y and M are defined as for the variational problems (2.11) and (3.50).

Approximate solutions for these two problems are calculated based on conforming finite dimensional subspaces $X_{\tau h} \subseteq X$, $Y_{\tau h} \subseteq Y$ and $M_{\tau h} \subseteq M$. The discrete spaces corresponding to the space-time discretization described in Section 5.2 is given in the following. The short notation $\mathbb{P}_i^{[c/dc]}(A)$ denotes the space of A-valued functions that are piecewise polynomials of order i. The superscript c or dc defines whether the function is globally continuous or not. The spaces have the following structure:

- $X_{\tau h} = \mathbb{P}_1^c(V_h)$, i.e. $X_{\tau h}$ consists of piecewise linear, V_h-valued functions, globally continuous: discrete space of trial functions for velocity

- $Y_{\tau h} = \mathbb{P}_0^{dc}(V_h)$, i.e. $Y_{\tau h}$ consists of piecewise constant, V_h-valued functions: discrete space of test functions for velocity
- $M_{\tau h} = \mathbb{P}_0^{dc}(Q_h)$, i.e. $M_{\tau h}$ consists of piecewise constant, Q_h-valued functions: discrete space of test and trial functions for pressure.

$V_h \times Q_h$ represents the finite element space spanned by Taylor-Hood elements $\mathcal{Q}_2/\mathcal{Q}_1$. For the estimation of the error related to the time-discretization, the following discrete spaces are introduced additionally:

- $X_\tau = \mathbb{P}_1^c(\hat{V}_h)$: time-discrete space of trial functions for velocity
- $Y_\tau = \mathbb{P}_0^{dc}(\hat{V}_h)$: time-discrete space of test functions for velocity
- $M_\tau = \mathbb{P}_0^{dc}(\hat{Q}_h)$: time-discrete space of test and trial functions for pressure.

The space $\hat{V}_h \times \hat{Q}_h$ corresponds to the finite element space spanned by higher-order Taylor-Hood elements $\mathcal{Q}_4/\mathcal{Q}_2$. The combination of $\mathcal{Q}_2/\mathcal{Q}_1$ and $\mathcal{Q}_4/\mathcal{Q}_2$ allows the efficient calculation of spatial higher-order interpolations as described in Section 3.2.1.3. The corresponding interpolation operator is denoted by

$$\hat{I}_{2h} : (V_h \times Q_h) \to (\hat{V}_h \times \hat{Q}_h).$$

The temporal higher-order interpolation operator is denoted by

$$\hat{I}_\tau : (X \times M) \to (X_\tau \times M_\tau),$$

and is defined such that the velocity components remain unchanged, only the pressure component (piecewise constant) is interpolated into the space of piecewise linear functions as given in equation (3.29). Note that all spaces are conformingly defined, i.e. $X_{\tau h} \subseteq X_\tau \subseteq X$, $Y_{\tau h} \subseteq Y_\tau \subseteq Y$ and $M_{\tau h} \subseteq M_\tau \subseteq M$.

After these notations, the a posteriori error estimators in (5.6) can be stated. Let $u_{\tau h} \in X_{\tau h} \times M_{\tau h}$ and $z_{\tau h} \in X_{\tau h} \times M_{\tau h}$ denote the discrete solution of the primal and dual problems. Further let the time-discrete solutions $\hat{u}_\tau$ and $\hat{z}_\tau$ be defined in terms of higher-order interpolation:

$$\hat{z}_\tau := \hat{I}_\tau(\hat{I}_{2h}(z_{\tau h})), \quad \hat{u}_\tau := \hat{I}_\tau(\hat{I}_{2h}(u_{\tau h})).$$

By equation (3.38), the error related to the time-discretization can be characterized by:

$$E^{(time)}(u_{\tau h}) = \frac{1}{2}\left(\rho(u_{\tau h})(\hat{z} + \hat{z}_\tau - I_\tau(\hat{z} + \hat{z}_\tau)) + \rho^*_{u_{\tau h}}(z_{h\tau})(\hat{u} - \hat{u}_\tau - I_\tau(\hat{u} - \hat{u}_\tau)\right).$$

Let the approximations of the exact solutions be defined by $\hat{u} := \hat{u}_\tau$ and $\hat{z} := \hat{z}_\tau$. Then the error characterization reduces to (see Remark 10):

$$E^{(time)}(u_{\tau h}) = \rho(u_{\tau h})(\hat{z}_\tau - I_\tau(\hat{z}_\tau)). \tag{5.7}$$

The estimator for the error contribution related to the space-discretization has the form:

$$\begin{aligned} E^{(space)}(u_{\tau h}) &= \frac{1}{2}\Big(\rho(u_{\tau h})(\hat{z}_\tau + z_{\tau h} - I_h(\hat{z}_\tau + z_{\tau h})) \\ &\quad +\rho^*_{u_{\tau h}}(z_{\tau h})(\hat{u}_\tau - u_{\tau h} - I_h(\hat{u}_\tau - u_{\tau h}))\Big). \end{aligned} \tag{5.8}$$

For the goal functionals J_V and J_E, the velocity field $\bar{v}$ must be defined additionally. In the ith adaptation cycle of the DWR method, first the primal problem is solved for the complete time interval. The velocity of the resulting solution, denoted by $v^{(i)}$, can be used to define the needed approximation, i.e. $\bar{v}(x) := v^{(i)}(T, x)$ for $x \in \Omega$.

For the a posteriori error characterizations (5.7) and (5.8), corresponding error indicators can be derived as described in Section 3.2.2. Based on these temporal and spatial indicators, the adaptation of the space-time mesh can be guided. Optimal meshes should have approximately an equal distribution of the error over the cells and further consist of a fixed number of total cells. The space-time meshes used for the numerical experiments have a further constraint: The spatial structure given by a possibly optimized mesh is kept constant in time. A partitioning of the time-interval defines the temporal structure of the space-time mesh. On such meshes, the discrete divergence-free condition and the global continuity of the discrete velocity field can be guaranteed at the same time. The latter is needed for the conformity of the discrete spaces. If the spatial mesh would be adapted within the time interval, either the continuity of the solution, or the divergence-free condition in the discrete sense, given in equation (2.38), would be violated. In the following, two mesh adaptation strategies are presented that are used for the numerical experiments discussed in Section 5.5.

5.4.1 Adaptation of the Spatial Mesh

The spatial discretization is based on meshes consisting of quadrilaterals. For such meshes, several constraints exist for mesh adaptation, as already mentioned in Section 2.4.2. Beside the 1-irregularity condition and the patch-structure (required for efficient higher-order interpolation), the space-periodicity of the scenario necessitates these constraints also to be fulfilled with respect to the neighborship relations over the periodic boundaries.

Based on the reduced error indicators introduced in equation (3.41), the spatial mesh adaptation can be controlled. To this end, strategies can be employed that are typically used for stationary problems, e.g. the error-balancing strategy, fixed-error-reduction or fixed-rate strategy [2]. Such methods aim to adapt the mesh toward an equal distribution of the error over the cells, i.e. cells with large error indication should be refined and cells with small error indication may be coarsened. To compare different adaptive methods based on several goal functionals, a mesh refinement strategy that leads to meshes consisting of a user-defined number of cells would be useful. The selection of cells that should be refined or coarsened towards a mesh with $N_{space}^{(\mathrm{opt})}$ cells is non-trivial, due to the aforementioned mesh constraints. On the one hand, each refined cell can lead to a plurality of further cells that also must be refined, on the other hand, cells that are marked to be coarsened will only be coarsened if all involved cells are also marked. Therefore, the following adaptation strategy decouples the steps of coarsening and refinement, to better control the adaptation procedure toward a mesh with $N_{space}^{(\mathrm{opt})}$ cells.

In the ith adaptation cycle of the DWR method, let the corresponding mesh consist of N_{space}^{i} cells. For the construction of the optimal mesh of the following adaptation cycle, the desired number of cells is defined by

$$N_{space}^{(\mathrm{opt}),i+1} := N_{space}^{i} + k(N_{space}^{(\mathrm{opt})} - N_{space}^{i}),$$

with a damping parameter $k \in (0,1)$. To mark cells that should be coarsened or refined, it is assumed that refining a cell into four smaller cells (in the case of quadrilaterals) is related to an error reduction by a factor of 2^{α}, where $\alpha > 0$ denotes the order parameter. A cell is marked to be coarsened, if its error indication is smaller than the coarsening bound

$$B_c := \left(\frac{1}{2}\right)^{\alpha+2} \eta_{avg}, \quad \eta_{avg} := \frac{1}{N_{space}^{(\mathrm{opt}),i+1}} \sum_{j=1}^{N_{space}^{i}} \eta_j^{(space)}.$$

The factor $\left(\frac{1}{2}\right)^{\alpha}$ represents effects of the error reduction in case of refinement and the remaining factor of $\left(\frac{1}{2}\right)^{2}$ accounts for the increased number of cells (one cell is refined to four cells). Hence, only cells are marked to be coarsened, if the coarsening is assumed to lead to an error of η_{avg} at most. Then the coarsening step can be carried out and leads to a mesh with $\bar{N}_{space}^{(\mathrm{opt}),i+1}$ cells.

In the next phase, cells with the largest error indication should be refined, and the resulting mesh should have approximately $N_{space}^{(\mathrm{opt}),i+1}$ cells. Since the refinement of one cell can cause the refinement of several further cells, an iterative approach is appropriate. The number of cells that should be refined is initialized with a small value, e.g. 10% of the initial difference $\max\{0, N_{space}^{(\mathrm{opt}),i+1} - \bar{N}_{space}^{(\mathrm{opt}),i+1}\}$, and is iteratively increased until the number of cells in the accordingly refined meshes matches the desired number of $N_{space}^{(\mathrm{opt}),i+1}$ up to a tolerance factor p. Only cells may be refined, that already existed on the mesh, based on which the error indicators where calculated (i.e. no recently coarsened or refined cells). The resulting mesh is accepted for the next adaptation cycle of the DWR method.

For the numerical simulations presented in Section 5.5, the order parameter is set to $\alpha = 2$, the damping parameter is set to $k = 0.7$ and the tolerance factor is set to $p = 0.07$. In each adaptation cycle of the DWR method, the primal and dual problems must be solved and the error must be estimated. Hence, the related computational cost is much higher compared to the iterative mesh adaptation procedure described before.

5.4.2 Adaptation of the Temporal Mesh

In contrast to the previous section, no comparable restrictions exist for the temporal mesh adaptation due to the one-dimensional structure of the domain. A partitioning is optimal if it consists of a user-defined number of sub-intervals and the corresponding error is distributed equally over these. Reduced error indicators can be derived from the error characterization (5.7) as described in Section 3.2.2:

$$\eta_i^{(time)} := \max_{K\in\mathcal{T}_h(i)} \eta_{iK}^{(time)}.$$

For a desired number of time intervals $N_{time}^{(\mathrm{opt})}$, the time step sizes should be determined such that the error indicators corresponding to each time-interval (t_{i-1}, t_i) are approximately identical:

$$\eta_i^{(time)} \approx \eta_j^{(time)} \quad \forall i, j \in \{1, \dots, N_{time}^{(\mathrm{opt})}\}.$$

Optimal partitionings of the interval $[0, T]$ are be constructed iteratively. In the kth iteration of the DWR method, the reduced temporal error indicators for each of the N_{time}^{k} time intervals on the current temporal mesh are given. In the following, the relation

$$\eta_i^{(time)} = C_i \cdot (\Delta t_i)^{\beta}, \quad i \in \{1, \dots, N_{time}^{k}\}, \tag{5.9}$$

between $\eta_i^{(time)}$ and corresponding time step size $\Delta t_i = t_i - t_{i-1}$ is assumed. The parameter $\beta > 0$ describing the order is constant over the complete time interval $[0, T]$. The following real-valued, piecewise constant functions D and E are introduced:

$$D(t)_{|(t_{i-1},t_i]} := \Delta t_i, \quad E(t)_{|(t_{i-1},t_i]} := \eta_i^{(time)}, \quad t \in (t_{i-1}, t_i],$$

for any $i \in \{1, \dots, N_{time}^{k}\}$. Further, by relation (5.9), a function C can be defined by

$$C(t) := \frac{E(t)}{D(t)^{\beta}}, \quad t \in (0, T]. \tag{5.10}$$

The optimality condition of the partitioning

$$N_{time}^{k+1} = N_{time}^{(\mathrm{opt})}, \tag{5.11}$$

$$\eta_i^{(time)} = \eta_j^{(time)} \quad \forall i, j \in \{1, \dots, N_{time}^{(\mathrm{opt})}\}. \tag{5.12}$$

can also be stated in terms of the functions $D^{(\mathrm{opt})}$ and $E^{(\mathrm{opt})}$ that describe the optimal partitioning:

$$\int_0^T \frac{1}{D^{(\mathrm{opt})}(t)}\, dt = N_{time}^{(\mathrm{opt})}, \tag{5.13}$$

$$E^{(\mathrm{opt})}(t) \equiv \bar{E}, \tag{5.14}$$

for some $\bar{E} \in \mathbb{R}$. By (5.14) and (5.10), the optimal time step size function $D^{(\mathrm{opt})}$ must be proportional to $1/C(t)^{1/\beta}$. To obtain the desired number of sub-intervals in the new partitioning, condition (5.13) must be fulfilled, which yields

$$D^{(\mathrm{opt})}(t) := \frac{\bar{E}}{C(t)^{1/\beta}}, \quad \bar{E} := N_{time}^{(\mathrm{opt})} \cdot \left(\int_0^T \frac{1}{C(t)^{1/\beta}}\, dt\right)^{-1}.$$

Then, the optimized partitioning can be defined successively in terms of function $D^{(\mathrm{opt})}$: Let $t_0 := 0$ and for each $i \in \{1, \dots, N_{time}^{(\mathrm{opt})}\}$ let the point in time t_i be defined such that

$$\int_{t_{i-1}}^{t_i} D^{(\mathrm{opt})}(t)\, dt = 1.$$

The resulting time increments are $\Delta t_i^{(\mathrm{opt})} := t_i - t_{i-1}$. The parameter β depends on the error measure, i.e. on the goal functional J. Approximations of β can be determined via series of numerical simulations on successively refined, uniform partitions of the time interval. If the parameter is chosen too large, the mesh adaptation process of the temporal discretization is damped.

For the numerical simulations shown in the following, the order parameter was set to $\beta = 3$. The partitioning after one or two adaptation cycles had the correct number of time steps and the corresponding error indicators were uniformly distributed.

5.5 Numerical Results

In the following, numerical simulations for the scenario of two interacting TCs are presented that were calculated using the the multi-purpose finite element library **HiFlow³** [28]. Since the exact solution is not known for this scenario, a reference solution based on a spatial mesh with 1,327,104 degrees of freedom (DOFs) (approx. cell diameter of 10 km) and 1,152 time steps was calculated. For the error analysis, the resulting reference solution υ and corresponding storm position Pos_{fix} at final time is employed to measure the different error quantities. As in Chapter 4, the efficiency index

$$I_{\text{eff}} := \left| \frac{E(\upsilon_{\tau h})}{J(\upsilon) - J(\upsilon_{\tau h})} \right| , \tag{5.15}$$

is introduced to quantify the relation between error estimates, denoted by $E(\upsilon_{\tau h})$, and true error for different goal functionals J. The first investigations are related to the adaptation of the spatial mesh based on a uniform partitioning of the time interval with sufficient small time steps of 300 s. The impact of the spatial mesh resolution to track prediction can be seen in Figure 5.7. On uniform meshes with less than 50,000 degrees of freedom, the storm position error is about 10^3 km at final time. This indicates a merger of the two storms, caused by too coarse mesh resolution (physical parameters are unchanged).

In the following, the iterative construction of an optimal spatial mesh is exemplified for the goal functional J_V. Figure 5.5 illustrates the initial uniform mesh with 4,096 cells (36,864 DOFs), the successive meshes obtained during the adaptation cycles of the DWR method and, finally, the optimal mesh with 5.968 cells (55,032 DOFs) that fulfills the optimality conditions given by the mesh adaptation strategy. On the initial mesh, the two storms merge due to the coarse spatial resolution. Hence, the dual problem is formulated based on a strongly perturbed primal solution. The corresponding error indicators emphasize the region at the domain's center where the two storms merge. Consequently, high resolution is confined to this region (see second mesh in Figure 5.5). Since the initial interaction phase is better resolved on this mesh, the storm tracks can be determined qualitatively correct. In the following adaptation cycles, the primal and dual solutions are more and more accurate and lead to better sensitivity information, improved error indicators and more economical meshes.

Figure 5.6 shows the dual solution corresponding to the goal functional $J_{V,fix}$ calculated on an optimized mesh with about 120,000 DOFs. At initial time, the

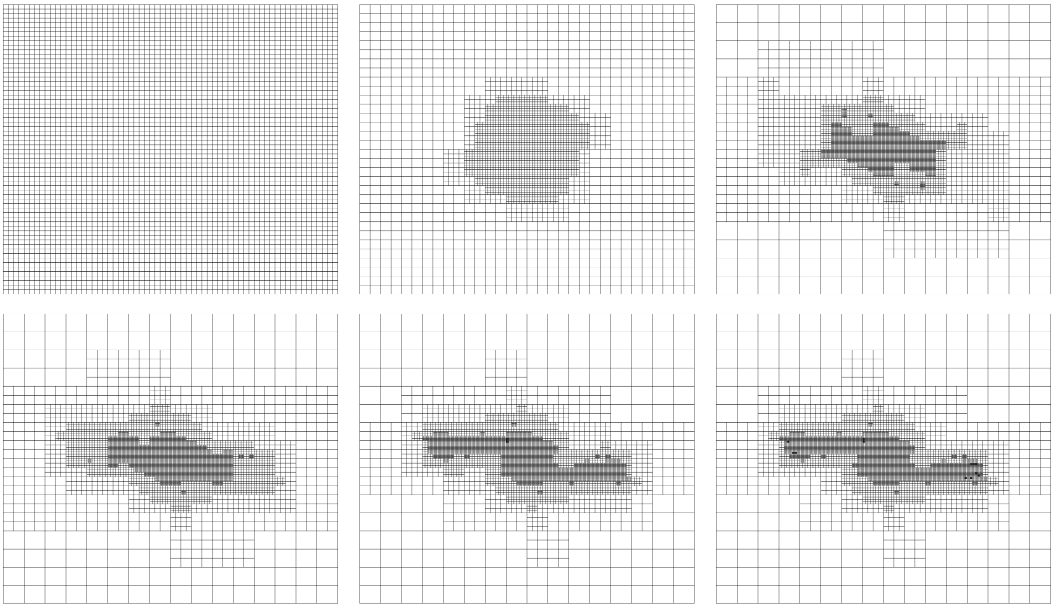

Figure 5.5: Sequence of meshes corresponding to the adaptation cycles of the DWR method for goal functional J_V for construction of an optimal mesh with about 6,000 cells.

sensitive regions are almost symmetrically distributed and surround the regions of the initial positions of the two vortices. At this stage, the vortices are closely located and the subsequent storm tracks are significantly impacted by their mutual interaction. By the definition of $J_{V,fix}$, the position of the storm that is located on the left at final time, is of interest, cf. the storm tracks in Figure 5.2. Although only one of the two storms is directly accounted for by the definition of the goal functional, the sensitivity of both storms is high. It can be seen that the optimized mesh has high resolution at the region where both storms are located at these first hours of simulation. After 32 hours, the tendency of the sensitive regions to the storm on the left can clearly be seen. After 96 hours, these congregate at the outside radius of the circle described by the indicator function $\mathbf{1}_{V,fix}$. The track of the second storm is highly resolved as long as its influence on the track of the first storm is strong. In Figure 5.7, the relative error in the goal functional

$$|J_{V,fix}^{(ref)} - J_{V,fix}(\upsilon_{\tau h})|/J_{V,fix}^{(ref)},$$

and corresponding estimated error quantities based on uniform and adapted meshes are plotted. The estimated and true error in the goal functional show good agreement, especially on meshes with more than 30,000 DOFs. On the coarsest grids, the information used by the error estimator is of lower quality. On finer meshes, the efficiency indicators is close to one. The resulting errors on optimized meshes, are reduced by more than one order of magnitude compared to uniform meshes (with approximately the same number of unknowns). The position error after 96 hours is shown in Figure 5.12. Even on grids with less than 20,000 DOFs, the tracks can be predicted qualitatively correct (i.e. the storms diverge) with a final position error

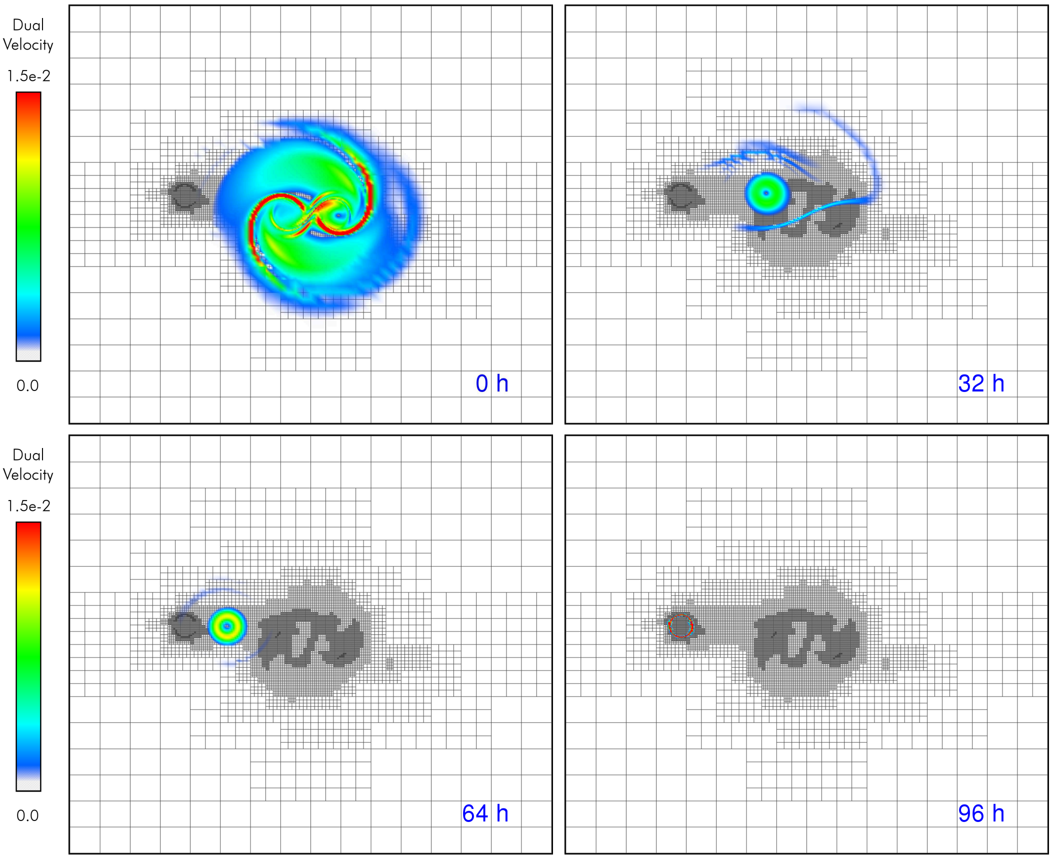

Figure 5.6: $J_{V,fix}$: Dual velocity on optimized mesh; 120,000 DOFs.

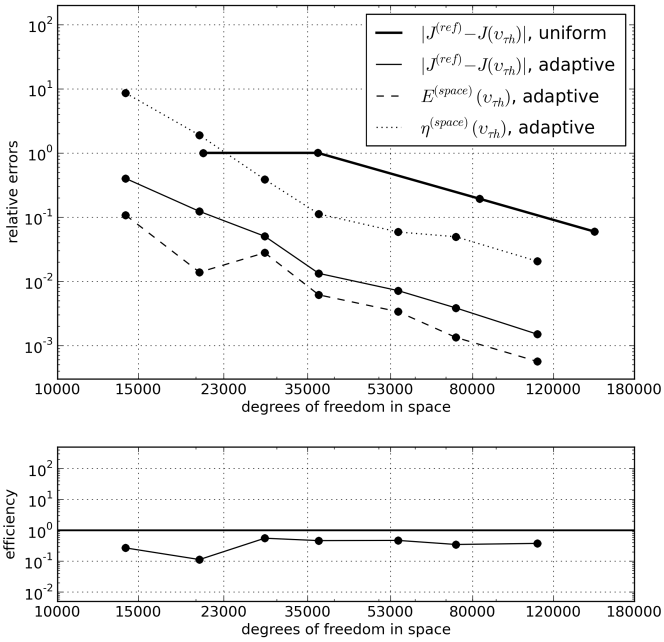

Figure 5.7: Relative error in $J_{V,fix}$ and efficiency index.

below 100 km. The first mesh with final position error of less than 10 km has about 30,000 DOFs.

The second goal functional J_V measures the vorticity close to the final position of both storms. The dual solution corresponding to $J_{V,fix}$ represents the sensitivity of one of the vortices only. For J_V, the mutual influence of the two storms is the symmetric superposition of the respective effects. Figure 5.8 shows the dual solution for different points in time and an optimized mesh with approximately 120,000 DOFs. The mesh has symmetric structure, since the primal problem as well as the goal functional is symmetrical. On optimized meshes, J_V can be determined more accurately compared to uniform meshes with the same number of unknowns and leads to a reduction of the relative errors in J_V by one order of magnitude, in average, see Figure 5.9. Compared to the previously investigated goal functional $J_{V,fix}$, the efficiency is declined. However, the adaptive meshes lead to position errors that are significantly reduced, compared to uniform meshes, see Figure 5.12.

The dual solution corresponding to the energy-based goal functional J_E is shown in Figure 5.10. Sensitive regions at the initial state are surrounding both initial locations of the two storms. In the course of time, these zones are expanding and finally focus at the two regions of highest kinetic energy of the primal solution at final time. At that stage, the vortex cores themselves are not included in the highlighted regions. Due to the propagation of the storms the zones of the highest velocity and kinetic energy are located to the right of the storm tracks. Also for this goal functional, adapted meshes lead to much better approximations of the reference value corresponding to the goal functional, cf. Figure 5.11. On the finest meshes, the error is reduced approximately by one order of magnitude and leads to very accurate track predictions, see Figure 5.12.

The goal functionals J_V and J_E are defined in terms of the maximum vorticity and maximum energy values of the velocity field, respectively. During the adaptation cycles of the DWR method, these values are determined based on the approximate solutions calculated on adapted meshes. Especially the maximum vorticity values vary strongly on these meshes, see left panel of Figure 5.12 showing the ratio of the maximal vorticity and maximal energy to the reference values, respectively. Therefore, the definitions of the goal functionals J_V and J_E are also changing in each adaptation cycle. In Figures 5.9 and 5.11, the error plots corresponding to $|J^{(ref)}(v) - J(v_{\tau h})|$ include these effects of varying definition of the goal functionals. The significance of the efficiency indicators is limited for these two goal functionals, since the estimated errors and the true errors correspond to different error norms for these goal functionals.

For the investigation of the position errors, only the upper left storm position at final time is considered. This is an adequate measure, since this vortex is marked in case of the goal functional $J_{V,fix}$ and the remaining goal functionals are treating both storms identically and lead to symmetrical meshes and tracks. The right panel of Figure 5.12 shows a comparison of the position errors based on uniform and adapted meshes for all considered goal functionals. Especially on coarser meshes, the vorticity type functionals $J_{V,fix}$ and J_V lead to better position forecasts. On meshes with more than 70,000 DOFs the goal functional J_E leads to the best predictions with an error of less than 1 km compared to the reference track which was calculated based on a uniform mesh with cell diameter of 10 km. The storm positions are

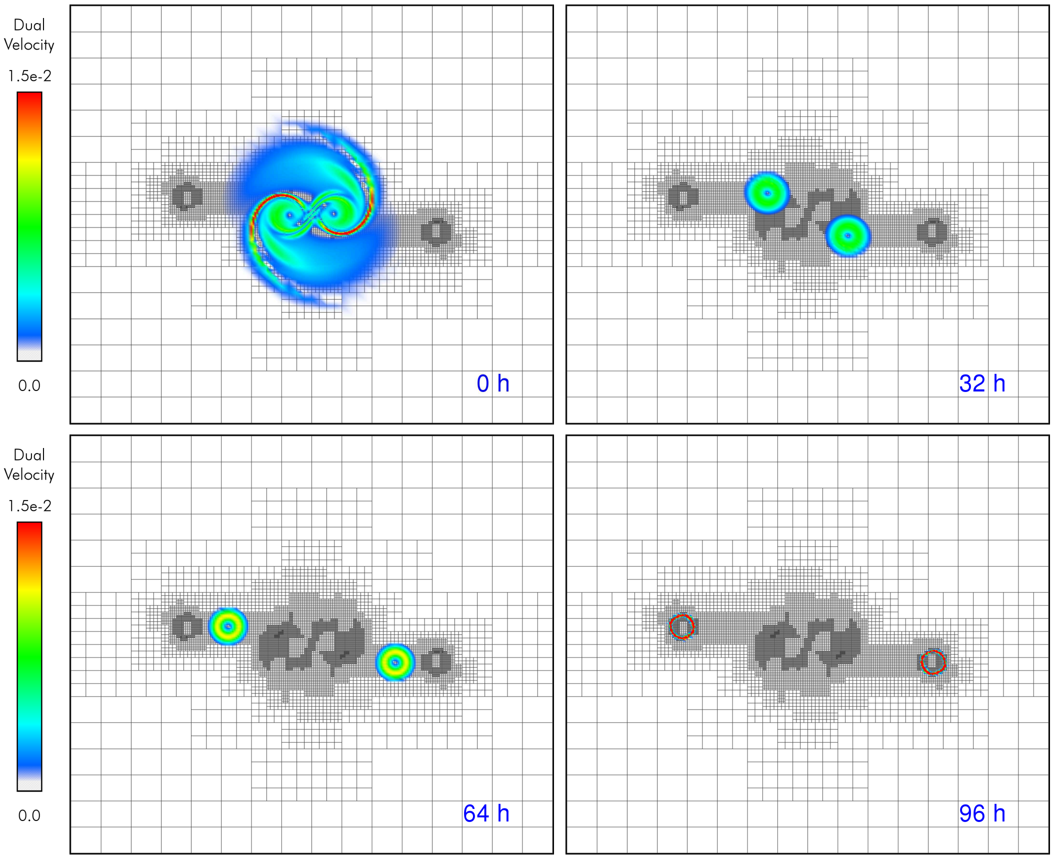

Figure 5.8: J_V: Dual velocity on optimized mesh; 120,000 DOFs.

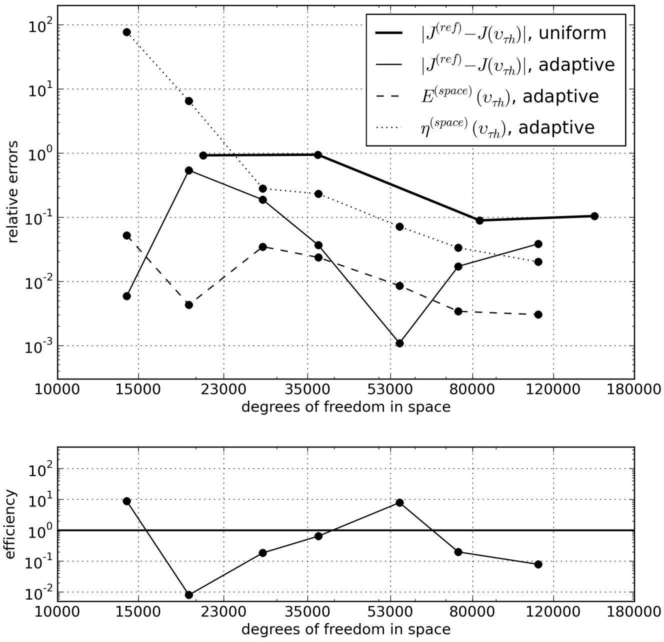

Figure 5.9: Relative error in J_V and efficiency index.

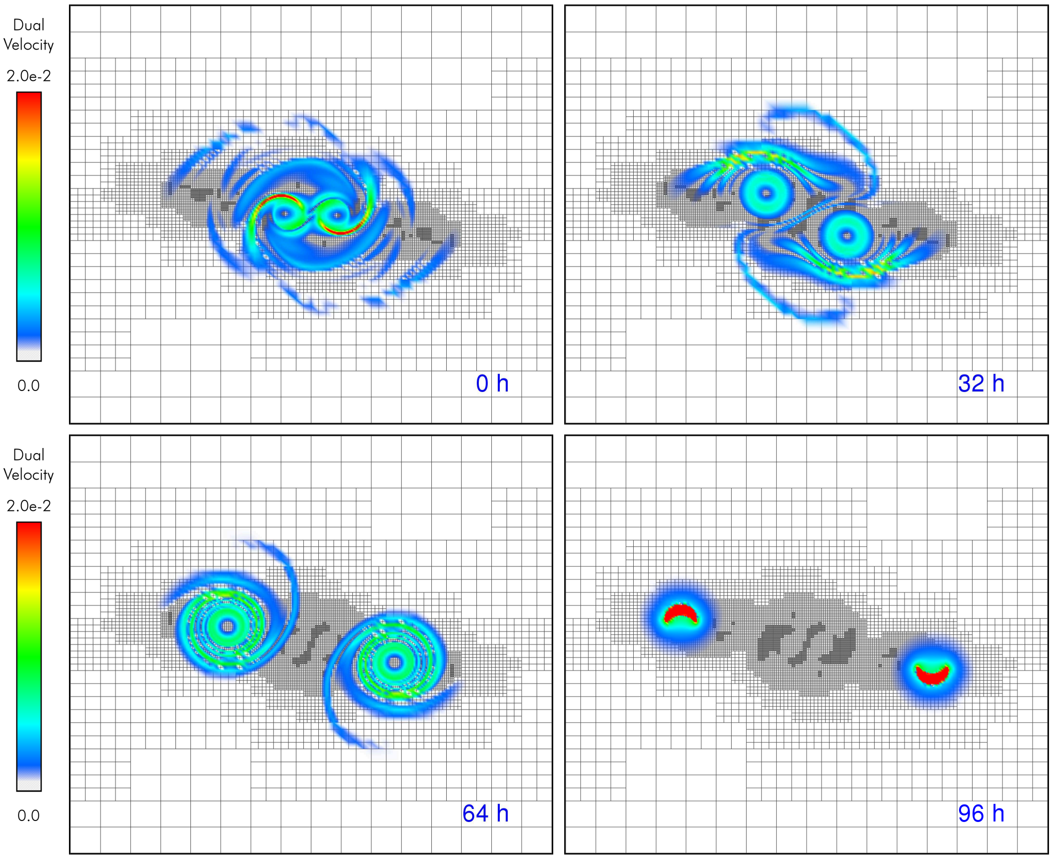

Figure 5.10: J_E: Dual velocity on optimized mesh; 120,000 DOFs.

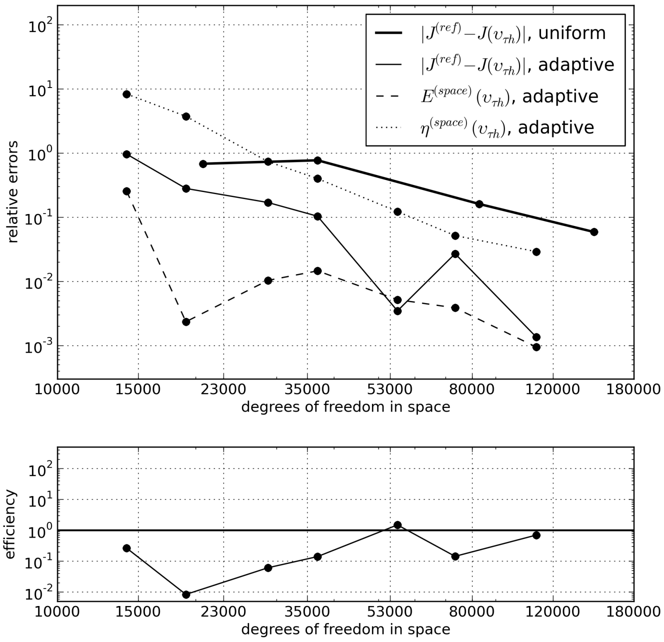

Figure 5.11: Relative error in J_E and efficiency index.

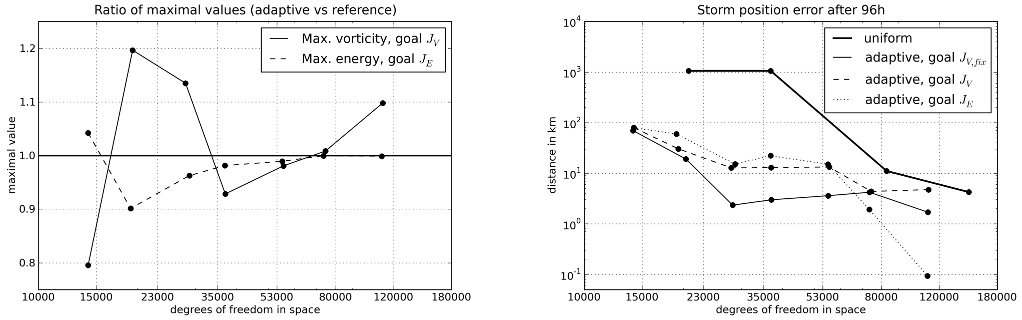

Figure 5.12: Left: Ratio of maximum vorticity and energy on adapted meshes to the reference values. Right: Position error on uniform and optimized grids.

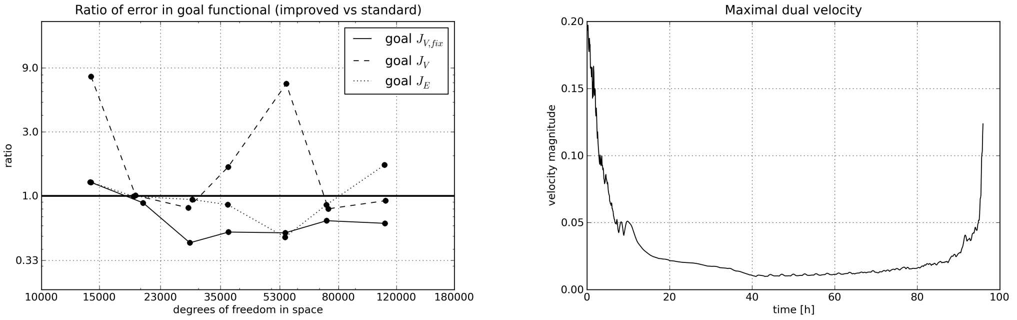

Figure 5.13: Left: Ratio between error in goal functional $J(v_{\tau h})$ and post-processed quantity $\tilde{J}(v_{\tau h})$. Right: Maximal value of dual velocity magnitude over the domain as function in time for goal functional $J_{V,fix}$.

characterized in sub-grid accuracy as the vorticity-weighted barycenter, i.e.

$$Pos(v) := \int_V x \cdot (\nabla \times v(T,x) - M)\, dx \cdot \left(\int_V (\nabla \times v(T,x) - M)\, dx \right)^{-1}.$$

Here, $V \subseteq \Omega$ denotes the region located closely to the upper left storm at final time, where vorticity values are greater than $M := 0.9 \cdot \max_{x \in V} \nabla \times v(T,x)$, i.e. 90% of the maximum vorticity at the storm center.

By means of the a posteriori error estimators, post-processed quantities of interest $\tilde{J}(v_{\tau h}) \approx J(v)$ can be determined as described in Section 3.2.3. The left panel of Figure 5.13 shows the ratio of the error in the post-processed goal value to the error in the standard approximation $J(v_{\tau h})$, i.e.

$$R := \frac{|J(v) - \tilde{J}(v_{\tau h})|}{|J(v) - J(v_{\tau h})|}.$$

In contrast to the stationary scenarios investigated in Chapter 4, no significant improvements by post-processing the quantity of interest can be noticed.

The optimization of the time-discretization based on temporal error indicators for the goal functional $J_{V,fix}$ is investigated in the following. To this end, an optimized

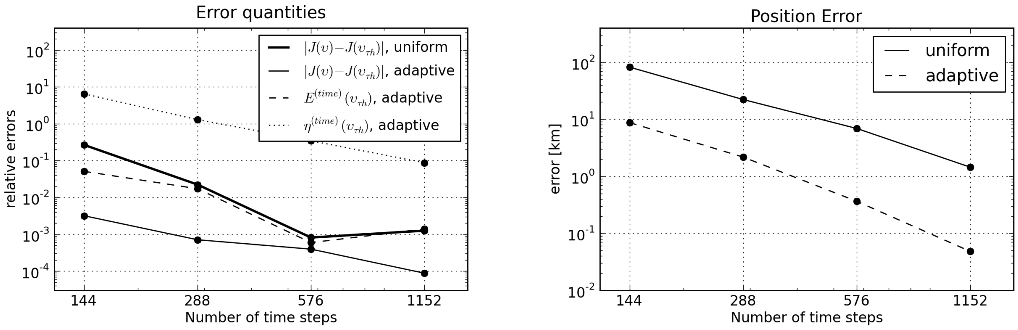

Figure 5.14: Relative error in goal functional $J_{V,fix}$ (left) and position error at final time (right) based on uniform and optimized partitioning of the time interval.

spatial mesh with 36,864 DOFs is considered. Figure 5.15 shows comparisons between optimized and uniform partitions of the time interval for different numbers of total time steps. The temporal error indicators for uniform partitions vary by several orders of magnitude within the time interval. Especially the early hours of the storm interaction and the final hours are related to large indicators. During the first hours, the separation distance between the two storms is still small. In this phase, the wind profiles and zones of increased vorticity of the two storms overlap, leading to an interaction of the two cyclones. At later times, the influence of the interaction becomes smaller and smaller. On the right panel of Figure 5.13, the maximum velocity magnitude of the dual solution is plotted as function in time. It can be seen that the velocity magnitude is increased during the first and last hours of the simulation. As the dual solution plays the role of the weighting of the primal problem's residual in the error characterizations, cf. equation (3.21), the resulting error indicators tend to be increased close to the initial time and close to the final time.

Based on the mesh adaptation strategy presented in Section 5.4.2, economical partitions can be determined. On the optimized partitions, the time increments for the first and last hours of the considered time horizon are very small, see right panels of Figure 5.15. In between, the time step sizes are up to a factor of 6 larger. Each sub-interval is related to a temporal error indicator with approximately the same value, see left panels of Figure 5.15. This indicates the optimality of the temporal mesh.

For the investigated scenario, the optimization of the partitioning based on the temporal error indicators, leads to remarkable improvements with respect to the different error measurements. For the error analysis, a reference solution calculated on a partitioning with 9,216 uniform time steps is employed. On adapted partitions, the error in the goal functional is reduced by approximately one order of magnitude compared to uniform partitions with the same number of sub-intervals (left panel of Figure 5.14). For example, on an optimized partition consisting of 288 time increments, the resulting error in the goal functional is smaller compared to a uniform partitioning consisting of 1,152 time increments. Additionally, the position error at final time is reduced significantly on optimized time-discretizations, see right panel

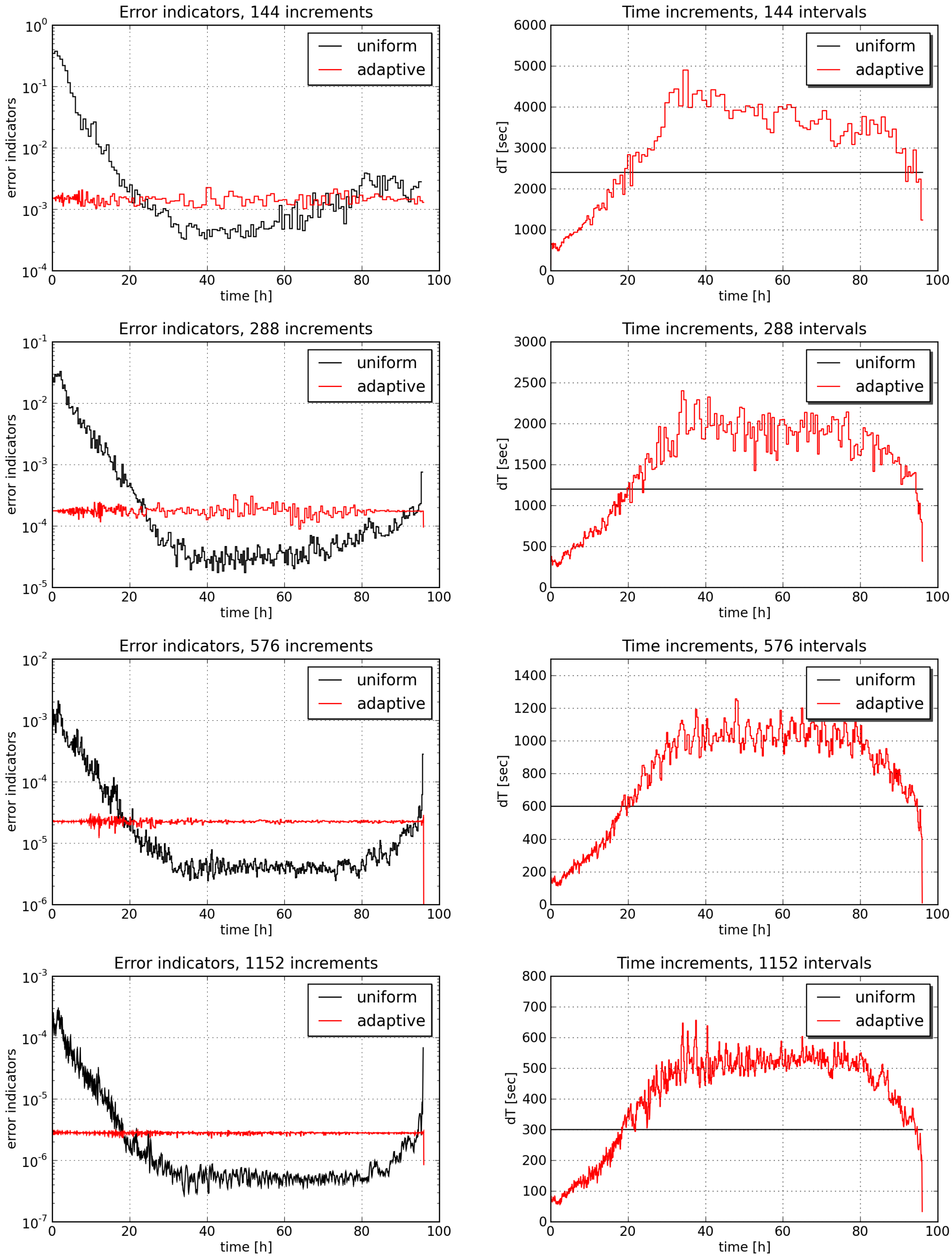

Figure 5.15: Temporal error indicators (left) and time step sizes (right) for uniform and adaptive partitions of the time interval.

of Figure 5.14.

5.6 Concluding Remarks

The chosen goal functionals could be verified to be adequate for the prediction of storm tracks. The position error could be reduced significantly based on adapted discretizations that were optimized to reduce the error in the goal functionals. Based on spatial mesh adaptation, the accuracy could be increase by about one order of magnitude. The construction of optimal partitions of the time interval leads to an additional improvement. The optimized partitions where characterized by an almost uniform distribution of the error indicators, independent of the total number of sub-intervals. The error in the goal functional as well as the position error of the storm could be reduced by approximately one order of magnitude compared to uniform partitions with the same number of time increments.

Furthermore, a more general property of goal-oriented methods could be noticed. The goal functional $J_{V,fix}$ lead to non-symmetric adapted meshes, although the underlying primal problem was symmetrically defined. In terms of the non-symmetric goal functional that accounted for one storm primarily, a better specialization of the meshes for the determination of this storm's position could be achieved, since large parts of the domain had only small influence to the quantity of interest. This depicts the principle potential of such methods to account for local features of the underlying problems in contrast to many alternative adaptive approaches that don't consider similar sensitivity information.

6 Discussion and Outlook

In this thesis, goal-oriented adaptive methods were further developed and applied to scenarios of large-scale atmospheric fluid flow. A new strategy for the approximation of the dual solution based on local Dirichlet problems and global defect correction was proposed. The corresponding a posteriori error estimators were compared to several alternative variants in a series of benchmark problems with known analytical solutions. Furthermore, an extension of goal-oriented error estimation for conforming discretizations of parabolic problems was developed in the context of Petrov-Galerkin methods. For a scenario of interacting tropical cyclones, economical meshes were constructed based on the developed adaptive techniques. The error of the predicted storm tracks could significantly be reduced.

These achievements suggest that such goal-oriented methods offer great potential for the modeling of tropical cyclone dynamics. The time-continuous discretizations based on the cGP(k) method lead to systems with smaller number of unknowns, compared to the discontinuous methods with same polynomial degree. In case of the NSE, a divergence-free condition must be fulfilled simultaneously to the global continuity. The space-time meshes considered in this work allowed only one spatial mesh during the complete time interval to satisfy both conditions. Without this limitation, even more economical discretizations can be expected. In this context, aspects of mesh adaptation in time should be subject of future work. Small discontinuities (e.g. defined in terms of the interpolation operator presented in Section 2.4.3) could be allowed in contrast to the global continuity condition. Alternatively, the divergence-free condition could be weakened in situations where the spatial mesh is adapted.

The discussed adaptive methods lead to economical meshes by means of an iterative procedure. The related overall effort can be quite high, since the primal and dual problems must be solved repeatedly on a series of adapted meshes. Especially for time-dependent problems, new ideas to decrease the related computational cost are needed. In this context, reduced sensitivity information that accounts only for local time horizons, as proposed in [13], could be sufficient for many applications and requires the solution of quasi-stationary dual problems, only. Furthermore, approaches of model reduction such as the proper orthogonal decomposition (POD) method offer great potential for massive decrease of the number of unknowns related to the discrete problems and should be investigated in the context of time-dependent problems.

More realistic models for numerical weather prediction require the consideration of many complex atmospheric processes, including solar radiation, moist processes, heat exchange, and multiple chemical reactions. In addition to the discussed mesh adaptation approach, such systems could take great advantage of goal-oriented model adaptation techniques as proposed in [7, 8]. This would enable the use of a hierarchy of physical models with varying complexity, whereas error estimators can determine which level of complexity is needed to guarantee good approximation of user-defined quantities of interest. Methods of simultaneous mesh and model adaptation combined with highly efficient techniques for the determination of the needed sensitivity information could lead to substantial progress in modeling such complex atmospheric phenomena.

7 Appendix

The following tabulars contain specific error quantities corresponding to numerical simulations of the scenarios presented in Chapter 4. For each error estimator variant and each scenario, the efficiency index, the estimated error $E(v_h)$, the true error in J and the error of the post-processed value $\tilde{J}(v_h)$, as defined in Section 3.2.3, is given for a sequence of uniform meshes.

Scenario 1: Point Value of Velocity

# DOFs	$\lvert J(u) - J(u_h)\rvert$	$\lvert E(u_h)\rvert$	I_{eff}	$\lvert J(u) - \tilde{J}(u_h)\rvert$
659	$4.84 \cdot 10^{-04}$	$2.78 \cdot 10^{-04}$	0.57	$2.06 \cdot 10^{-04}$
2467	$4.85 \cdot 10^{-05}$	$2.77 \cdot 10^{-05}$	0.57	$2.07 \cdot 10^{-05}$
9539	$4.28 \cdot 10^{-06}$	$2.51 \cdot 10^{-06}$	0.59	$1.76 \cdot 10^{-06}$
37507	$6.95 \cdot 10^{-07}$	$3.70 \cdot 10^{-07}$	0.53	$3.24 \cdot 10^{-07}$
148739	$4.94 \cdot 10^{-08}$	$2.91 \cdot 10^{-08}$	0.59	$2.03 \cdot 10^{-08}$

Table 7.1: $E_D^{(\text{anal.})}$, analytical solution of primal problem

# DOFs	$\lvert J(u) - J(u_h)\rvert$	$\lvert E(u_h)\rvert$	I_{eff}	$\lvert J(u) - \tilde{J}(u_h)\rvert$
659	$4.84 \cdot 10^{-04}$	$2.71 \cdot 10^{-04}$	0.56	$2.13 \cdot 10^{-04}$
2467	$4.85 \cdot 10^{-05}$	$2.67 \cdot 10^{-05}$	0.55	$2.18 \cdot 10^{-05}$
9539	$4.28 \cdot 10^{-06}$	$2.61 \cdot 10^{-06}$	0.61	$1.66 \cdot 10^{-06}$
37507	$6.95 \cdot 10^{-07}$	$3.67 \cdot 10^{-07}$	0.53	$3.27 \cdot 10^{-07}$
148739	$4.94 \cdot 10^{-08}$	$2.95 \cdot 10^{-08}$	0.60	$1.99 \cdot 10^{-08}$

Table 7.2: $E_P^{(\text{ho-fe})}$, higher-order finite element solution

# DOFs	$\lvert J(u) - J(u_h)\rvert$	$\lvert E(u_h)\rvert$	I_{eff}	$\lvert J(u) - \tilde{J}(u_h)\rvert$
659	$4.84 \cdot 10^{-04}$	$2.81 \cdot 10^{-04}$	0.58	$2.03 \cdot 10^{-04}$
2467	$4.85 \cdot 10^{-05}$	$2.73 \cdot 10^{-05}$	0.56	$2.12 \cdot 10^{-05}$
9539	$4.28 \cdot 10^{-06}$	$2.57 \cdot 10^{-06}$	0.60	$1.70 \cdot 10^{-06}$
37507	$6.95 \cdot 10^{-07}$	$3.70 \cdot 10^{-07}$	0.53	$3.25 \cdot 10^{-07}$
148739	$4.94 \cdot 10^{-08}$	$2.93 \cdot 10^{-08}$	0.59	$2.01 \cdot 10^{-08}$

Table 7.3: $E_{PD}^{(\text{ho-fe})}$, higher-order finite element solution

# DOFs	$\lvert J(u)-J(u_h)\rvert$	$\lvert E(u_h)\rvert$	I_{eff}	$\lvert J(u)-\tilde{J}(u_h)\rvert$
659	$4.84 \cdot 10^{-04}$	$4.61 \cdot 10^{-05}$	0.10	$4.38 \cdot 10^{-04}$
2467	$4.85 \cdot 10^{-05}$	$1.86 \cdot 10^{-05}$	0.38	$2.99 \cdot 10^{-05}$
9539	$4.28 \cdot 10^{-06}$	$2.87 \cdot 10^{-06}$	0.67	$7.15 \cdot 10^{-06}$
37507	$6.95 \cdot 10^{-07}$	$2.30 \cdot 10^{-07}$	0.33	$9.25 \cdot 10^{-07}$
148739	$4.94 \cdot 10^{-08}$	$4.26 \cdot 10^{-08}$	0.86	$9.20 \cdot 10^{-08}$

Table 7.4: $E_P^{(\text{ho-int})}$, higher-order interpolation

# DOFs	$\lvert J(u)-J(u_h)\rvert$	$\lvert E(u_h)\rvert$	I_{eff}	$\lvert J(u)-\tilde{J}(u_h)\rvert$
659	$4.84 \cdot 10^{-04}$	$1.82 \cdot 10^{-04}$	0.38	$3.02 \cdot 10^{-04}$
2467	$4.85 \cdot 10^{-05}$	$2.45 \cdot 10^{-05}$	0.51	$2.40 \cdot 10^{-05}$
9539	$4.28 \cdot 10^{-06}$	$2.25 \cdot 10^{-07}$	0.05	$4.50 \cdot 10^{-06}$
37507	$6.95 \cdot 10^{-07}$	$6.77 \cdot 10^{-08}$	0.10	$6.27 \cdot 10^{-07}$
148739	$4.94 \cdot 10^{-08}$	$6.88 \cdot 10^{-09}$	0.14	$5.63 \cdot 10^{-08}$

Table 7.5: $E_{PD}^{(\text{ho-int})}$, higher-order interpolation

# DOFs	$\lvert J(u)-J(u_h)\rvert$	$\lvert E(u_h)\rvert$	I_{eff}	$\lvert J(u)-\tilde{J}(u_h)\rvert$
659	$4.84 \cdot 10^{-04}$	$1.43 \cdot 10^{-04}$	0.29	$3.42 \cdot 10^{-04}$
2467	$4.85 \cdot 10^{-05}$	$1.47 \cdot 10^{-05}$	0.30	$3.38 \cdot 10^{-05}$
9539	$4.28 \cdot 10^{-06}$	$5.92 \cdot 10^{-07}$	0.14	$3.68 \cdot 10^{-06}$
37507	$6.95 \cdot 10^{-07}$	$1.79 \cdot 10^{-07}$	0.26	$5.16 \cdot 10^{-07}$
148739	$4.94 \cdot 10^{-08}$	$1.33 \cdot 10^{-08}$	0.27	$3.61 \cdot 10^{-08}$

Table 7.6: $E_P^{(\text{block},1)}$, block strategy, one update step, $\omega = 0.2$

# DOFs	$\lvert J(u)-J(u_h)\rvert$	$\lvert E(u_h)\rvert$	I_{eff}	$\lvert J(u)-\tilde{J}(u_h)\rvert$
659	$4.84 \cdot 10^{-04}$	$1.61 \cdot 10^{-04}$	0.33	$3.23 \cdot 10^{-04}$
2467	$4.85 \cdot 10^{-05}$	$1.65 \cdot 10^{-05}$	0.34	$3.20 \cdot 10^{-05}$
9539	$4.28 \cdot 10^{-06}$	$9.11 \cdot 10^{-07}$	0.21	$3.37 \cdot 10^{-06}$
37507	$6.95 \cdot 10^{-07}$	$1.82 \cdot 10^{-07}$	0.26	$5.13 \cdot 10^{-07}$
148739	$4.94 \cdot 10^{-08}$	$1.71 \cdot 10^{-08}$	0.35	$3.23 \cdot 10^{-08}$

Table 7.7: $E_P^{(\text{block},2)}$, block strategy, two update steps, $\omega = 0.2$

Scenario 2: Weighted Integral of Vorticity (I)

# DOFs	$\lvert J(u)-J(u_h)\rvert$	$\lvert E(u_h)\rvert$	I_{eff}	$\lvert J(u)-\tilde{J}(u_h)\rvert$
659	$3.16\cdot 10^{-04}$	$3.16\cdot 10^{-04}$	1.00	$5.68\cdot 10^{-08}$
2467	$1.95\cdot 10^{-05}$	$1.95\cdot 10^{-05}$	1.00	$7.67\cdot 10^{-10}$
9539	$1.22\cdot 10^{-06}$	$1.22\cdot 10^{-06}$	1.00	$1.38\cdot 10^{-11}$
37507	$7.61\cdot 10^{-08}$	$7.61\cdot 10^{-08}$	1.00	$2.39\cdot 10^{-12}$
148739	$4.75\cdot 10^{-09}$	$4.76\cdot 10^{-09}$	1.00	$2.10\cdot 10^{-12}$

Table 7.8: $E_D^{(\text{anal.})}$, analytical solution of primal problem

# DOFs	$\lvert J(u)-J(u_h)\rvert$	$\lvert E(u_h)\rvert$	I_{eff}	$\lvert J(u)-\tilde{J}(u_h)\rvert$
659	$3.16\cdot 10^{-04}$	$2.24\cdot 10^{-04}$	0.71	$9.25\cdot 10^{-05}$
2467	$1.95\cdot 10^{-05}$	$1.40\cdot 10^{-05}$	0.72	$5.53\cdot 10^{-06}$
9539	$1.22\cdot 10^{-06}$	$8.74\cdot 10^{-07}$	0.72	$3.44\cdot 10^{-07}$
37507	$7.61\cdot 10^{-08}$	$5.45\cdot 10^{-08}$	0.72	$2.16\cdot 10^{-08}$
148739	$4.75\cdot 10^{-09}$	$3.40\cdot 10^{-09}$	0.72	$1.35\cdot 10^{-09}$

Table 7.9: $E_P^{(\text{ho-fe})}$, higher-order finite element solution

# DOFs	$\lvert J(u)-J(u_h)\rvert$	$\lvert E(u_h)\rvert$	I_{eff}	$\lvert J(u)-\tilde{J}(u_h)\rvert$
659	$3.16\cdot 10^{-04}$	$2.85\cdot 10^{-04}$	0.90	$3.18\cdot 10^{-05}$
2467	$1.95\cdot 10^{-05}$	$1.77\cdot 10^{-05}$	0.91	$1.85\cdot 10^{-06}$
9539	$1.22\cdot 10^{-06}$	$1.10\cdot 10^{-06}$	0.91	$1.15\cdot 10^{-07}$
37507	$7.61\cdot 10^{-08}$	$6.89\cdot 10^{-08}$	0.91	$7.18\cdot 10^{-09}$
148739	$4.75\cdot 10^{-09}$	$4.31\cdot 10^{-09}$	0.91	$4.48\cdot 10^{-10}$

Table 7.10: $E_{PD}^{(\text{ho-fe})}$, higher-order finite element solution

# DOFs	$\lvert J(u)-J(u_h)\rvert$	$\lvert E(u_h)\rvert$	I_{eff}	$\lvert J(u)-\tilde{J}(u_h)\rvert$
659	$3.16\cdot 10^{-04}$	$1.89\cdot 10^{-04}$	0.60	$1.27\cdot 10^{-04}$
2467	$1.95\cdot 10^{-05}$	$1.34\cdot 10^{-05}$	0.68	$6.16\cdot 10^{-06}$
9539	$1.22\cdot 10^{-06}$	$8.66\cdot 10^{-07}$	0.71	$3.52\cdot 10^{-07}$
37507	$7.61\cdot 10^{-08}$	$5.45\cdot 10^{-08}$	0.72	$2.16\cdot 10^{-08}$
148739	$4.75\cdot 10^{-09}$	$3.41\cdot 10^{-09}$	0.72	$1.35\cdot 10^{-09}$

Table 7.11: $E_P^{(\text{ho-int})}$, higher-order interpolation

# DOFs	$\lvert J(u) - J(u_h)\rvert$	$\lvert E(u_h)\rvert$	I_{eff}	$\lvert J(u) - \tilde{J}(u_h)\rvert$
659	$3.16 \cdot 10^{-04}$	$2.61 \cdot 10^{-04}$	0.82	$5.57 \cdot 10^{-05}$
2467	$1.95 \cdot 10^{-05}$	$1.66 \cdot 10^{-05}$	0.85	$2.93 \cdot 10^{-06}$
9539	$1.22 \cdot 10^{-06}$	$1.04 \cdot 10^{-06}$	0.86	$1.74 \cdot 10^{-07}$
37507	$7.61 \cdot 10^{-08}$	$6.53 \cdot 10^{-08}$	0.86	$1.08 \cdot 10^{-08}$
148739	$4.75 \cdot 10^{-09}$	$4.08 \cdot 10^{-09}$	0.86	$6.72 \cdot 10^{-10}$

Table 7.12: $E_{PD}^{(\text{ho-int})}$, higher-order interpolation

# DOFs	$\lvert J(u) - J(u_h)\rvert$	$\lvert E(u_h)\rvert$	I_{eff}	$\lvert J(u) - \tilde{J}(u_h)\rvert$
659	$3.16 \cdot 10^{-04}$	$9.86 \cdot 10^{-05}$	0.31	$2.18 \cdot 10^{-04}$
2467	$1.95 \cdot 10^{-05}$	$6.19 \cdot 10^{-06}$	0.32	$1.34 \cdot 10^{-05}$
9539	$1.22 \cdot 10^{-06}$	$3.82 \cdot 10^{-07}$	0.31	$8.37 \cdot 10^{-07}$
37507	$7.61 \cdot 10^{-08}$	$2.36 \cdot 10^{-08}$	0.31	$5.25 \cdot 10^{-08}$
148739	$4.75 \cdot 10^{-09}$	$1.47 \cdot 10^{-09}$	0.31	$3.29 \cdot 10^{-09}$

Table 7.13: $E_P^{(\text{block},1)}$, block strategy, one update step, $\omega = 0.2$

# DOFs	$\lvert J(u) - J(u_h)\rvert$	$\lvert E(u_h)\rvert$	I_{eff}	$\lvert J(u) - \tilde{J}(u_h)\rvert$
659	$3.16 \cdot 10^{-04}$	$1.16 \cdot 10^{-04}$	0.37	$2.00 \cdot 10^{-04}$
2467	$1.95 \cdot 10^{-05}$	$7.14 \cdot 10^{-06}$	0.37	$1.24 \cdot 10^{-05}$
9539	$1.22 \cdot 10^{-06}$	$4.40 \cdot 10^{-07}$	0.36	$7.78 \cdot 10^{-07}$
37507	$7.61 \cdot 10^{-08}$	$2.73 \cdot 10^{-08}$	0.36	$4.88 \cdot 10^{-08}$
148739	$4.75 \cdot 10^{-09}$	$1.70 \cdot 10^{-09}$	0.36	$3.06 \cdot 10^{-09}$

Table 7.14: $E_P^{(\text{block},2)}$, block strategy, two update steps, $\omega = 0.2$

Scenario 3: Weighted Integral of Vorticity (II)

# DOFs	$\lvert J(u)-J(u_h)\rvert$	$\lvert E(u_h)\rvert$	I_{eff}	$\lvert J(u)-\tilde{J}(u_h)\rvert$
659	$2.44\cdot 10^{-05}$	$2.95\cdot 10^{-05}$	1.21	$5.03\cdot 10^{-06}$
2467	$2.39\cdot 10^{-06}$	$8.56\cdot 10^{-07}$	0.36	$3.24\cdot 10^{-06}$
9539	$1.33\cdot 10^{-07}$	$3.62\cdot 10^{-08}$	0.27	$9.70\cdot 10^{-08}$
37507	$3.07\cdot 10^{-09}$	$3.92\cdot 10^{-09}$	1.28	$8.47\cdot 10^{-10}$
148739	$9.07\cdot 10^{-11}$	$7.96\cdot 10^{-11}$	0.88	$1.11\cdot 10^{-11}$

Table 7.15: $E_D^{(\text{anal.})}$, analytical solution of primal problem

# DOFs	$\lvert J(u)-J(u_h)\rvert$	$\lvert E(u_h)\rvert$	I_{eff}	$\lvert J(u)-\tilde{J}(u_h)\rvert$
659	$2.44\cdot 10^{-05}$	$3.14\cdot 10^{-05}$	1.29	$7.01\cdot 10^{-06}$
2467	$2.39\cdot 10^{-06}$	$8.29\cdot 10^{-07}$	0.35	$3.22\cdot 10^{-06}$
9539	$1.33\cdot 10^{-07}$	$3.23\cdot 10^{-08}$	0.24	$1.01\cdot 10^{-07}$
37507	$3.07\cdot 10^{-09}$	$3.70\cdot 10^{-09}$	1.21	$6.36\cdot 10^{-10}$
148739	$9.07\cdot 10^{-11}$	$6.54\cdot 10^{-11}$	0.72	$2.53\cdot 10^{-11}$

Table 7.16: $E_P^{(\text{ho-fe})}$, higher-order finite element solution

# DOFs	$\lvert J(u)-J(u_h)\rvert$	$\lvert E(u_h)\rvert$	I_{eff}	$\lvert J(u)-\tilde{J}(u_h)\rvert$
659	$2.44\cdot 10^{-05}$	$3.09\cdot 10^{-05}$	1.26	$6.43\cdot 10^{-06}$
2467	$2.39\cdot 10^{-06}$	$8.67\cdot 10^{-07}$	0.36	$3.26\cdot 10^{-06}$
9539	$1.33\cdot 10^{-07}$	$3.47\cdot 10^{-08}$	0.26	$9.86\cdot 10^{-08}$
37507	$3.07\cdot 10^{-09}$	$3.86\cdot 10^{-09}$	1.26	$7.87\cdot 10^{-10}$
148739	$9.07\cdot 10^{-11}$	$7.48\cdot 10^{-11}$	0.83	$1.58\cdot 10^{-11}$

Table 7.17: $E_{PD}^{(\text{ho-fe})}$, higher-order finite element solution

# DOFs	$\lvert J(u)-J(u_h)\rvert$	$\lvert E(u_h)\rvert$	I_{eff}	$\lvert J(u)-\tilde{J}(u_h)\rvert$
659	$2.44\cdot 10^{-05}$	$7.52\cdot 10^{-06}$	0.31	$1.69\cdot 10^{-05}$
2467	$2.39\cdot 10^{-06}$	$1.19\cdot 10^{-06}$	0.50	$1.19\cdot 10^{-06}$
9539	$1.33\cdot 10^{-07}$	$2.95\cdot 10^{-08}$	0.22	$1.04\cdot 10^{-07}$
37507	$3.07\cdot 10^{-09}$	$2.23\cdot 10^{-09}$	0.72	$8.44\cdot 10^{-10}$
148739	$9.07\cdot 10^{-11}$	$2.32\cdot 10^{-10}$	2.56	$1.41\cdot 10^{-10}$

Table 7.18: $E_P^{(\text{ho-int})}$, higher-order interpolation

# DOFs	$\lvert J(u)-J(u_h)\rvert$	$\lvert E(u_h)\rvert$	I_{eff}	$\lvert J(u)-\tilde{J}(u_h)\rvert$
659	$2.44 \cdot 10^{-05}$	$1.94 \cdot 10^{-05}$	0.79	$5.01 \cdot 10^{-06}$
2467	$2.39 \cdot 10^{-06}$	$1.49 \cdot 10^{-07}$	0.06	$2.24 \cdot 10^{-06}$
9539	$1.33 \cdot 10^{-07}$	$3.26 \cdot 10^{-08}$	0.24	$1.01 \cdot 10^{-07}$
37507	$3.07 \cdot 10^{-09}$	$3.07 \cdot 10^{-09}$	1.00	$5.43 \cdot 10^{-12}$
148739	$9.07 \cdot 10^{-11}$	$1.55 \cdot 10^{-10}$	1.71	$6.47 \cdot 10^{-11}$

Table 7.19: $E_{PD}^{(\text{ho-int})}$, higher-order interpolation

# DOFs	$\lvert J(u)-J(u_h)\rvert$	$\lvert E(u_h)\rvert$	I_{eff}	$\lvert J(u)-\tilde{J}(u_h)\rvert$
659	$2.44 \cdot 10^{-05}$	$1.51 \cdot 10^{-05}$	0.62	$9.31 \cdot 10^{-06}$
2467	$2.39 \cdot 10^{-06}$	$4.13 \cdot 10^{-07}$	0.17	$2.80 \cdot 10^{-06}$
9539	$1.33 \cdot 10^{-07}$	$1.42 \cdot 10^{-08}$	0.11	$1.19 \cdot 10^{-07}$
37507	$3.07 \cdot 10^{-09}$	$1.62 \cdot 10^{-09}$	0.53	$1.45 \cdot 10^{-09}$
148739	$9.07 \cdot 10^{-11}$	$2.93 \cdot 10^{-11}$	0.32	$6.13 \cdot 10^{-11}$

Table 7.20: $E_{P}^{(\text{block},1)}$, block strategy, one update step, $\omega = 0.2$

# DOFs	$\lvert J(u)-J(u_h)\rvert$	$\lvert E(u_h)\rvert$	I_{eff}	$\lvert J(u)-\tilde{J}(u_h)\rvert$
659	$2.44 \cdot 10^{-05}$	$1.71 \cdot 10^{-05}$	0.70	$7.29 \cdot 10^{-06}$
2467	$2.39 \cdot 10^{-06}$	$4.54 \cdot 10^{-07}$	0.19	$2.84 \cdot 10^{-06}$
9539	$1.33 \cdot 10^{-07}$	$1.65 \cdot 10^{-08}$	0.12	$1.17 \cdot 10^{-07}$
37507	$3.07 \cdot 10^{-09}$	$1.88 \cdot 10^{-09}$	0.61	$1.19 \cdot 10^{-09}$
148739	$9.07 \cdot 10^{-11}$	$3.40 \cdot 10^{-11}$	0.37	$5.67 \cdot 10^{-11}$

Table 7.21: $E_{P}^{(\text{block},2)}$, block strategy, two update steps, $\omega = 0.2$

Scenario 4: Point Value of Vorticity

# DOFs	$\lvert J(u)-J(u_h)\rvert$	$\lvert E(u_h)\rvert$	I_{eff}	$\lvert J(u)-\tilde{J}(u_h)\rvert$
2467	$4.04 \cdot 10^{-04}$	$2.29 \cdot 10^{-04}$	0.57	$1.74 \cdot 10^{-04}$
9539	$8.56 \cdot 10^{-05}$	$4.19 \cdot 10^{-05}$	0.49	$4.36 \cdot 10^{-05}$
37507	$1.34 \cdot 10^{-05}$	$8.47 \cdot 10^{-06}$	0.63	$4.91 \cdot 10^{-06}$
148739	$8.18 \cdot 10^{-07}$	$1.87 \cdot 10^{-07}$	0.23	$6.32 \cdot 10^{-07}$

Table 7.22: $E_D^{(\text{anal.})}$, analytical solution of primal problem

# DOFs	$\lvert J(u)-J(u_h)\rvert$	$\lvert E(u_h)\rvert$	I_{eff}	$\lvert J(u)-\tilde{J}(u_h)\rvert$
2467	$4.04 \cdot 10^{-04}$	$1.48 \cdot 10^{-04}$	0.37	$2.56 \cdot 10^{-04}$
9539	$8.56 \cdot 10^{-05}$	$4.34 \cdot 10^{-05}$	0.51	$4.22 \cdot 10^{-05}$
37507	$1.34 \cdot 10^{-05}$	$8.49 \cdot 10^{-06}$	0.63	$4.89 \cdot 10^{-06}$
148739	$8.18 \cdot 10^{-07}$	$1.86 \cdot 10^{-07}$	0.23	$6.32 \cdot 10^{-07}$

Table 7.23: $E_P^{(\text{ho-fe})}$, higher-order finite element solution

# DOFs	$\lvert J(u)-J(u_h)\rvert$	$\lvert E(u_h)\rvert$	I_{eff}	$\lvert J(u)-\tilde{J}(u_h)\rvert$
2467	$4.04 \cdot 10^{-04}$	$1.48 \cdot 10^{-04}$	0.37	$2.56 \cdot 10^{-04}$
9539	$8.56 \cdot 10^{-05}$	$4.34 \cdot 10^{-05}$	0.51	$4.22 \cdot 10^{-05}$
37507	$1.34 \cdot 10^{-05}$	$8.49 \cdot 10^{-06}$	0.63	$4.89 \cdot 10^{-06}$
148739	$8.18 \cdot 10^{-07}$	$1.86 \cdot 10^{-07}$	0.23	$6.32 \cdot 10^{-07}$

Table 7.24: $E_{PD}^{(\text{ho-fe})}$, higher-order finite element solution

# DOFs	$\lvert J(u)-J(u_h)\rvert$	$\lvert E(u_h)\rvert$	I_{eff}	$\lvert J(u)-\tilde{J}(u_h)\rvert$
2467	$4.04 \cdot 10^{-04}$	$5.60 \cdot 10^{-04}$	1.39	$9.64 \cdot 10^{-04}$
9539	$8.56 \cdot 10^{-05}$	$7.58 \cdot 10^{-06}$	0.09	$7.80 \cdot 10^{-05}$
37507	$1.34 \cdot 10^{-05}$	$5.22 \cdot 10^{-06}$	0.39	$8.16 \cdot 10^{-06}$
148739	$8.18 \cdot 10^{-07}$	$5.77 \cdot 10^{-07}$	0.71	$1.40 \cdot 10^{-06}$

Table 7.25: $E_P^{(\text{ho-int})}$, higher-order interpolation

# DOFs	$\lvert J(u)-J(u_h)\rvert$	$\lvert E(u_h)\rvert$	I_{eff}	$\lvert J(u)-\tilde{J}(u_h)\rvert$
2467	$4.04 \cdot 10^{-04}$	$3.98 \cdot 10^{-04}$	0.99	$8.02 \cdot 10^{-04}$
9539	$8.56 \cdot 10^{-05}$	$2.70 \cdot 10^{-05}$	0.32	$5.86 \cdot 10^{-05}$
37507	$1.34 \cdot 10^{-05}$	$6.89 \cdot 10^{-06}$	0.51	$6.50 \cdot 10^{-06}$
148739	$8.18 \cdot 10^{-07}$	$1.95 \cdot 10^{-07}$	0.24	$1.01 \cdot 10^{-06}$

Table 7.26: $E_{PD}^{(\text{ho-int})}$, higher-order interpolation

# DOFs	$\lvert J(u) - J(u_h)\rvert$	$\lvert E(u_h)\rvert$	I_{eff}	$\lvert J(u) - \tilde{J}(u_h)\rvert$
2467	$4.04 \cdot 10^{-04}$	$4.96 \cdot 10^{-04}$	1.23	$8.99 \cdot 10^{-04}$
9539	$8.56 \cdot 10^{-05}$	$5.79 \cdot 10^{-05}$	0.68	$2.77 \cdot 10^{-05}$
37507	$1.34 \cdot 10^{-05}$	$1.34 \cdot 10^{-05}$	1.00	$1.77 \cdot 10^{-08}$
148739	$8.18 \cdot 10^{-07}$	$2.12 \cdot 10^{-07}$	0.26	$1.03 \cdot 10^{-06}$

Table 7.27: $E_P^{(\text{block},1)}$, block strategy, one update step, $\omega = 0.6$

# DOFs	$\lvert J(u) - J(u_h)\rvert$	$\lvert E(u_h)\rvert$	I_{eff}	$\lvert J(u) - \tilde{J}(u_h)\rvert$
2467	$4.04 \cdot 10^{-04}$	$2.32 \cdot 10^{-04}$	0.57	$1.72 \cdot 10^{-04}$
9539	$8.56 \cdot 10^{-05}$	$1.12 \cdot 10^{-05}$	0.13	$7.44 \cdot 10^{-05}$
37507	$1.34 \cdot 10^{-05}$	$8.65 \cdot 10^{-06}$	0.65	$2.20 \cdot 10^{-05}$
148739	$8.18 \cdot 10^{-07}$	$7.18 \cdot 10^{-07}$	0.88	$1.00 \cdot 10^{-07}$

Table 7.28: $E_P^{(\text{block},2)}$, block strategy, two update steps, $\omega = 0.6$

Scenario 5: Kinetic Energy

# DOFs	$\lvert J(u) - J(u_h)\rvert$	$\lvert E(u_h)\rvert$	I_{eff}	$\lvert J(u) - \tilde{J}(u_h)\rvert$
2467	$4.35 \cdot 10^{-03}$	$4.34 \cdot 10^{-03}$	1.00	$1.16 \cdot 10^{-05}$
9539	$2.55 \cdot 10^{-04}$	$2.56 \cdot 10^{-04}$	1.00	$1.17 \cdot 10^{-06}$
37507	$1.55 \cdot 10^{-05}$	$1.56 \cdot 10^{-05}$	1.00	$1.89 \cdot 10^{-08}$
148739	$9.65 \cdot 10^{-07}$	$9.65 \cdot 10^{-07}$	1.00	$2.94 \cdot 10^{-10}$

Table 7.29: $E_D^{(\text{anal.})}$, analytical solution of primal problem

# DOFs	$\lvert J(u) - J(u_h)\rvert$	$\lvert E(u_h)\rvert$	I_{eff}	$\lvert J(u) - \tilde{J}(u_h)\rvert$
2467	$4.35 \cdot 10^{-03}$	$4.17 \cdot 10^{-03}$	0.96	$1.83 \cdot 10^{-04}$
9539	$2.55 \cdot 10^{-04}$	$2.52 \cdot 10^{-04}$	0.99	$2.98 \cdot 10^{-06}$
37507	$1.55 \cdot 10^{-05}$	$1.55 \cdot 10^{-05}$	1.00	$5.01 \cdot 10^{-08}$
148739	$9.65 \cdot 10^{-07}$	$9.64 \cdot 10^{-07}$	1.00	$8.03 \cdot 10^{-10}$

Table 7.30: $E_P^{(\text{ho-fe})}$, higher-order finite element solution

# DOFs	$\lvert J(u) - J(u_h)\rvert$	$\lvert E(u_h)\rvert$	I_{eff}	$\lvert J(u) - \tilde{J}(u_h)\rvert$
2467	$4.35 \cdot 10^{-03}$	$4.17 \cdot 10^{-03}$	0.96	$1.83 \cdot 10^{-04}$
9539	$2.55 \cdot 10^{-04}$	$2.52 \cdot 10^{-04}$	0.99	$2.98 \cdot 10^{-06}$
37507	$1.55 \cdot 10^{-05}$	$1.55 \cdot 10^{-05}$	1.00	$5.01 \cdot 10^{-08}$
148739	$9.65 \cdot 10^{-07}$	$9.64 \cdot 10^{-07}$	1.00	$8.03 \cdot 10^{-10}$

Table 7.31: $E_{PD}^{(\text{ho-fe})}$, higher-order finite element solution

# DOFs	$\lvert J(u) - J(u_h)\rvert$	$\lvert E(u_h)\rvert$	I_{eff}	$\lvert J(u) - \tilde{J}(u_h)\rvert$
2467	$4.35 \cdot 10^{-03}$	$3.57 \cdot 10^{-03}$	0.82	$7.81 \cdot 10^{-04}$
9539	$2.55 \cdot 10^{-04}$	$2.52 \cdot 10^{-04}$	0.99	$3.03 \cdot 10^{-06}$
37507	$1.55 \cdot 10^{-05}$	$1.57 \cdot 10^{-05}$	1.01	$1.23 \cdot 10^{-07}$
148739	$9.65 \cdot 10^{-07}$	$9.67 \cdot 10^{-07}$	1.00	$2.07 \cdot 10^{-09}$

Table 7.32: $E_P^{(\text{ho-int})}$, higher-order interpolation

# DOFs	$\lvert J(u) - J(u_h)\rvert$	$\lvert E(u_h)\rvert$	I_{eff}	$\lvert J(u) - \tilde{J}(u_h)\rvert$
2467	$4.35 \cdot 10^{-03}$	$3.35 \cdot 10^{-03}$	0.77	$1.01 \cdot 10^{-03}$
9539	$2.55 \cdot 10^{-04}$	$2.51 \cdot 10^{-04}$	0.98	$4.25 \cdot 10^{-06}$
37507	$1.55 \cdot 10^{-05}$	$1.56 \cdot 10^{-05}$	1.01	$1.01 \cdot 10^{-07}$
148739	$9.65 \cdot 10^{-07}$	$9.67 \cdot 10^{-07}$	1.00	$1.72 \cdot 10^{-09}$

Table 7.33: $E_{PD}^{(\text{ho-int})}$, higher-order interpolation

# DOFs	$\lvert J(u) - J(u_h)\rvert$	$\lvert E(u_h)\rvert$	I_{eff}	$\lvert J(u) - \tilde{J}(u_h)\rvert$
2467	$4.35 \cdot 10^{-03}$	$4.67 \cdot 10^{-03}$	1.07	$3.16 \cdot 10^{-04}$
9539	$2.55 \cdot 10^{-04}$	$3.03 \cdot 10^{-04}$	1.19	$4.77 \cdot 10^{-05}$
37507	$1.55 \cdot 10^{-05}$	$1.92 \cdot 10^{-05}$	1.23	$3.63 \cdot 10^{-06}$
148739	$9.65 \cdot 10^{-07}$	$1.20 \cdot 10^{-06}$	1.24	$2.36 \cdot 10^{-07}$

Table 7.34: $E_P^{(\text{block},1)}$, block strategy, one update step, $\omega = 0.7$

# DOFs	$\lvert J(u) - J(u_h)\rvert$	$\lvert E(u_h)\rvert$	I_{eff}	$\lvert J(u) - \tilde{J}(u_h)\rvert$
2467	$4.35 \cdot 10^{-03}$	$5.26 \cdot 10^{-03}$	1.21	$9.61 \cdot 10^{-03}$
9539	$2.55 \cdot 10^{-04}$	$3.01 \cdot 10^{-04}$	1.18	$5.57 \cdot 10^{-04}$
37507	$1.55 \cdot 10^{-05}$	$1.83 \cdot 10^{-05}$	1.18	$3.39 \cdot 10^{-05}$
148739	$9.65 \cdot 10^{-07}$	$1.14 \cdot 10^{-06}$	1.18	$2.10 \cdot 10^{-06}$

Table 7.35: $E_P^{(\text{block},2)}$, block strategy, two update steps, $\omega = 0.7$

Bibliography

[1] R. A. Adams and J. J. F. Fournier. *Sobolev spaces.* Pure and applied mathematics; 140. Academic Press, Amsterdam, 2. ed., repr. edition, 2007.

[2] W. Bangerth and R. Rannacher. *Adaptive Finite Element Methods for Differential Equations.* Birkhäuser Verlag, 2003.

[3] R. E. Bank and A. Weiser. Some a posteriori error estimators for elliptic partial differential equations. *Math. Comp*, 44:283–301, 1985.

[4] M. Baumann and V. Heuveline. Evaluation of Different Strategies for Goal Oriented Adaptivity in CFD – Part I: The Stationary Case. EMCL Preprint Series, ISSN: 2191-0693, 2010.

[5] R. Becker, V. Heuveline, and R. Rannacher. An Optimal Control Approach to Adaptivity in Computational Fluid Mechanics. *International Journal for Numerical Methods in Fluids*, 40(1-2):105–120, 2002.

[6] M. Beckers, H. J. H. Clercx, G. J. F. van Heijst, and R. Verzicco. Dipole formation by two interacting shielded monopoles in a stratified fluid. *Phys. Fluids*, 14(2):704–720, 2002.

[7] M. Braack and A. Ern. A posteriori control of modeling errors and discretization errors. *Multiscale Model. Simul.*, 1(2):221–238, 2003.

[8] M. Braack and R. Rannacher. Adaptive finite element methods for low-mach-number flows with chemical reactions. In *of 30th Computational Fluid Dynamics, von Karman Institute*, pages 1–93, 1999.

[9] D. Braess. *Finite elements: Theory, fast solvers, and applications in solid mechanics.* Cambridge Univ. Press, Cambridge [u.a.], 2. ed. edition, 2001.

[10] F. Brezzi. On the existence, uniqueness, and approximation of saddle point problems arising from Lagrangian multipliers. *Revue française d'automatique, informatique, recherche opérationnelle. Analyse Numérique*, 8(2):129–151, 1974.

[11] F. Brezzi and R. S. Falk. Stability of higher-order hood-taylor methods. *SIAM Journal on Numerical Analysis*, 28(3):581–590, 1991.

[12] E. Burman, A. Ern, and V. Giovangigli. An adaptive finite element method with crosswind diffusion for low mach, steady, laminar combustion. *J. Comput. Phys.*, 188:472–492, July 2003.

[13] J. Carpio Huertas. *Duality methods for time-space adaptivity to calculate the numerical solution of partial differential equations.* PhD thesis, Matemática Aplicada a la Ingeniería Industrial / E.T.S.I. Industriales (UPM), 2008.

[14] A. Chorin. Numerical solution for the navier-stokes equations. *Math. Comp*, 22:745–762, 1968.

[15] C. Davis, W. Wang, S. Cavallo, J. Done, J. Dudhia, S. Fredrick, J. Michalakes, G. Caldwell, T. Engel, and R. Torn. High-resolution hurricane forecasts. *Computing in Science and Engg.*, 13:22–30, January 2011.

[16] J. Doyle, C. Reynolds, and C. Amerault. Diagnosing tropical cyclone sensitivity. *Computing in Science and Engineering*, 13:31–39, 2011.

[17] S. C. Eisenstat and H. F. Walker. Choosing the forcing terms in an inexact newton method. *SIAM J. Sci. Comput.*, 17:16–32, January 1996.

[18] K. Emanuel. Tropical Cyclones. *Annu. Rev. Earth. Planet. Sci.*, 31:75–104, 2003.

[19] E. Emmrich. *Gewöhnliche und Operator-Differentialgleichungen: Eine integrierte Einführung in Randwertprobleme und Evolutionsgleichungen für Studierende.* Vieweg, Wiesbaden, 1. Aufl. edition, 2004.

[20] K. Eriksson, D. Estep, P. Hansbo, and C. Johnson. Introduction to Adaptive Methods for Differential Equations. *Acta Numerica*, 4(-1):105–158, 1995.

[21] A. Ern and J.-L. Guermond. *Theory and practice of finite elements.* Applied mathematical sciences; 159. Springer, New York, 2004.

[22] M. D. Gunzburger. *Finite Element Methods for Viscous Incompressible Flows.* Academic Press, 1989.

[23] R. Hartmann. A posteriori Fehlerschätzung und adaptive Schrittweiten- und Ortsgittersteuerung bei Galerkin-Verfahren für die Wärmeleitungsgleichung. Diplomarbeit, Institut für Angewandte Mathematik, Universität Heidelberg, 1998.

[24] R. Hartmann. Multitarget error estimation and adaptivity in aerodynamic flow simulations. *SIAM J. Sci. Comput.*, 31(1):708–731, 2008.

[25] V. Heuveline and R. Rannacher. Duality-based adaptivity in the hp-finite element method. *Journal of Numerical Mathematics*, 11(2):95–113, 2003.

[26] V. Heuveline and R. Rannacher. Adaptive FEM for Eigenvalue Problems with Application in Hydrodynamic Stability Analysis. *Journal of Numerical Mathematics*, pages 1–32, 2006.

[27] V. Heuveline and F. Schieweck. On the inf-sup condition for higher order mixed fem on meshes with hanging nodes. *Mathematical Modelling and Numerical Analysis M2AN*, 41(1):1–20, 2007.

[28] V. Heuveline. Hiflow3: a flexible and hardware-aware parallel finite element package. In *Proceedings of the 9th Workshop on Parallel/High-Performance Object-Oriented Scientific Computing*, POOSC '10, pages 4:1–4:6, New York, NY, USA, 2010. ACM.

[29] M. Hinze, R. Pinnau, M. Ulbrich, and S. Ulbrich. *Optimization with PDE Constraints*. Springer, 2008.

[30] J. R. Holton. *An Introduction to Dynamic Meteorology*. International geophysics series; 88. Elsevier Acad. Press, Amsterdam, 4. ed. edition, 2004.

[31] W. Layton. *Introduction to the Numerical Analysis of Incompressible Viscous Flows*. Society for Industrial and Applied Mathematics, Philadelphia, PA, USA, 2008.

[32] A. J. Majda and A. L. Bertozzi. *Vorticity and Incompressible Flow*. Cambridge University Press, 1 edition, December 2001.

[33] J. Mayer. A multilevel crout ilu preconditioner with pivoting and row permutation. *Numerical Linear Algebra with Applications*, 14(10):771–789, 2007.

[34] J. Mayer. Symmetric permutations for i-matrices to delay and avoid small pivots during factorization. *SIAM J. Sci. Comput.*, 30:982–996, March 2008.

[35] M. B. Monagan, K. O. Geddes, K. M. Heal, G. Labahn, S. M. Vorkoetter, J. McCarron, and P. DeMarco. *Maple 10 Programming Guide*. Maplesoft, Waterloo ON, Canada, 2005.

[36] A. Quarteroni and A. Valli. *Numerical approximation of partial differential equations*. Springer series in computational mathematics; 23. Springer, Berlin, 1994.

[37] Y. Saad and M. H. Schultz. Gmres: A generalized minimal residual algorithm for solving nonsymmetric linear systems. *SIAM Journal on Scientific and Statistical Computing*, 7(3):856–869, 1986.

[38] L. Scheck, S. C. Jones, and M. Juckes. The Resonant Interaction of a Tropical Cyclone and a Tropopause Front in a Barotropic Model, Part I: Zonally-oriented Front. *J. Atmos. Sci.*, 68:405–419, 2011.

[39] F. Schieweck. A-stable discontinuous galerkin-petrov time discretization of higher order. *Journal of Numerical Mathematics*, 18(1):25–57, 04 2010.

[40] M. Schmich and B. Vexler. Adaptivity with dynamic meshes for space-time finite element discretizations of parabolic equations. *SIAM J. Sci. Comput.*, 30(1):369–393, 2007.

[41] S. Shin, J. Han, and J. Baik. On the critical separation distance of binary vortices in a nondivergent barotropic atmosphere. *Journal of the Meteorological Society of Japan*, 84(5):853–869, 2006.

[42] R. K. Smith, W. Ulrich, and G. Dietachmayer. A numerical study of tropical cyclone motion using a barotropic model. I: The role of vortex asymmetries. *Quart. J. Roy. Meteor. Soc.*, 116(492):337–362, 1990.

[43] J. Spurk and N. Aksel. *Fluid Mechanics.* Springer, 2010.

[44] E. Stein and E. Ramm. *Error controlled adaptive finite elements in solid mechanics.* Wiley, Chichester, 2003.

[45] A. H. Stroud. *Approximate calculation of multiple integrals.* Englewood Chiffs, New Jersey: Prentice-Hall, 1971.

[46] R. Temam. *Navier-Stokes equations and nonlinear functional analysis.* Regional conference series in applied mathematics; 66. Soc. for Industrial and Applied Mathematics, Philadelphia, 2. ed. edition, 1995.

[47] R. Temam. *Navier-Stokes equations: Theory and Numerical Analysis.* AMS Chelsea Publ., Providence, RI, reprinted with corr. edition, 2001.

[48] V. Thomée. *Galerkin Finite Element Methods for Parabolic Problems (Springer Series in Computational Mathematics).* Springer-Verlag New York, Inc., Secaucus, NJ, USA, 2006.

[49] S. Valcke and J. Verron. Interactions of baroclinic isolated vortices: The dominant effect of shielding. *J. Phys. Oceanogr.*, 27(4):524–541, April 1997.

[50] R. Verführth. *A Review of A Posteriori Error Estimation and Adaptive Mesh-Refinement Techniques.* Wiley-Teubner, 1996.

[51] J. Wloka. *Partial differential equations.* Cambridge Univ. Pr., Cambridge, engl. ed., reprinted edition, 1992.

[52] E. Zeidler. *Applied Functional Analysis*, volume Main Principles and Their Applications of *Applied Mathematical Sciences.* Springer Verlag, New York, 1995.